Unexpected temperature and polarization behavior of the high-T_C superconductor Bi(Pb)-2212

DISSERTATION

zur Erlangung des akademischen Grades
doctor rerum naturalium
(Dr. rer. nat.)
im Fach Physik

eingereicht an der
Mathematisch-Naturwissenschaftlichen Fakultät I
Humboldt-Universität zu Berlin

von
Herrn M.Sc. Aliakbar Ghafari

Präsident der Humboldt-Universität zu Berlin:
Prof. Dr. Jan-Hendrik Olbertz

Dekan der Mathematisch-Naturwissenschaftlichen Fakultät I:
Prof. Stefan Hecht, PhD.

Gutachter:
1. Prof. Dr. Recardo Manzke
2. Prof. Dr. Wolfgang Nolting
3. Prof. Dr. Martin Knupfer

eingereicht am: 12.02.2013
Tag der mündlichen Prüfung: 30.05.2013

Abstract

In this PhD work the electronic structure of high-T_C Bi-2212 cuprates is investigated. For this purpose x-ray absorption spectroscopy (XAS) and angle resolved photoemission spectroscopy (ARPES) are used. Additionally, density functional theory is applied for making theoretical trends of the electronic structure evident. At first, the temperature dependence of the hole density (n_H) by XAS on nearly optimum and slightly underdoped single crystals is studied. The measurements of the temperature dependence of n_H by XAS show completely different behavior as that derived from Hall effect. Moreover, fitting our data by the Gor'kov and Teitel'baum formula, i.e. assuming a constant term and an activation term, was impossible. For solving the problem a contribution of magnons is suggested. Additionally, the polarization dependence of the hole density has been measured by XAS showing that an inhomogeneity of holes in the copper oxide planes may exist. Such a behavior is not expected for the isotropic structure of the Bi(Pb)-2212 crystals and was only hardly to be explained. Possibly, magnetic symmetry breaking properties like e.g. magnetic stripes might give an answer. In order to derive additional experimental information, the temperature and polarization dependence of the electronic structure of the CuO_2 planes of Bi(Pb)-2212 single crystals has been studied by ARPES. In particular, the so-called peak-dip-hump emission structure close to the Fermi energy has been measured, which is located at the M point of the Brillouin zone. The results show that the sharp emission structure close to the Fermi edge reveals a distinct polarization dependence and it vanishes at the pseudogap temperature T^* and not at the critical temperature T_C. The polarization dependence at the four M points of the Brillouin zone has revealed that there exists a symmetry line along to 45° from the Cu-O-Cu direction. This could also be due to stripe formation. Additionally, the observed failure of the dipole approximation to describe the spectra at normal polarization with respect to the mirror plane is discussed. On the other hand, the calculation of material properties by density functional theory has become a very active area of research in condensed matter physics. Therefore, after my calculations based on DFT by the MBJ potential have revealed good agreement with experimental data for the ternary semiconductors $ZrSe_xS_{2-x}$ and the $LiZrSe_xS_{2-x}$ compound I applied it for a support of the experimental superconductor data. The electronic properties of $CaCuO_2$ and the Bi-2212 cuprate have been calculated by DFT based on GGA and GGA+U where the Hubbard U term has been calculated by an ab initio method. The results reveal that only calculations based on MBJ+U lead to an anti-ferromagnetic ground state for the $CaCuO_2$ compound while all functionals fail to find an anti-ferromagnetic ground state for Bi-2212.

Zusammenfassung

In dieser Doktorarbeit wird der Hochtemperatur-Supraleiter Bi-2212 auf seine elektronische Struktur hin untersucht. Für diesen Zweck wurden Röntgen-Absorptionsspektroskopie (XAS) und winkelaufgelöste Photoemissionsspektroskopie (ARPES) verwendet. Zusätzlich wurden mittels Dichtefunktionaltheorie theoretische Trends in der elektronischen Struktur aufgezeigt. Zu Beginn wurde die Temperaturabhängigkeit der Löcher-Konzentration (n_H) von nahezu optimal dotierten und geringfügig unterdotierten Einkristallen mittels XAS untersucht. Die Messungen der Temperaturabhängigkeit von n_H mit XAS zeigen ein komplett anderes Verhalten als das, welches aus dem Hall-Effekt hergeleitet wurde. Hinzu kommt, dass es unmöglich ist, die Formel von Gor'kov und Teitel'baum, d.h. mit einem konstanten und einem Aktivierungsterm, an die Daten anzupassen. Als Lösungsansatz kommen Magnonen in Frage. Zusätzlich wurde die Polarisationsabhängigkeit der Löcher-Konzentration mittels XAS gemessen, die zeigt, dass in den Kupferoxidschichten die Löcher offenbar offenbar inhomogen verteilt sind. Solch ein Verhalten wird für die isotrope Struktur der Bi-2212-Kristalle nicht erwartet und kann nur schwer erklärt werden. Möglicherweise sind die, die Symmetrie brechenden magnetischen Eigenschaften wie magnetische Streifen die Antwort. Um zusätzliche experimentelle Informationen zu erhalten, wurde darüber hinaus noch die Temperatur- und Polarisationsabhängigkeit der Bi-2212-Einkristalle mittels ARPES studiert. Insbesondere die 'Peak-Dip-Hump'-Emissionsstruktur an der Fermi-Energie wurde gemesssen, die sich am M-Punkt der Brillouin-Zone befindet. Die Ergebnisse zeigen, dass der scharfe Peak nahe der Fermi-Kante eine deutliche Polarisations- und Temperaturabhängigkeit aufweist, welche bei der Pseudolücken-Temperatur T^* und nicht bei der Sprungtemperatur T_C verschwindet. Die Polarisationsabhängigkeit an den vier M-Punkten der Brillouin-Zone hat gezeigt, dass eine Symmetrieachse im 45°-Winkel zur Cu-O-Cu-Richtung existiert. Dies könnte ebenfalls mit magnetischer Streifenbildung erklärt werden. Des Weiteren wurde das beobachtete Versagen der Dipol-Näherung zur Beschreibung der Spektren bei einer Polarisation senkrecht zur Spiegelebene erörtert. Andererseits ist die Berechnung von Materieleigenschaften mittels der Dichtefunktionaltheorie ein sehr aktiver Bereich der Festkörperphysik geworden. Nachdem meine DFT-Rechnungen auf der Basis des MBJ-Potentials sehr gute Übereinstimmung mit den experimentellen Ergebnissen des ternären Halbleiters $ZrSe_xS_{2-x}$ und die $LiZrSe_xS_{2-x}$ –Verbindung erzielt haben, habe ich diese auch zur Unterstützung der experimentellen Supraleiterdaten angewendet. Die elektronischen Eigenschaften von $CaCuO_2$ und des Bi-2212-Kuprats wurden mittels DFT auf der Basis von GGA und GGA+U berechnet, wobei der Hubbard-U-Term mit einer „ab-

initio“-Methode berechnet wurde. Die Ergebnisse ergaben, dass nur Rechnungen auf der Basis von MBJ+U einen antiferromagnetischen Grundzustand für die $CaCuO_2$-Verbindung lieferten, während alle Funktionale versagten, den antiferromagnetischen Grundzustand für das Bi-2212-Kuprat zu finden.

Acknowledgments

This thesis was performed at the electronic structure and superconductivity (EES) group at the Humboldt University of Berlin. I believed that a major research project like this is never the work of anyone alone. First, I would like to express my gratitude to my supervisor, Professor Recardo Manzke. His leadership, support, attention to detail, hard work, and vast knowledge added considerably to my graduate experience. A very special thanks goes out to PD Dr. Christoph Janowitz, without whose discussions and assistance during measurements I would not have considered a graduate career in PhD physics research. I would like to thank Dr. Helmut Dwelk for conducting the Hall effect and the AC-Susceptibility measurements for some samples, as well as Dr. Alica Krapf for preparing the crystals. I would like to thank Ahmad Kamal Ariffin and the staff of BESSY II for assistance during the XAS measurements. I must also acknowledge Mrs. Kaiser and others in the EES group for their support.

Furthermore, I gratefully thank for the Yousef Jameel Scholarship of the Humboldt University of Berlin.

Finally, I would like to thank my family for their unconditional support throughout my degree. In particular, the patience and understanding shown by my wife, mum, and dad during these years is greatly appreciated.

Aliakbar Ghafari

List of Abbreviations

ARPES: angle resolved photoemission spectroscopy
BSCCO: Bismuth-strontium-calcium-copper-oxide
BZ: Brillouin zones
1BH: one band Hubbard model
3BH : three-band p-d Hubbard model
CT: charge transfer
CDW: charge density wave
DOS: density of states
DFT: density functional theory
DMFT: dynamical mean field theory
1D: one-dimensional
EDX: x-ray analysis
EPI: electron-phonon interaction
EXAFS: Extended x-ray absorption fine structure
EY: electron yield
FL: Fermi-liquid
FY: fluorescence yield
FS: Fermi surface
GGA: generalised gradient approximation
HTC: high-T_C cuprates
LDA: local-density approximation
LHB: lower Hubbard band
MFL: Marginal Fermi liquid
NFL: non-Fermi liquid
PG : pseudogap
QP: quasiparticle
RIXS: resonant inelastic X-ray scattering
RVB: Resonating Valence Bonds
TMD: transition metal dichalcogenides
UHB: upper Hubbard band
XAS: x-ray absorption spectroscopy
XANES: x-ray absorption near edge structure
YBCO: Yttrium-barium-copper-oxide
ZRS: Zhang-Rice singlet

Contents page

Contents page

Chapter 1

Introduction

Superconductivity remains a mystery in condensed matter physics, a century after it was found in Hg. Research on superconductivity, including understanding the mechanisms of superconductivity, still poses great challenges in physics, such that superconductivity remains an exciting field in condensed matter physics. Consequently, over 100,000 scientific publications on superconductivity exist today. In 1957, John Bardeen, Leon Cooper, and Robert Schrieffer [1] successfully modeled the properties of conventional superconductors using the BCS theory. Pairing of electrons that are close to the Fermi level into Cooper pairs, due to interactions with the crystal lattice, is a key conceptual element in BCS theory. However, high-T_C cuprates (HTC) exhibit different behavior [2]. These types of superconductors have transition temperatures well above the boiling point of liquid nitrogen (77 K), as discovered by Wu et al. [3] in 1986 for an yttrium-barium-copper-oxygen compound.

Cuprates are categorized into two groups: hole-doped and electron-doped cuprates. The hole-doped family is divided into four subfamilies, as follows: i) yttrium-barium-copper-oxide (YBCO), ii) bismuth-strontium-calcium-copper-oxide (BSCCO), iii) thallium-barium-calcium-copper-oxide, and iv) mercury-barium-calcium-copper-oxide. As in BCS theory, superconductivity in cuprates is also due to the pairing of charges into Cooper pairs, with charges of 2e and -2e for hole- and electron-doped compounds, respectively. Undoped cuprates

possess a half-filled conduction band (one electron per unit cell) and should behave as metals, but strong electronic correlations block electron transport and open up a charge transfer gap. Thus, these so-called parent compounds are insulators the number of free carriers is zero at low temperature. In 1987, Anderson [4] identified three essential features in cuprates: i) They are quasi–two dimensional, such that the key structural unit is the CuO_2 plane with very weak interplane coupling, ii) superconductivity is created by doping, and iii) cuprates can exhibit novel behavior due to low dimensionality and doping that is not explicable in terms of conventional metallic physics. Furthermore, magnetic interactions are currently believed to play a fundamental role in the pairing mechanism in cuprates [5-8], as evidenced e.g. by the temperature dependence of the hole density in chapter 4 of this work.

In conventional superconductors, the electron-phonon interaction (EPI) plays a vital role in the appearance of superconductivity. It should also be noted that the charge density waves (CDW) e.g. in transition metal dichalcogenides are driven by the EPI, as discussed by Borisenko et al. [9] and Moncton et al. [10]. For instance, superconductivity is observed when CDW are suppressed, e.g. in Cu_xTiSe_2 [11]. Therefore, the results for transition metal dichalcogenides may be also important for CDW and superconductivity formation in HTC. Furthermore, the transition metal dichalcogenides and HTC are not only quasi-two-dimensional materials, but they are also candidate materials for negative Hubbard U, which will be discussed in section 2.6. In this thesis, I shall focus on Bi(Pb)-2212 single crystals and attempt to answer some central questions about HTC, such as those given below.

On the use of x-ray absorption spectroscopy (XAS):

- Is there an in-plane polarization dependence for the excitations in the copper oxide plane?
- Is the density of holes in the copper oxide plane uniform?
- Does the hole density exhibit thermal behavior and is it similar in the experimental techniques XAS and Hall effect?
- Do the magnetic excitations make an observable contribution in cuprates?

On the use of angle resolved photoemission spectroscopy (ARPES):

- Can we explain polarization dependent ARPES data by using conventional matrix elements?
- Is there evidence by ARPES for one-dimensional charge ordering in cuprates?

On the use of density functional theory (DFT):

- Why do DFT functionals, such as the local-density approximation (LDA) and the generalized gradient approximation (GGA), fail to describe the ground state of HTC?
- Can we find an anti-ferromagnetic gap for Bi-2212 compounds using DFT+U?
- Can we use DFT to compute XAS data that are comparable to experimental data?

The general physics of high-T_C cuprates will thus be reviewed in chapter two. Chapter three discusses the hole concentration and the Hall constant of the cuprates. We shall see that there is still no real solution, after 27 years, for the interpretation of the Hall coefficient in these materials. In chapter four, I shall answer central questions on the thermal behavior of the hole density by introducing an empirical formula that is an extension of the Gor'kov and Teitel'baum formula [12]. The formula shows the role of magnetic interactions in cuprates. In addition, we shall see that the temperature dependence of the hole density and that of R_H (from chapter three) explains why cuprates can not be described as Fermi liquids or marginal Fermi liquids. Moreover, no in-plane polarization dependence of the CuL_3 and O K absorption edge is expected due to the $d_{x^2-y^2}$ symmetry of the matrix elements. However, XAS measurements reveal an in-plane polarization dependence. In chapter four, we shall conclude that the hole density distribution in the copper plane seems to be inhomogeneous. Therefore one ends up with the question whether such polarization effects of the CuO_2 plane of Bi-2212 can be also observed by ARPES. This question will be answered in chapter five, where ARPES is used to find the polarization and temperature dependence of the density of states at the M point in the Brillouin zone crystals. We shall also see that the simple matrix element description breaks down for interpreting the observed

polarisation dependence. The failure of the dipole approximation to describe the density of states at polarizations normal to a mirror plane is especially evident for the CuO_2 plane. Moreover, the polarization dependence at all four M points in the Brillouin zone reveals a set of differences that supports this behavior. Density functional theory (DFT), a powerful technique for describing the electronic structure of many solids, will be reviewed in chapter six. DFT-based calculations will be presented to confirm the experimental results in chapters four and five. General aspects of DFT, the exchange correlation energy and the reason why LDA and GGA fail to describe the ground state of HTC will be discussed. DFT and DFT+U are used to calculate the electronic structure of Bi-2212, based on the full potential method. The capability of DFT to calculate XAS at the CuL_3 and O K edge of Bi-2212 is also explained. Finally, the conclusions of the thesis will be presented in chapter seven.

Chapter 2

Physics of the high-T_C cuprates

In this chapter the general aspects of the high-T_C cuprates (HTC) are reviewed. For this propose the crystal structure in real and reciprocal space as well as the phase diagram of the cuprates are explained. The method for crystal growth and sample characterization is reviewed. Then the Fermi liquid (FL), marginal FL, and Luttinger liquid phenomenologies are discussed. In next chapter the capability of these models are evaluated for Hall coefficient data. The phenomenological models will be followed by the Hubbard model which is the simplest model for describing the electronic structure of the cuprates. Additionally, the negative U centers is reviewed. Finally, stripes and magnetic behavior are discussed.

2.1 Crystal structure of Bi cuprates

Bi cuprates which are compounds of Bismuth, Strontium, Calcium, Copper, and Oxygen form a family of high temperature superconductors. In this family three main structural areas are interesting which are the average structure, the cause of the observed structural modulation, and finally the oxygen positions and their role in the last two points [13]. In the following these three areas will be discussed.

The general chemical formula of the members of the Bi family can be written as $Bi_2Sr_2Ca_{n-1}Cu_nO_{2n+4+\delta}$ where the number of CuO_2 layers (n) in the unit cell changes practically from 1 to 3. They are often assigned as Bi-2201, Bi-2212, and Bi-2223 with critical temperatures up to 40 K, 95 K, and 110 K, respectively. On the other hand, $Bi_2Sr_2Ca_{n-1}Cu_nO_{2n+4+\delta}$ structures can be described as a stacking of a basic Bi-2201 unit with zero, one, or two $CaCuO_2$ slabs inserted. In the Bi family compounds due to a long-range modulation along the [010] direction the crystal structure is more complicated than the ideal structure which is described in the following.

The tetragonal phase of Bi-2201is shown in FIG. 2.1a. It is described by the space group I4/mmm (space group number 139). For better visibility one half of the neighboring unit cell is also depicted. The nonequivalent atomic positions are presented in table 2.1. In the tetragonal phase the lattice parameters from x-ray diffraction has been reported as a=3.8097 Å and c=24.607 Å [14, 15, 16]. From FIG. 2.1a it can be seen that the perovskite-like block contains one copper-oxygen plane. The general formula of the perovskite structure is ABX_3 which has cubic symmetry where A and B are cation metals located at the centers and the corners of the cubic cell, respectively, while X (anion) is located in the middle of the 12 edges of the cubic cell [18] (FIG. 2.1b) . The orthorhombic symmetry phase has been also reported for Bi-2201 with lattice parameters a=5.392 Å, b=5.394 Å, c=24.537 Å, and space group Amaa [16].

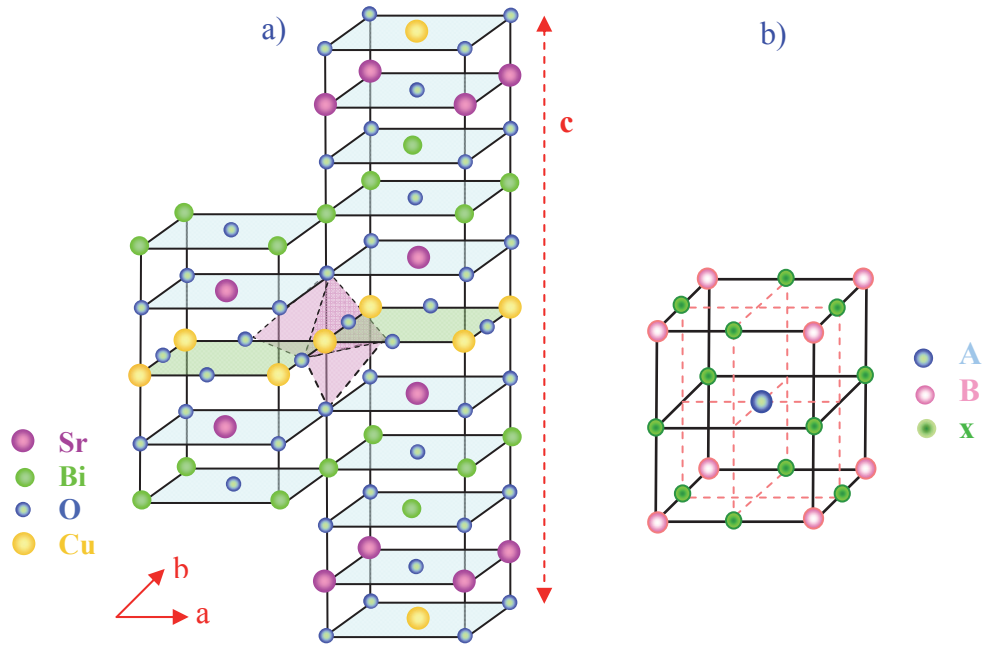

FIG. 2.1: a) The crystal structure of Bi-2201 in the tetragonal phase with space group I4/mmm (space group number 139). For details see the text. b) Perovskit structure with the general formula of ABX_3 where A and B are cation metals located at the center and corners of the cubic cell, respectively, while X is located in the middle of the 12 edges of the cubic cell.

Regarding the second family member, i.e Bi-2212, also two types of crystal structures have been reported which are even tetragonal and orthorhombic [14, 15, 16]. These two structures are depicted in FIG. 2.2a and FIG. 2.2b where for better visibility one half of the neighboring unit cell is also depicted. In the tetragonal cell with space group I4/mmm (space group number 139) the experimental lattice parameters are reported as a=3.814 Å and c=30.52 Å [14] and the nonequivalent atomic positions are also presented in table 2.1. From FIG. 2.2a it can be seen that along the [001] direction the structure can be described as two neighboring slabs of thickness c/2. As such they are shifted by a/2 and bonded by the Bi-O bonds which have a length of about 3.0 Å. Each slab consists of seven layers in which the Ca layers are sandwiched by two

CuO_2, SrO, and BiO layers (FIG. 2.2). Therefore, each slab contains one formula unit of $Bi_2Sr_2CaCu_2O_8$.

On the other hand, the orthorhombic phase of Bi-2212 is also reported by several structural investigations like such as x-ray, neutron, and electron diffraction methods. In table 2.1 the crystal data of the nonequivalent atomic positions and the lattice parameters are presented. In the orthorhombic structure atoms are moved from their tetragonal positions and therefore the symmetry group is changed to Fmmm (space group number 69). This structure is represented in FIG. 2.2b where the lattice constants were reported as 5.414 Å, b=5.418 Å, and c=30.89 Å [15]. Finally, two mirror planes can be observed in the tetragonal structure while in the orthorhombic cell it is changed to one.

A structural supermodulation causes displacements of the atomic position of about 0.6 Å from the ideal crystalline locations in Bi-2212. This behavior has been experimentally observed by x-ray diffraction [14, 19-22] and by scanning tunneling microscopy [23]. For the cause of the structural modulation several models were proposed by Zanderbergen et al. [24]. They argued that the modulation is caused by i) extra oxygen, ii) strontium vacancies, iii) partial substitution of Bi by Cu and Sr by Bi, iv) change in the orientation of the Bi lone pairs, and (v) a combination of (i) and (iii). While several other groups believed that it is only due to extra oxygen, such as Goodman et al. [25], Zhang and Sato [26], Levin et al. [27], and Walker and Wieming [28]. On the other hand, Calestani et al. [29] did not find extra oxygen by analyzing x-ray diffraction data on single crystals. Therefore, they concluded that a mismatch between the perovskite block and the stereochemical requirements of the Bi in the Bi-O layers leads to the modulation. Additionally, Lee et al. [30] have found that the modulation wave vector of the Bi-2212 is determined by

$$\mathbf{q}=0.243\mathbf{b}^*+\mathbf{c}^* \qquad (2\text{-}1)$$

where **q** is the modulation wave vector and **b**, **c** are reciprocal lattice vectors. It means that the Bi-2212 single crystal has an incommensurate modulation in the crystallographic b direction with a period (1/0.243) **b** and a commensurate modulation in the c direction.

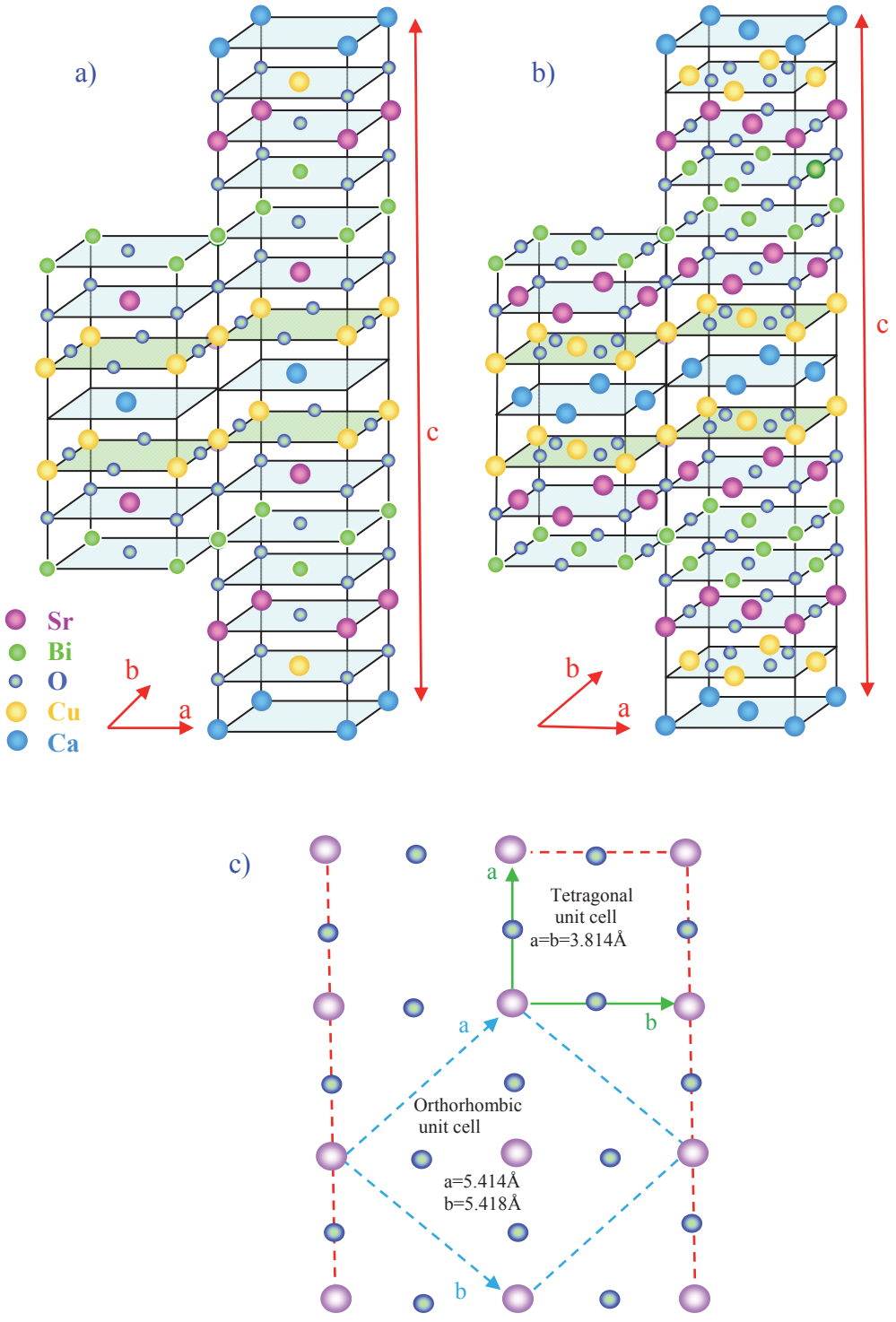

FIG. 2.2: a) and b) are the crystal structures of Bi-2212 in tetragonal (space group I4/mmm, space group number 139) and orthorhombic symmetry (space group Fmmm, number 69), respectively. c) Periodic lattice modulation in the copper plane with tetragonal and orthorhombic unit cell.

Table 2.1: Crystal data of nonequivalent atoms of Bi-2201, Bi-2212, and Bi-2223 in the tetragonal phase with space group I4/mmm (space group number 139) [17]. For Bi-2212 the orthorhombic phase is also presented (with space group Fmmm, No.69, a=5.414 Å, b=5.418 Å, c=30.890 Å) [15]. Additionally the n=3 tetragonal phase (Bi-2223) with three CuO_2 planes per unit cell is depicted.

Atom	Bi-2201 (tetragonal)	Bi-2212 (tetragonal)	Bi-2212 (orthorhombic)	Bi-2223 (tetragonal)
	x, y, z	x, y, z	x, y, z	x, y, z
Bi(1)	0, 0, 0.183	0, 0, 0.1989	0, 0, 0.1989	0, 0, 0.2089
Bi(2)	---	---	0, 0.5, 0	
Sr	0.5, 0.5, 0.072	0.5, 0.5, 0.1019	0, 0.5, 0.1091	0.5, 0.5, 0.1352
Ca	----	0.5, 0.5, 0.5	0, 0.5, 0	0.5, 0.5, 0.428
Cu1	0, 0, 0	0, 0, 0.0543	0, 0, 0.0543	0, 0, 0
Cu2	---	---	---	0, 0, 0.0881
O1	0.5, 0, 0.092	0.5, 0, 0.0510	0.25, 0.25, 0.051	0.5, 0, 0
O2	0, 0, 0.092	0, 0, 0.1200	0, 0.5, 0.198	0, 0, 0.1544
O3	0.5, 0.5, 0.187	0.5, 0.5, 0.1980	0, 0, 0.12	0.5, 0.5, 0.2066
O4	----	-----	---	0.5, 0, 0.0857

2.2 Reciprocal space of Bi-2212

Two adjacent Brillouin zones (BZ) of the body centered orthorhombic Bi cuprates, some symmetry points, and the high symmetry directions of Bi-cuprates are shown in FIG. 2.3a. Moreover, the two dimensional Brillouin zone derived from FIG. 2.2c is also depicted in FIG. 2.3b. It can be seen that the M point of the BZ is located between the x and the y direction. It should be

mentioned that the ΓM direction is the direction of the Cu-O bonds. It has found that the d-wave superconducting gap is maximal along the ΓM direction which is called the antinodal direction, and the superconducting gap has a node along the Γ- (X/Y) direction [31]. These aspects will be discussed in chapter 5. The lengths of the reciprocal vector can be found by

$$b_i=2\pi(a_j\times a_k)/V \ (i, j, k\in 1,2,3) \qquad (2\text{-}2)$$

which is 1.65 Å $^{-1}$ and 1.16 Å $^{-1}$ for the tetragonal ($\vec{b}_1=\vec{b}_2$) and the orthorhombic ($\vec{b}_1\neq\vec{b}_2$) structure, respectively.

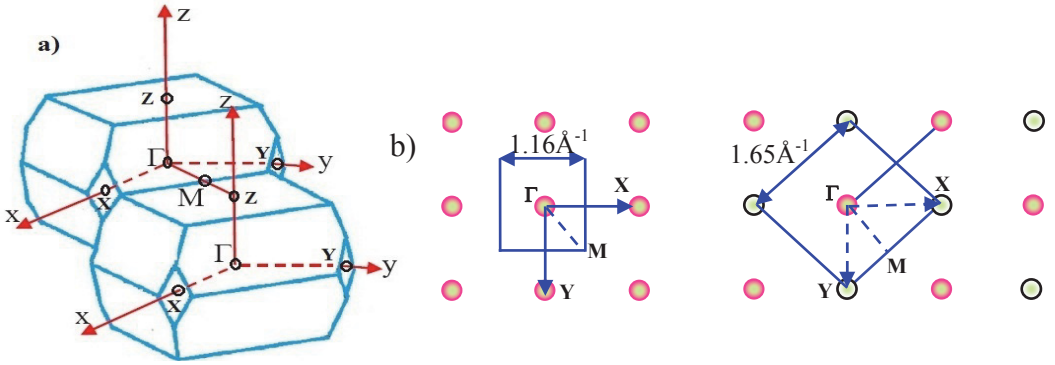

FIG. 2.3: a) Two adjacent Brillouin zones of the body centered orthorhombic structure of the Bi cuprates [32]. b) Two dimensional Brillouin zone as derived from the two-dimensional structure of FIG. 2.2c. Left and right are for orthorhombic and tetragonal structures, respectively [33].

2.3 Phase diagram of the cuprates

A complicated phase diagram is observed in the case of the high-T_C cuprates, which agrees with the phase diagram of the CuO_2-plane as shown in FIG. 2.4. The undoped parent compound consists of a anti-ferromagnetic (AFM) insulator until the AFM- paramagnetic phase transition temperature T_N. Adding charge carriers can be done by two methods, i) by a variation of the oxygen content. ii) by a suitable substitution of cations. The two ways will be discussed in section 3.1. At low temperatures, the electric transport shows a dramatic change from insulating-antiferromagnetic to metallic-superconducting behaviour. The so-called superconductivity dome appears by doping from about 0.08 holes per Cu atom in the CuO_2 planes (assigned underdoped

regime). Maximum critical temperature (T_{Cmax}) occurs at so-called optimal doping which is about 0.16 holes per Cu atom in the CuO_2 planes. By further doping, T_C decreases again (overdoped regime) and superconductivity disappears at about 0.24 holes per Cu atom. Above this hole content a Fermi liquid-like metal is observed for the compound. Presland et al. [34] have discussed that the approximately symmetrical shaped dome of the $T_C(p)$-curve is represented by

$$T_C / T_{C_1 \max} = 1 - 82.6(p - 0.16)^2 \qquad (2\text{-}3)$$

where p is the hole concentration. This empirical formula is generally applied to all high-T_C cuprate families. Dudy [35] has studied the superconducting dome in great detail for Bi-2201 and (Pb, Bi)-2201 and found remarkable deviations from this simple shaped dome behaviour.

At the high hole concentration site of the superconducting dome there is a boundary between a Fermi liquid and non-Fermi liquid phase which is characterized as the transition temperature T_{FL}, i.e. between a correlated Fermi liquid metal and a highly correlated charge transfer (CT) insulator [36]. The aspects of a Fermi liquid will be discussed in the next section. It is a great current debate whether at higher temperatures the cuprates are already CT-insulators [37]. It should be noted that the undoped cuprates are Mott insulators of charge-transfer type because the electron number per unit cell is odd and the uppermost energy band is half-filled and without correlations metallic behavior would be expected. One should note that in a conventional band insulator the spectral weights of the bands below and above the gap are independent of doping while this is not the case for a Mott insulator [38]. On the other hand, one other important well established feature of the phase diagram of cuprates is the pseudogap (PG) formation which is identified as a dip in the electronic density of states (DOS) at the Fermi energy above T_C. Renner et al. [39] have demonstrated by scanning tunnelling spectroscopy that the DOS near the Fermi energy decreases gradually with decreasing temperature below a critical temperature T^*. This is due to PG formation and has been confirmed by several other techniques such as electrical transport [40-42], angle-resolved photoemission spectroscopy [43-45], optical reflectivity [46], nuclear magnetic

resonance [47, 48], thermodynamic measurements [49], and Knight shift [50]. More over, in bilayer and monolayer cuprates the run of T^* has obviously a similar variation with doping [50]. It has been reported that the PG progressively destroys the Fermi surface [51, 52]. These two effects, i.e. the dependence of the Fermi surface on doping and temperature, clearly show the anomaly of the normal state of the cuprates, in particular for underdoped materials. Today, some researchers believe that the PG phase is independent of the phenomenum of high-T_C superconductivity and it should be related to a quantum critical point [53]. On the other hand, others believe that it is due to a pre-pairing of the charge carries [54]. This was initially supported from the detection of a large negative value of the Nernst effect [55-57] and the observation of diamagnetic behavior even above T_C up to T^* [58]. Recently, it has been argued that the PG temperature, T^*, represents the boundary between bound and unbound charge-2e bosons where the binding energy to excite a boson vanishes and a linear-T resistivity is obtained [59].

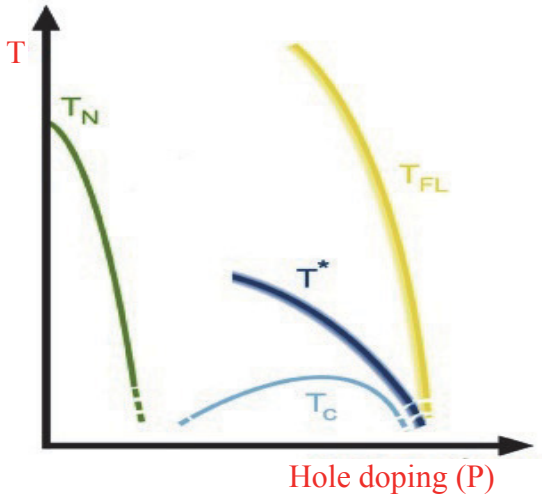

FIG. 2.4: Phase diagram of the CuO_2-plane which is temperature as a function of hole doping. For details see the text.

Furthermore, Chakraborty and Phillips [59] have found that in high-T_C superconductor $La_{2-x}Sr_xCuO_4$ the T^* value can be estimated by

$$T^* \approx \Delta(x)/\ln(x) \qquad (2\text{-}4)$$

where $\Delta(x)$ and x are a characteristic activation energy scale for the system and the amount of doping, respectively.

Finally, it has also been reported that the pseudogap exists also in disordered conventional superconductors [60, 61].

The question how and whether the pseudogap temperature (T^*), the superconducting transition temperature (T_C), the pseudogap energy (E^*), and the superconducting gap energy (Δ_C) are related to each other is tempting and has to be solved. It is not clear how all these characteristic values are related. A final theory, to be found, has to solve and explain all this.

2.4 Crystal growth and characterization

All the single crystals studied in this thesis were grown in Prof. Manzke's group by Dr. A. Krapf, who has extended experience in crystal growth. She used the flux method to grow the Bi(Pb)-2212 single crystals. The flux method should be briefly reviewed here. The reader may also refer to the work of Dudy [35] for more details on the flux method.

The basic components for growing Bi(Pb)-2212 crystals are powders of Bi_2O_3, $SrCO_3$, $CaCO_3$, and CuO, which are mixed as per the desired crystal composition. Ethanol is used to homogenize the mixture. The mixture is then calcined to dissolve the carbonates. After calcination, PbO or LaO can be added to prepare crystals containing additional Lead or Lanthanum, respectively. If this is the case, the mixture is re-dissolved in ethanol. The mixture is casted into a circonium oxide crucible and homogenized by heating above the liquidus temperature for a few hours. The mixture is then cooled to the crystallization and solidus temperatures, respectively. Finally, once the system is stable, the mixture is rapidly cooled to room temperature. Note that the requisite cooling steps are essential for the growth process and affect the desired result. FIG. 2.5 shows typical single crystals in the crucible prepared by the flux method.

Energy dispersive x-ray analysis (EDX) was used to determine the chemical composition of all single crystals. EDX reveals the actual stochiometric

composition of the crystal. The crystal is placed into an electron beam using a scanning-electron-microscope for the EDX analysis. FIG. 2.6 shows the resulting lines of the characteristic x-ray spectrum for a Bi(Pb)-2212 single crystal, measured with a semiconductor detector.

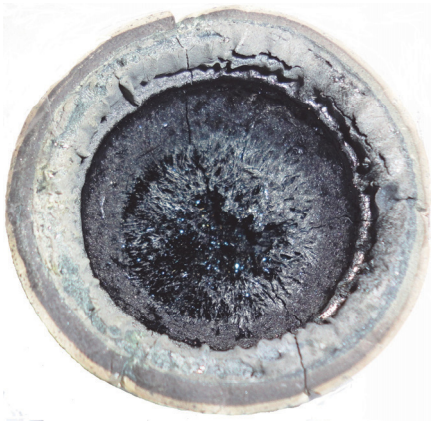

FIG. 2.5: Single crystals, grown by the flux method in a circonium oxide crucible.

The stoichiometric concentrations of the different atoms in a Bi(Pb)-2212 single crystal are given in table 2.2, which were calculated with the PUzaf correction using commercial software [62].

Table 2.2: Stochiometric concentration of Bi(Pb)-2212 single crystal, measured by EDX.

Element/Line	Concentration					
	Hall effect		XAS		ARPES	
	Sample#1	Sample#2	Sample#3	Sample#4	Sample#5	Sample#6
Ca K-alpha	0.92	0.91	0.99	0.99	0.82	0.85
Cu K-alpha	2.26	2.12	2.21	2.21	2.26	2.24
Bi	1.68	1.94	1.74	1.74	1.57	1.59
Pb	0.28	0.16	0.24	0.24	0.39	0.41
Sr	1.85	1.87	1.83	1.83	1.96	1.91

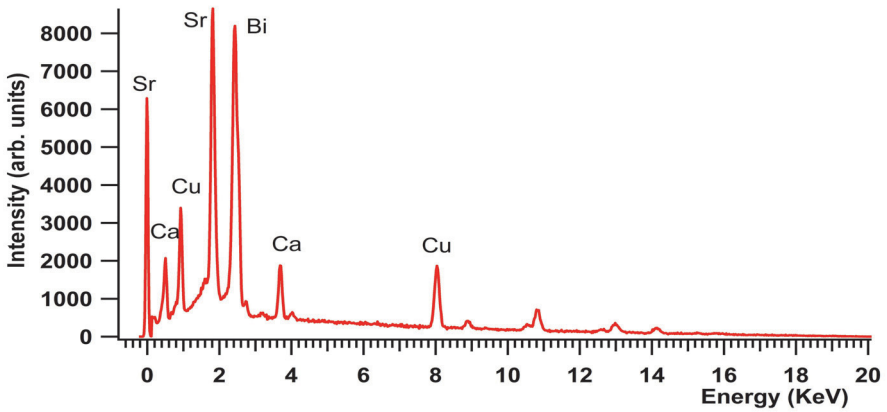

FIG. 2.6: Typical spectrum for a Bi 2212 single crystal measured by the EDX analysis.

The superconducting properties were evaluated by ac-susceptibility. The ac-susceptibility of all samples was measured by a PPMS 6000 Quantum Design maschine at our group. High-T_C cuprates exhibit two critical magnetic fields, H_{c1} and H_{c2}, similar to type II superconductors. This means that an ideal diamagnet phase occurs below Hc_1 when the superconductor is in the Meissner phase. In the region between Hc_1 and H_{c2}, known as the Shubnikov phase, the magnetic field penetrates the superconductor in the form of flux vortices. A typical magnetic moment diagram (ac-susceptibility $\chi = \frac{m}{HV}$ where H and V are magnetic field and volume, respectively) for optimally doped Bi(Pb)-2212 (Sample#6) is shown in FIG. 2.7. High-quality samples have a sharp superconducting transition in the ac-susceptibility and, consequently, a small ΔT in the $\chi(T)$ curve. ΔT is the temperature difference between 10% and 90% of $\chi(T=T_C)$. For instance, ΔT is approximately 4.5 K in FIG. 2.7. Additionally, T_C and ΔT of Bi(Pb)-2212 single crystals from Table 2.2 are presented in Table 2.3.

Table 2.3: T_C and ΔT of Bi(Pb)-2212 single crystals from Table 2.2.

	Sample#1	Sample#2	Sample#3	Sample#4	Sample#5	Sample#6
T_C (K)	93	46	89	84	91	95
ΔT (K)	5	10	4	6	7.5	4.5

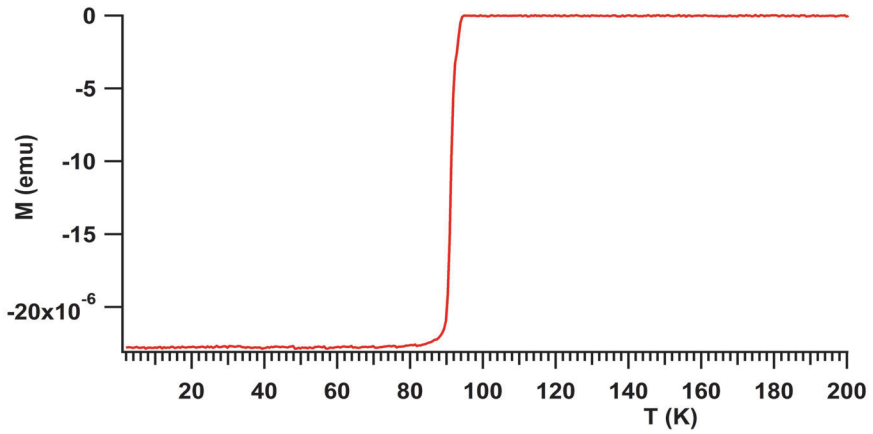

FIG. 2.7: Plot of the magnetic moment (see text) versus temperature for a Pb-doped Bi(Pb)-2212 single crystal (Sample#6) with T_C= 95 K and ΔT=4.5 K.

2.5 Fermi liquid, Marginal Fermi liquid, and Luttinger liquid model

The idea of quasiparticle excitations in the context of interacting Fermi liquid systems has been developed by Landau which is called the Fermi liquid theory [63]. In the FL theory, the excited states of the interacting system are described as in one-to-one correspondence with the excited states of the noninteracting system through "switching on" the pair interactions. Such that the interactions conserve the total particle number, spin, and momentum.

The normal state of conventional superconductors is described completely by the FL picture while there exist strong hints that the normal state of a high-T_C cuprate is not at all Fermi liquid like. Three anomalous features stand out in the normal state. First, the optical reflectance and the resistivity at high temperature are dominated by scattering processes with a linear variation of the scattering rate τ with temperature and frequency [64, 65]. These behaviors can be observed experimentally as a dc resistivity that varies linearly with temperature with a zero intercept on the temperature axis as discussed in Ref. 66. Additionally, by infrared reflectance that varies linearly with frequency, as discussed in Ref. 67. Second, the presence of a pseudogap phases as discussed in the section 2.3, which leads below a temperature T^* to a depression in the density of states at E_F. The depression decreases as the doping is increased.

Third, at low temperature, the development of a sharp scattering resonance in the transport properties of the ab-plane appears. This effect manifests itself as a sharp increase in the ab-plane scattering rate at 500 cm^{-1}. In underdoped materials it takes place below 150 K and in two-layer optimally doped ones near T_C [68]. Additionally, this has been seen in the ARPES dispersion curves as a sharp kink [69]. The kink is due to some scattering process, whereas some groups mean (have hints) that the origin is due to phonons or polarons and others mean due to magnons.

If one accepts that the normal state of a cuprate high-T_C superconductor is non-Fermi liquid like it is natural to search for other explanation for the ground state. In one dimension, for instance, the FL theory of interacting electrons breaks down due to a Peierls instability. Low-lying excitations in a one-dimensional electron gas in terms of bosons can be described by the Luttinger liquid theory. On the other hand, it has been revealed by many experiments that there exists a quasi-1D charge stripes structure [70–77] in the cuprates. Thus, it seems that the transport properties of cuprates could be compared with similar properties of quasi-1D metals. Mourachkine [78] has compared the electrical transport properties of the two cuprates YBCO and Bi-2212 with that of a quasi-one-dimensional conductor. The results point out that i) both $YBa_2Cu_3O_{7-x}$ and Bi2212 exhibit 1D character of the transport properties and ii) there is a steep rise in the ρ_{ab} and ρ_c curves of the cuprates similar to a quasi-1D organic conductor at low temperatures which is due to charge-density-wave ordering.

An intermediate behavior between the Landau Fermi liquid and the Luttinger liquid has been proposed by Varma et al. [79] which is called the 'Marginal Fermi liquid' (MFL) model. They pointed out that several anomalies of the normal state properties of cuprates such as resistivity and optical conductivity could be understood by the MFL phenomenology. For instance, resistivity in optimally doped $La_{2-x}Sr_xCuO_4$ has been found to increase linearly with temperature up to 1000 K without any tendency towards saturation [66]. This dependence was interpreted well within the framework of the MFL theory [79]. While the MFL model is not able to explain other anomalies such as e.g. the

temperature dependence of the Hall effect in the normal state and the magnetoresistance. Furthermore, for near optimal doping where the resistivity behaves linearly with temperature, the expectation is that the cotangent of the Hall angle ($\sigma_{xx}/\ \sigma_{xy}$) should also be linear with T while experimental evidence shows it to be more nearly quadratic. This will be discussed in section 3.3. Also a pseudo gap phase is not explained by the MFL theory. It means that the MFL model is not able to explain all essential new physics of the cuprates. Moreover, recently Wu and Ikeda [80] found by studying the Bogoliubov-de Gennes equation at T≠0 that there exist excited state solutions which are missing in the MFL model. In the MFL picture it is assumed that there exist excitations over a wide range of wave numbers **q** depending only on the ratio ω/T and determining the charge and spin polarizability in the form [79]

$$\operatorname{Im} P(\mathbf{q},\omega) \propto \begin{Bmatrix} -N(0)(\omega/T) & for & |\omega| < T| \\ -N(0)\operatorname{sgn}\omega & for & |\omega| > T| \end{Bmatrix} \qquad (2\text{-}5)$$

where N(0) is the one-particle density of states at the Fermi surface (FS). The interaction of the electrons with these excitations leads to the self-energy [79]

$$\sum(k,\omega) \sim g^2 N^2(0)[\omega \ln(x/\omega_c] - i(\pi/2)x], \qquad x = \max(|\omega|, T) \qquad (2\text{-}6)$$

where g and ω_c are the coupling constant and cutoff energy, respectively. In this case the quasiparticle (QP) weight is given by

$$1/Z = 1 - \frac{\partial \sum'}{\partial \omega} = 1 + g\ln(y/\omega_c), \qquad y = (\max(|E_k - \mu|, T) \qquad (2\text{-}7)$$

while near the Fermi surface, $E_k \to \mu$, and for $T \to 0$ the QP weight vanishes logarithmically, violating the QP picture of the conventional Fermi liquid only marginally [81].

2.6 Hubbard model

The electronic structure of solids based on density functional theory which is a very active area of research in condensed matter physics will be discussed in chapter 6. In this section, the Hubbard model is reviewed which was formulated in the early 1960's. The transition metal monoxides such as FeO,

NiO, and CoO were first candidate compounds with stong electron correlations for an understanding of the behavior of the electronic structure by the Hubbard model. It revealed that they are antiferromagnetic insulators while density functional theory (DFT) with local density approximation (LDA) and generalized gradient approximation (GGA) functionals proposed metallic behavior (as I found similarly with GGA functionals in the DFT calculations reported in section 6.5 for the Bi-2212 compound). Afterwards the Hubbard model has been applied to the understanding of many systems such as heavy fermion systems and high-T_C superconductors respectively, in the 1980's and1990's. Anderson [82] believed that the Hubbard Model is a good model for high-T_C cuprates. The Hubbard model has been investigated by several methods, such as e.g. numerical simulations for finite clusters [83], dynamical mean field theory (DMFT) [84], or the dynamical cluster theory [85]. The Hubbard model often focuses on the half-filled cases because they exhibit a lot of interesting phenomena like Mott insulating behavior, anti-ferromagnetic order, etc.

2.6.1 One band Hubbard model

The Hubbard model is a lattice of "sites" in which a set of electrons hop around from one site to neighboring sites in the lattice. In addition, the spin of each electron can be up or down. According to the Pauli exclusion principle, two electrons on the same site must have opposite spin. Furthermore, a site can accommodate zero, one, or two electrons. One electron orbital per unit cell is considered in the one band Hubbard model (1BH) which is the simplest approximation [86, 87]. This model is specified by two parameters which are the single-electron hopping matrix element *t* between the nearest neighbors and the single-site Coulomb energy U. The Hamiltonian of the Hubbard model consists of kinetic energy and interaction energy what is written respectively, in the Hamiltonian as

$$H = -t\sum_{i\neq j\sigma} c_{i\sigma}^{+} c_{j\sigma} + U\sum_{i} n_{i\uparrow} n_{i\downarrow} \qquad (2\text{-}8)$$

where $c_{j\sigma}(c_{i\sigma}^{+})$ are the annihilation (creation) operators for electrons of spin $\sigma = (\uparrow,\downarrow)$ (index σ labels the electron spin up or down) at the lattice site i and $n_{i\sigma} = c_{i\sigma}^{+} c_{j\sigma}$ is the electron occupation number.

According to the Pauli principle two electrons with opposite spin can be put on one site. Then the electrons interact via a screened Coulomb interaction. This means that the biggest interaction is for two electrons on the same site. While it is zero if the site is empty of electrons or has only a single electron on it.

Both the weak correlation limit ($U << W$) and the strong correlation limit ($U >> W$) can be considered in the Hamiltonian (2-8) where *W=2zt* is the bandwith and z is the number of nearest neighbors [87]. For a square lattice z=4. Two different electronic structures are found for the two limits. A metallic state is observed in the weak correlation limit while in the strong correlations limit, the model describes a Mott-Hubbard insulating state at half-filling with an average occupation electron number n=1. It becomes an unconventional metal under the hole doping (n<1) of the lower Hubbard band (LHB) or under electron doping (n>1) of the upper (UHB). In Ref. 88 a self-consistent moment method is applied to the Hubbard model, they have found antiferromagnetism is stable in a restricted region of *n* around *n*=1.

Only one $Cu3d_{x^2-y^2}$ orbital located in the CuO_2 plane is considered for applying the 1BH for the high-T_C cuprates. Then the Hubbard parameter, U, is described as the Coulomb energy cost to place two electrons at the same site [89]. For instance, in the case of d electrons it can be written as

$$U=E(N_d+1)+ E(N_d-1)-2E(N_d) \qquad (2\text{-}9)$$

where $E(N_d)$ is the ground state energy with N_d electrons of d orbital. (I calculated the Hubbard U by an ab initio method for $CaCuO_2$ and Bi-2212 compounds. This will be discussed in detail in chapter 6).

Applying the 1BH for HTC mattrials has some advantages. Two advantages of the 1BH are that it is able to describe properties such as the Mott-Hubbard metal-insulator transition [90] and antiferromagnetism. Recently, Markiewicz et al. [91] have found that there is a qualitative failure of the 1BH with fixed U to describe the experimental spectra at higher doping. Moreover, they have

revealed that the spectral weight of the UHB collapses with doping at a rate much faster than can be explained in a t-J or U=∞ 1BH. They proposed that such a fast falloff would require a real Mott gap collapse consistent with an intermediate coupling U<W (bandwidth) scenario. Therefore it seems that it is necessary to look at other orbitals for an effective model to describe the cuprates.

2.6.2 Three band Hubbard model

Emery [92] and Varma et al. [93] have proposed the three-band p-d Hubbard model (3BH) in which the copper and oxygen states in the CuO_2 plane are considered (FIG. 2.5a), i.e. a Cu atom that contributes a $d_{x^2-y^2}$ orbital and two O atoms so that one O atom contributes a p_x orbital and the other a p_y orbital. The essential aspects of the electronic structure of the copper plane of the cuprates, which are doped charge transfer insulators, see FIG. 2.4, can be extracted by the 3BH. The Hamiltonian of the 3BH model is obtained by

$$H = \sum_{i\sigma} \varepsilon_i n_{i\sigma} + \sum_{i\neq j\sigma} t_{ij} c^{+}_{i\sigma} c_{j\sigma} + \frac{1}{2}\sum_{i\sigma} U_i n_{i\sigma} n_{i-\sigma} + \frac{1}{2}\sum_{i\neq j\sigma\sigma'} U_{ij} n_{i\sigma} n_{j\sigma'} \quad (2\text{-}10)$$

where $c_{i\sigma}$ ($c^{+}_{i\sigma}$) are the annihilation (creation) operators for holes of spin σ at the copper or oxygen sites i of the square CuO_2 lattice. $n_{i\sigma} = c^{+}_{i\sigma} c_{i\sigma}$ and $\varepsilon_i = (\varepsilon_p, \varepsilon_d)$ are the electron occupation number and energy of the $O2p_\sigma(x,y)$-states and $Cu3d_{x^2-y^2}$-states, respectively, $t_{ij} = (\pm t_{pd}, \pm t_{pp})$ are the transfer integrals for p-d and p-p states on nearest Cu-O and O-O sites, respectively, (FIG. 2.8a). $U_i=(U_d, U_p)$ are the on-site Coulomb repulsion energies for 3d and 2p states and $U_{ij}=(U_{pd}, U_{pp})$ are the intersite Coulomb interactions.

In this model there is one hole per unit cell that is mostly localized on the Cu^{2+} ion with a half spin, given by the CuO_4 (CuO_6) cluster of the undoped CuO_2 layer. The extra hole will form a coherent state on the four oxygen p orbitals around a Cu atom with the hole concentration $n_H = 1+p$.

FIG. 2.8b shows the energy levels in which ε_d, $\varepsilon_d + \varepsilon_p$, $2\varepsilon_p + U_d$ are the local one-hole state and the two next terms representing the local two-hole states,

respectively. The higher energy term $2\varepsilon_p$ of the singlet two p-hole state is not shown. The p-d singlet state ε_2 has the lowest energy of the two-hole states which is called the Zhang-Rice singlet (ZRS) [94]. The charge transfer gap ($\Delta_{pd} \cong \varepsilon_2 - \varepsilon_1$) is determined by the excitation energy for the transition from the one-hole d-like state ε_1 to the two-hole singlet state ε_2. On the other hand, the p-levels are split due to the p-hole hybridization t_{pp} and the charge-transfer gap reduces to $E_{gap}=\Delta_{pd}-t_{pp}$ [95].

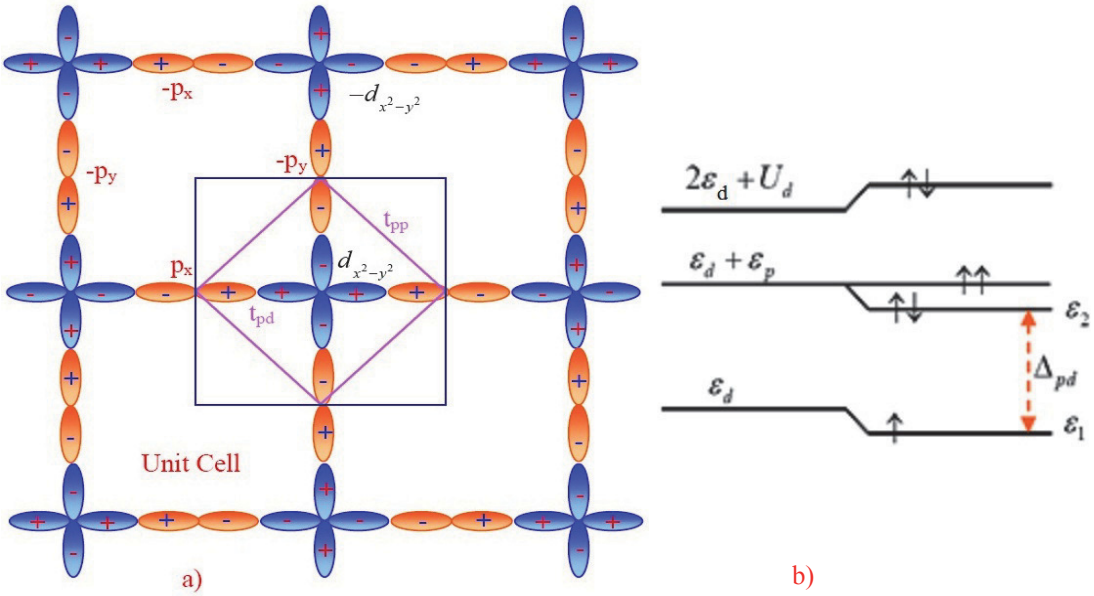

FIG. 2.8: a) A Cu $d_{x^2-y^2}$ orbital interacts with Op_x/p_y orbitals in the CuO_2 plane [53]. For futher explanations see the text. b) Hole energy level of copper and oxygen, respectively, ε_d and ε_p [81].

Recently, the effect of oxygen-oxygen hopping in the 3BH model has been investigated by Wang et al. [96]. Their results point out that as the oxygen-oxygen hopping is varied the physics is changed only slightly. Furthermore, the roles of other d orbitals are supported by some experimental and theoretical results. Therefore, it seems that it is necessary to look beyond the 3BH model such as the five-band Hubbard model discussed in Ref. 97. For instance, a significant contribution of the Cu $d_{3z^2-r^2}$ electrons is revealed by polarized x-ray absorption spectroscopy [98, 99] and electron energy-loss spectroscopy [100].

2.6.3 t-J Model

The t-J model is derived from the Hubbard model when the Coulomb repulsion term, U, in the Hamiltonian is replaced by $J\Sigma S_i \cdot S_j$ which is the Heisenberg term, where the exchange coupling is defined as $J=4t^2/U$. For instance, Ruckenstein et al. [101] proposed typical values for the parameters t and U of 0.4 eV and 3.5 eV, respectively. Furthermore, the t-J model also can be derived from the Hubbard model in the limit $t/U << 1$. Numerical calculations of the t-J model revealed that the hole dispersion might be given by [102-104]

$$\varepsilon(k) \approx t_{eff}(\cos k_x + \cos k_y)^2 \; ; \; t_{eff} = J/2 \qquad (2\text{-}11)$$

From mean-field calculations for the t-J model, it has been obtained that increasing the hole concentration causes the spinon pairing transition temperature T_S to decrease and the Bose condensation temperature T_B to increase [105]. While T_C is considered to be realized in the temperature range where not only fermion (spinon) condensation but also boson (holon) condensation occurs [106]. It is believed that the essential features of cuprates can be explained by the t-J model [107]. Moreover, Macridin et al. [108] have shown that a multiband model and a single band t-t'-U Hubbard model with a significant value of the next-nearest neighbor hopping, t', exhibit a similar low energy physics. For more details about the t-J model the reader should look at ref. [109].

2.6.4 Resonating Valence Bonds model

For the first time Pauling discussed about Resonating Valence Bond (RVB) model states in the context of organic materials. Later, the RVB model has been extended to metals. In 1973, Anderson [110] revived the interest in this concept when he claimed that they are able to explain the Mott insulators. The title of the paper was 'Resonating valence bonds-new kind of insulator'. After

that Anderson also described the copper oxide plane in the La_2CuO_4 as a RVB state [4].

The RVB state is presented by 1BH in which Hamiltonian is described by equation (2-8). Therewith, in equation (2-8), t and U are the hopping integral between neighboring Cu $d_{x^2-y^2}$ sites and on-site Coulomb repulsion on the same Cu site with different spins, respectively. Thus, spin singlet states are formed by localized $d_{x^2-y^2}$ spins of two neighboring Cu atoms. The RVB state is expressed by a superposition of many configurations of the local singlet pairs (FIG. 2.9). In the two-dimensionality of the CuO_2 plane localized spins should have a strong quantum fluctuation effect [106]. Anderson proposed that the ground state of the 1BH at half-filling (the system with one hole per Cu atom) can be described by the RVB state.

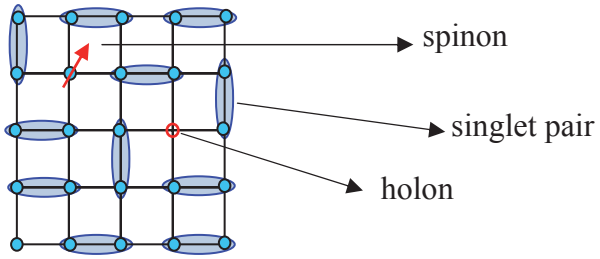

FIG. 2.9: Schematic picture of spinon and holon excitations in the RVB model [106].

In the RVB picture, as a result two kinds of quasiparticle excitations exist which are the so-called spinon and holon. The spinon is a spin 1/2 excitation and the holon is a +e charged spin 0 excitation. For finite hole density the ground state is regarded as the Bose condensed state of holon excitations [106] (FIG. 2.9).

Several essential features of the HTC can be explained by the RVB model such as the superconducting dome, the existence of a pseudo-gap (PG) phase, and the d-wave pairing symmetry. For instance, in the RVB picture the phase diagram of HTC could be explained by considering two temperature scales, T^* and T_{coh}. T^* is a temperature scale in which singlets of the RVB form and T_{coh} is a temperature scale which increases with doping such that the

superconducting carriers become phase coherent below T_{coh}. Thus, as shown in FIG. 2.10 the T_C is determined by the minimum of T^* and T_{coh} as well as in the underdoped samples PG forms for $T_{coh}<T<T^*$ [111]. It means that in this state the RVB singlet pairs still exist however, phase coherence is lost. Thus, in the PG regime by removing an electron from CuO plane a pair is breaked [111].

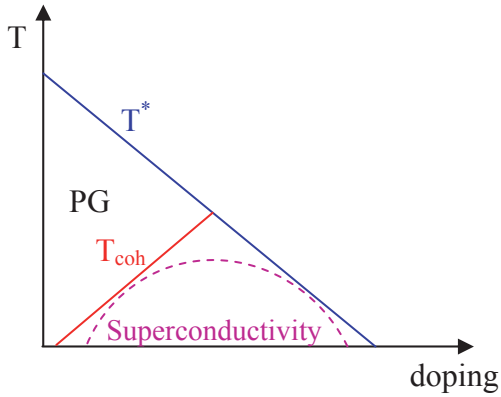

FIG. 2.10: RVB phase diagram, T^* and T_{coh} are singlet paring and phase-coherence temperatures, respectively [111]. For details see the text.

2.7 Negative U centers

The concept of negative U centers was introduced also by Anderson [112] who explained the absence of the paramagnetic states in chalcogenide glasses. The negative U centers is seen in some solids when the ionization energy of an outer electron, E_1, is larger than the ionization energy of a second electron, E_2, which cause them to form a pair particle with binding energy $-U=E_2- E_1$ [113]. One example of negative U center has been observed in the semiconductor PbTe when a small concentration of Tl is used to dope it [114-116].

A close resemblance between the electronic two-dimensionality of cuprates and that of transition metal dichalcogenides (TMD) has been discussed by Klemm [117] and Gabovich and Voitenko [118]. In the TMD the mechanism of charge density wave (CDW) formation is derived by e.g. electron phonon interactions as discussed by Borisenko et al. [9] which could be significant also for superconductivity and CDW formation in HTC. However, it should be noted that some researchers believed that in $TiSe_2$ excitonic coupling is much more

probable. In one and three dimensional metals the electron-phonon interaction can turn the material to an insulator and a superconductor, respectively [9]. For instance in Cu_xTiSe_2, only when the CDW transition reaches zero temperature a superconducting dome appears [11]. As discussed by Liu et al. [119] and Marshall [120] the PG phase in the HTC and the CDW phase in TMD are due to the instability on or near to these saddle bands. It is believed that all these similarities which arise between HTC and TMD are due to the negative U centers conception [113]. In this model, it is assumed that so-called Anderson pairs exist in the material so that they form an ideal Bose gas at a temperature lower than T_C. In this model T_C is given by [113]

$$T_C = \frac{W(1-2\nu)}{\ln(\nu^{-1}-1)}, \quad W = \frac{2zt^2}{U} \qquad (2\text{-}12)$$

W is the band width of the pair band and z, ν, and t are respectively, the number of the nearest neighbors of the given centers, the relative concentration of electronic pairs, and the matrix element for a transition of an electron from negative-U center to the nearest neighbour site. Tsendin et al. [113] believed that this model can explain several properties of HTC. For instance, for band diagram of $YBa_2Cu_3O_{7-x}$ Tsendin et al. [113] have proposed FIG. 2.11. In FIG. 2.11 D^+ and D^- are bands of negative U centers with first E_1 and second E_2 activation energy, respectively. E_C and E_V show conduction and valence bands. For more details about negative-U centers and HTC the reader may refer to Refs. 121-123.

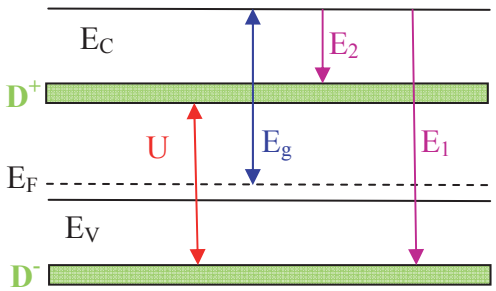

FIG. 2.11: Band diagram of $YBa_2Cu_3O_{7-x}$, D^- and D^+ are bands of negative U centers [113]. For details see the text.

2.8 Stripes and magnetic behavior

An example of a fundamentally new excitation is described by stripes in the electronic systems of HTC where the formation of stripes is not naturally describable in terms of Fermi liquid theory while mean field approaches do predict the formation of stripes [124-126]. It has been accepted that the expulsion of holes from regions of well-formed local moments leads to charge separation and due to two-dimensional electronic structure to one-dimensional charge stripe formation. There are several basic questions which are currently under investigation such as the direction of the stripes in the crystal the charge mobility along and transverse to the stripes [127-128]. There are two views about stripe formation. The first one is that the stripes appear as a compromise which is due to separation between holes and spins, however, the long range Coulomb repulsion frustrates this desire [129, 130]. The second is, stripe formation is caused by short-range interactions [131]. On the other hand, the role of stripes in superconductivity is one central question [126], while it has been argued that static stripes might exist in the superconductivity regime [132, 133]. However, it seems that static stripes are averse to superconductivity where it is supported by commensurability. It stabilizes the largest amplitude of static stripes in the $La_{(1.6-x)}Nd_{0.4}Sr_xCuO_4$ system when x = 1/8 [72]. In Ref. 72 magnetic ordering temperatures (T_m) have been determined by neutron scattering in samples with x = 0.08 and 0.25. The results have revealed that the highest T_m occurs at x = 1/8, which corresponds to a local minimum in the curve of T_C(x) [134].

2.9 Summary

This chapter I introduced several theoretical models, such as the Fermi liquid, the marginal Fermi liquid, and the Luttinger liquid model which are discussed for the nomal state of high-T_C cuprates. In the next chapter, these models will be evaluated in terms of their ability to interpret the temperature-dependent Hall coefficient of the high-T_C cuprate Bi(Pb)-2212. As well as the temperature dependence of the hole density in the CuO_2 plane is interpreted in chapter 4. In

addition, it has been mentioned in this chapter that in the one-band Hubbard model only one electron orbital per unit cell is used to evaluate the electronic structure of high-T_C cuprates. The three-band Hubbard model includes, however, a $d_{x^2-y^2}$ orbital of the Cu atom and the two $p_{x/y}$ orbitals of the oxygen atom. In chapter 4, the role of the other orbitals will be found from the in-plane polarization dependence of CuL_3 and O K edge absorption spectra. This will be accompanied by ARPES data in chapter 5. The role of the Hubbard U parameter for calculating the electronic structure of Bi(Pb)-2212 in the PBE+U method will be discussed in chapter 6.

Chapter 3

The Hall effect in cuprates

The presence of quasi two-dimensional CuO_2 planes is a common characteristic in all high-T_C cuprates (HTC). It is believed that the low energy physics is due to the CuO_2 planes. Two different approaches have been considered after discovery of HTC. A conventional electron-phonon pairing mechanism within the Fermi liquid (FL) picture. On the other hand, a doped Mott insulator picture based on the occurrence of strong electron correlations in the HTC.

In this chapter, the mechanism of doping in the Bi cuprates is discussed. The electronic structure of a CuO_5 pyramid is explained. Under title 'Hall effect in cuprates' the general aspects of the Hall coefficient are reviewed within FL and non-Fermi liquid (NFL) pictures. Additionaly, the measurements of the temperature dependence of the Hall effect of Bi(Pb)-2212 single crystals is presented and discussed.

3.1 Doping of Bi cuprates

In the insulating compound the Cu atoms in the copper oxide plane are Cu^{2+} ions with $4s^0 3d^9$ configuration and spin 1/2. It is well known that the hole carriers are mainly confined to the copper oxide plane. There are two methods of doping in Bi cuprates. The first one is the substitution of cation atoms by other cations with different valance. For instance, the substitution of i) Sr^{2+} by La^{3+} (which produces one electron within the SrO layer) or Bi^{3+} by Pb^{2+} in Bi-2201 and Bi-2212 (which produces one hole). The latter one causes the structural modulation of the Bi-O planes to be suppressed. Or ii) trivalent rare-earth ions such as Pr, Er, and Y substituted to divalent Ca which produces one electron. The second one is the variation of non-stochiometric oxygen probably in the BiO plane which introduces additional holes into the CuO_2 plane.

3.2 Electronic structure of a CuO_5 pyramid

There are two possibilities with respect to the orbitals in the Bi-2212 compound when it is doped with holes [106]. i) The hole occupies an antibonding a_1^* orbital which consists of a Cu d_z^2 orbital and five O p_σ orbitals. In this case both spins are parallel which is called 'Hund's coupling triplet' and which is denoted by ${}^3B_1$ (FIG. 3.1a).

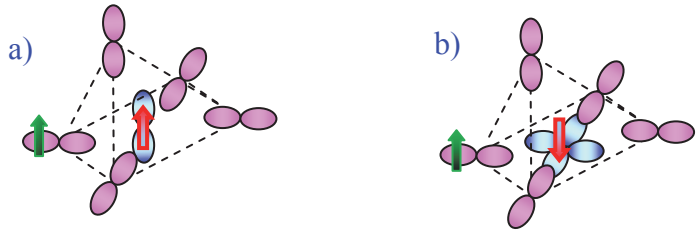

FIG. 3.1: a) and b) Schematic view of the ${}^3B_1$ and a_1^* (ZRS) multiplets, respectively. Red and green arrows represent a localized spin and the spin of a hole carrier, respectively. The solid arrows show the location of Cu d_z^2 and Cu $d_{x^2-y^2}$ for a) and b), respectively [106].

ii) The spins of four in-plane O p_σ orbitals and a Cu $d_{x^2-y^2}$ orbital become antiparallel which is called Zhang-Rice singlet (ZRS) and which is denoted by $^1A_1$ (FIG. 3.1b) [106], as already discussed in section 2.6.2.

It is belived that the satellite line of CuL_3 absorption spectra, which will be discussed in section 4.2, is due to the formation of a ZRS. The satellite peak is characteristic for the absorption of one photon at a site hosting a double hole. These aspects are discussed in the next chapter. Moreover, Ohta et al. [135] have investigated the effect of the apex oxygen on the electronic spectrum of CuO_5 pyramids and CuO_6 octahedrons for clusters with two copper ions, Cu_2O_9 and Cu_2O_{11}. In the case of a doped in-plane hole they found that the stability of the ZRS state strongly depends on $\Delta\varepsilon_A = \varepsilon(p_z) - \varepsilon(p_\sigma)$, where $\varepsilon(p_z)$ and $\varepsilon(p_\sigma)$ are the energy levels of the apex and planar oxygen states, respectively. The singlet state is destroyed when these levels come closer, which is caused by the hybridization increase between the one-hole states on the apex $2p_z$ and the in-plane $2p_\sigma$ oxygen ions. Moreover, recently Peets et al. [136] have measured x-ray absorption spectroscopy of the O K edge of over-doped LSCO and Tl-2201 and then by comparing them to under-doped YBCO they found that their results point to a breakdown of the ZRS picture in the over-doped regime. This experiment is supported by theoretical calculations as discussed in Ref. 137. The theoretical consideration of the multiorbital models which incorporate the $d_{3z^2-r^2}$ state for the CuO_6 cluster has shown that the two-hole triplet $^3B_{1g}$ formed with the participation of the $d_{3z^2-r^2}$ orbital lies only 0.7 eV above the singlet $^1A_{1g}$ term and the crossover between the $^1B_{1g}$ and $^1A_{1g}$ terms is possible with the variation of the model parameters [95, 138]. A similar conclusion has been reported by Kamimura and Eto [139] using the configuration interaction calculations for the CuO_6 cluster. They found that the small reduction of the Cu–axial oxygen distance results in a crossover for the $^3B_{1g}$ and $^1A_{1g}$ two hole terms.

3.3 Hall effect in cuprates

The Hall coefficient is used for the determination of the carrier concentration in ordinary metals and semiconductors. In the Fermi liquid picture the Hall coefficient, R_H, can be calculated according to

$$R_H = 1/n_H e \qquad (3\text{-}1)$$

where n_H is the carrier concentration and e is the electronic charge. From equation (3-1) it can be obtained that i) R_H is inversely proportional to the carrier concentration and ii) both R_H and n_H are temperature independent in conventional metals. Moreover, the Drude theory predicts that the cotangent of the Hall angle and the resistivity show the same temperature behavior because they are determined by the same scattering rate of the charge carriers. The Fermi liquid theory is found to be successful for the description of metals. But it has been observed a deviation from Fermi liquid behavior in correlated electronic systems such as HTC [140]. This is supported by a variety of experimental data where non-Fermi liquid (NFL) behavior has been observed, as already discussed in section 2.5. Thus, the Hall coefficient of the cuprates is not considered to be a useful tool to determine the hole density.

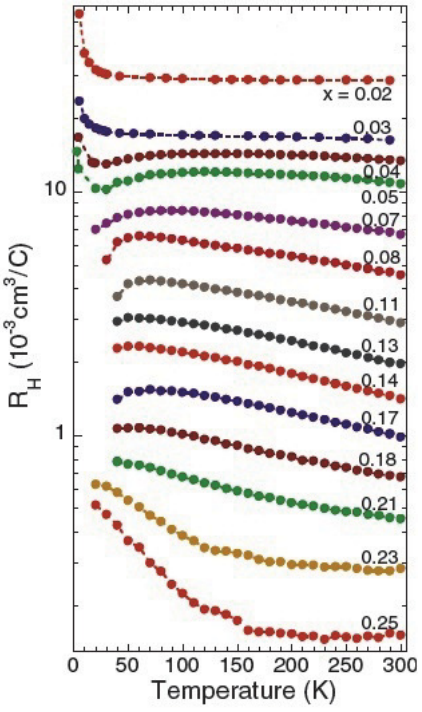

FIG. 3.2: Temperature dependence of R_H for several doping levels in $La_{2-x}Sr_xCuO_4$, from [141].

This is because it shows rather strong temperature dependence. Secondly, for optimum to overdoped samples it vanishes for temperatures below 100 K especially in the Bi-2212 compound. Thirdly, it has a complicated doping dependence. An example for LSCO, $La_{2-x}Sr_xCuO_4$, is shown in FIG. 3.2 [141]. Finally, the cotangent of the Hall angle, $\cot\theta_H=\rho/R_HH$ (where H is the magnetic field and ρ is the resistivity), reveals a quadratic temperature behavior [142]. This is opposed to the observed linear-T resistivity, which seems to be evidence in favor of two scales in the relaxation processes for the carriers as discussed in Ref. 142. Furthemore, as discussed in Ref. 143, sometimes this controversy is referred to as "the separation of lifetimes".

However, Anderson believed that the cotangent of the Hall angle equals to $A+BT^2$ where A vanishes in the most pure samples and it is proportional to the doping, for instance Ni or Zn doping in YBCO, and B is constant for all dopings [144]. For instance, Forro et al. [145] found that Bi-2212 exhibits a strong temperature dependence of the Hall effect through a range of temperatures from 50 to 300 K. The Hall coefficient increases as the temperature is decreased to 100 K. Then it begins to drop as the superconducting regime is approached. This is comparable with my data described in section 3.4. Moreover, Ando et al. [146] reported that R_H is virtually T independent (as in conventional metals) at moderate temperatures in lightly doped $La_{2-x}Sr_xCuO_4$ samples. In the FL picture, the temperature dependence can be caused by an anisotropic scattering time [$\tau_k(E)$] which changes with temperature. Yanase and Yamada [147] believed that the anomalous transport phenomena in HTC are comprehensively understood on the basis of the FL theory by taking into account strong anti-ferromagnetic spin fluctuations. Furthermore, the MFL has not been able to describe the temperature and doping dependence of R_H. For example, for a situation near optimal doping, where the resistivity is linear with temperature, the expectation of MFL is that the cotangent of the Hall angle should also be linear. But experimental data showed that it is nearly quadratic [142]. It seems that it is impossible to derive at simple relation for R_H and n_H for the cuprates. In Ref. [148], the authors have tried to explain the behavior of R_H and the Hall angle

$\cot\theta_H$ by an exact treatment of the local spin fluctuations in the uniform phase of the Falicov-Kimball model. They found that not only the essential features of the T dependence of R_H as well as $\cot\theta_H$ agree with the experimental results, but also R_H as a function of doping changes sign and becomes (for hole doping) negative at around a critical concentration x_C corresponding to a MFL to FL crossover.

Furthermore, within a two-excitation model (in which one assumes τ_{tr} and τ_H as a thermal scattering time and that of spinon excitations, respectively) the complex conductivity can be obtained by [149]

$$\sigma_{\pm} = \frac{n_c e^2 \tau_{tr}}{m_{tr}} \frac{1}{1 - i\omega\tau_{tr}} [1 \pm \frac{i\omega_c \tau_H}{1 - i\omega_c \tau_H}] \qquad (3\text{-}2)$$

Here n_c and m_{tr} are the carrier density and the transport mass, and respectively. ω_c is the cyclotron frequency ($\omega_c = eH/m_H c$). From equation (3-2) it can be obtained that in the limit of $\omega_c \to 0$ and $\tau_H = \tau_{th}$ it reduces to the Anderson result ($A+BT^2$) and a simple Drude model, respectively. Therefore, it seems that the two-excitation model may explain quadratic temperature behavior ($\sim T^2$) of the cotangent of Hall angle.

3.4 Measurements of the Hall effect of Bi(Pb)-2212 single crystals

R_H was determined by using 5-point magnetotransport measurements for two Bi(Pb)-2212 single crystal samples, with T_C=93 K and 46 K. FIG. 3.3 shows for both samples that, as the temperature decreases from room temperature, R_H increases to a maximum at a temperature of approximately 90 K (for optimally doped sample) and 60 K (for underdoped sample) and then decreases. Forro et al. [145] have reported a similar temperature dependence of the Hall coefficient for Bi-2212 single crystals.

Within the FL picture, the temperature dependence of n_H should be the inverse of the R_H temperature dependence. However, XAS measurements of the temperature dependence of n_H show completely different behavior. This behavior will be discussed in section 4.3. This means that the simple

correspondence between R_H and n_H as given in eqution (3-1) could not be valid.

Many models have been proposed to explain the T-dependence of R_H. In Ref. 150, for instance, the two-band model was used to interpret experimental results for R_H and the resistivity ρ_{ab} in $YBa_2Cu_3O_{7-x}$ (YBCO) single crystals.

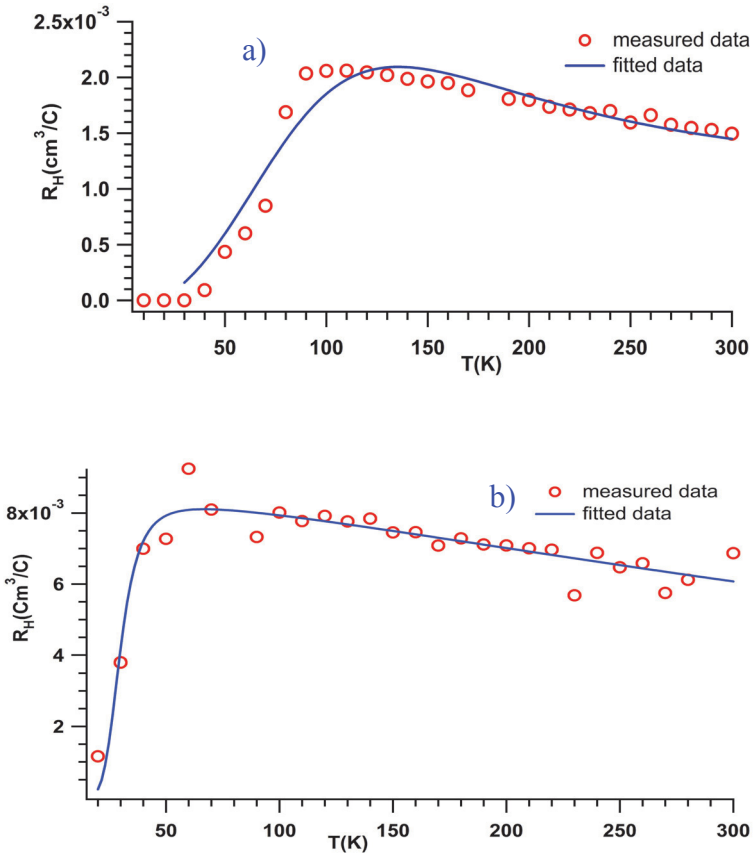

FIG. 3.3: R_H temperature dependence for Bi(Pb)-2212 single crystals in the a) optimally doped and b) underdoped regime.

The authors assumed that there were two types of carriers, electrons and holes, with no temperature dependence. The temperature dependence then comes from charge carrier mobilities given by $\mu_h^{-1} = A(1+BT)$ and $\mu_e^{-1} = C(1+DT)$, where A, B, C, and D are constants and $D \neq B$. Honma et al. [151] and Sanchez et al. [152] have also applied this model to Bi-2212 and Bi-2223 to interpret the temperature dependence of the electrical conductivity and Hall coefficient.

However, the temperature dependence of n_H rules out the two-band model. The temperature dependence of n_H will also be discussed in section 4.3.

Another model can be derived from the t-J model. Within the t-J model for a two-dimensional square lattice, R_H is calculated to be positive, monotonically decreasing with doping, and undergoing a sign change at approximately 1/3 hole-filling. These results agree well with the LSCO [153].
Finally, it should be mentioned that several explanations have been put forward for the anomalous behavior of R_H (T). The problem is reduced to choosing whether the FL or NFL picture provides a more appropriate description of the phenomena. Hussey [143] chose the FL theory and Gor'kov and Teitel'baum [12] chose the NFL theory. Hussey claimed that the anomalous behavior of R_H (T), as described within FL theory, can be explained by the magnitude of a single transport scattering rate. Hussey based his study on evidence for the temperature dependent basal-plane anisotropy of the transport scattering rate, obtained from studies of the angle-dependent interlayer magnetoresistance [154]. Gor'kov and Teitel'baum argued that FL behavior could not be extracted using the product of the temperature dependence of the hole density and the resistivity. MFL can at least explain the T-dependence of the resistivity [66, 79]. Finally, understanding the basic physics of the transport properties of HTC remains an open issue that has not yet been solved.

Chapter 4

X-ray absorption spectroscopy (XAS)

In hole-doped high-T_C cuprates (HTC), the upper Hubbard band (UHB) is an unoccupied state with an energy greater than the Fermi energy. Thus, a technique is needed to probe unoccupied electronic states with energies above the Fermi energy. XAS is used for this purpose. XAS probes the DOS of unoccupied electronic states above the Fermi energy via excitations from core levels. In chapter 6 the use of software will be discussed, such as Wien2K, for modeling the experimental results. In this chapter, the general aspects of the XAS method and its matrix elements are discussed. In addition, the in-plane XAS polarization dependence for Bi(Pb)-2212 single crystals is explained. The temperature dependence of the hole density in Bi(Pb)-2212 derived by XAS is also discussed. The polarization dependence and the temperature dependence are investigated from CuL_3 edge as well as O K edge XAS spectra.

4.1 XAS and matrix elements

Soft x-ray spectroscopy methods involve the production and monitoring of radiative transitions between ground and excited states. In XAS, the interaction between a photon and a core-level electron is normally treated within the one-electron picture. The electron absorbs the photon and is then promoted to a bound, previously unoccupied state. The energy separation between the core level and the unoccupied level is determined by the energy of the absorbed photon [155].

The intensity of an incoming x-ray beam (I_0), which has passed through the sample, is given by

$$I = I_0 e^{-\mu x} \quad (4\text{-}1)$$

where $\mu \approx \rho Z^4/AE^3$ is the absorption coefficient, which depends strongly on the x-ray energy (E), the atomic number (Z), the density (ρ), and the atomic mass (A) of the material [155, 156]. Plotting the absorption coefficient as a function of the incident photon energy (FIG. 4.1 b) produces the following results: i) the absorption coefficient which decreases as the energy of the incident photon increases and ii) several sharp rises, known as absorption edges, at certain energies. The absorption edge is unique to a given absorbing atom and reflects the excitation energy of the inner-shell electrons. The relevant absorption edge for the Cu and O atoms are given in table 4.1). For instance, L edges refer to transitions that excite the 2p electrons, K edges to s electrons.

Typically, the x-ray absorption spectrum is divided into two parts. i) The x-ray absorption near edge structure (XANES) which corresponds to energies up to approximately 60 eV above the edge. This technique can be used to extract information about the unoccupied electronic structure of the material, such as the orbital occupancy, the density of states, and the hole density of the copper planes in cuprates (see section 4.2). ii) The extended x-ray absorption fine structure (EXAFS) is located from approximately 60 eV to 1200 eV above the edge. EXAFS contains detailed information about the local atomic structure. More details on XANES and EXAFS can be found in [155, 157].

The transition probability between the orbitals can be found from Fermi's "golden rule", which is used to evaluate the XAS spectra:

$$W_{i\to f} = \frac{2\pi}{\hbar}\frac{e^2}{m_e^2 c^2} |A_0|^2 |M_{if}|^2 \delta(E_f - E_i - \hbar\omega) \qquad (4\text{-}2)$$

where $M_{if} = < f | e^{i\frac{\omega}{c}\vec{n}.\vec{x}} \hat{\varepsilon}\cdot\vec{P} | i >$ is the matrix element in which $\hat{\varepsilon}$ and $\vec{n}$ are the linear polarization and the propagation direction of the x-ray and $\vec{A} = 2A_0\hat{\varepsilon}\cos(\frac{\omega}{c}\hat{n}\cdot\vec{x} - \omega t)$ is the potential vector. The initial and final states are denoted by *i* and *f*, respectively.

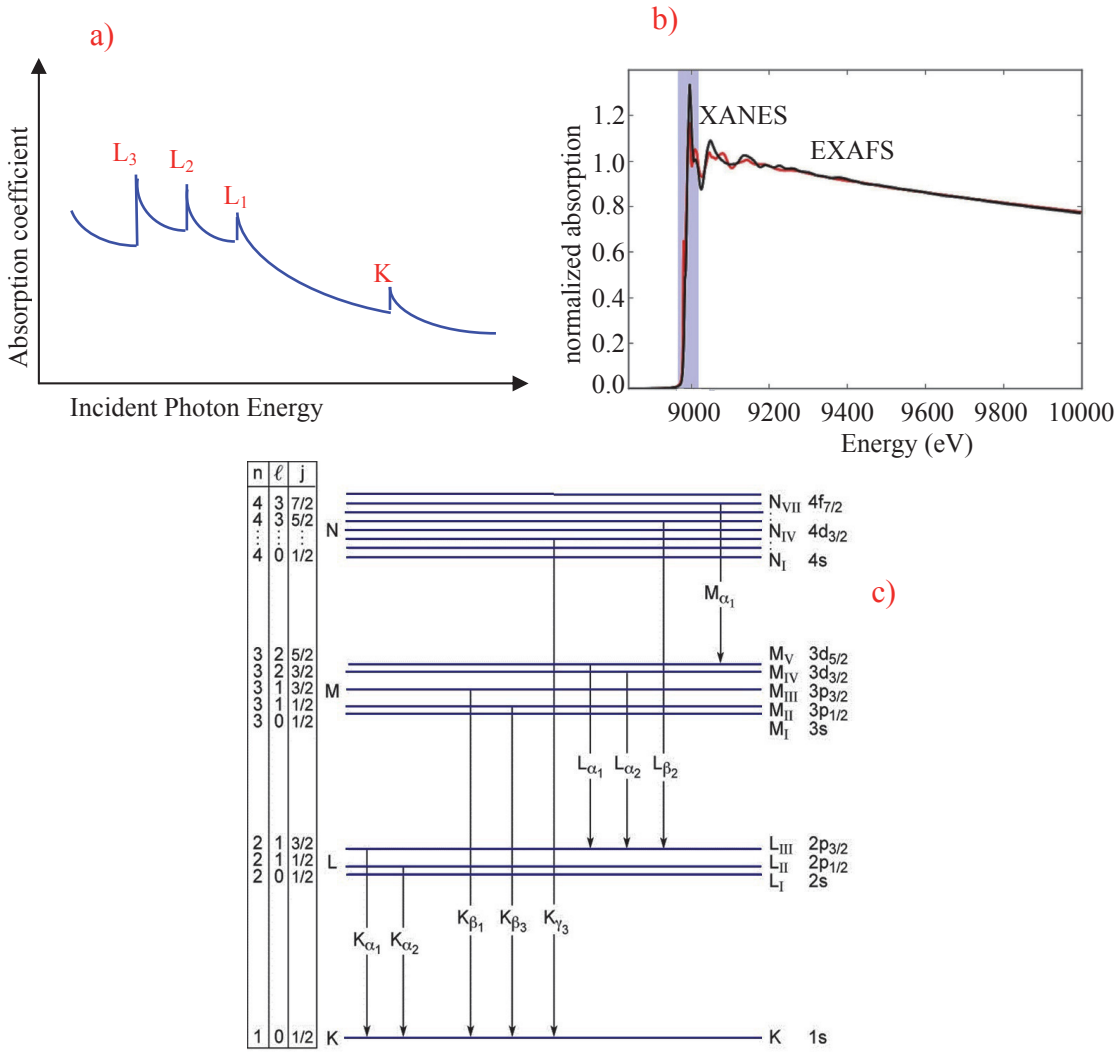

FIG. 4.1: a) X-ray absorption coefficient as a function of the incident photon energy, shown for K, L_1, L_2, and L_3 edges. b) The K-edge XAS spectra of CuO_2 and CuO red and black, respectively [158]. c) Excitations corresponding to the K, L_1, L_2, and L_3 edges for Cu [156].

Table 4.1: Energy of the absorption edges for Cu and O.

edge	Cu $K_{\alpha 1}$	Cu $K_{\alpha 2}$	Cu $K_{\beta 1}$	Cu $L_{\alpha 1}$	Cu $L_{\alpha 2}$	Cu $L_{\beta 1}$	O K
E(eV)	8048	8028	8905	930	930	950	543.1

Because the x-ray wavelength in the radiation field is much larger than atomic dimensions, the electric dipole approximation is used to evaluate the matrix elements (M_{if}) from Fermi's "golden rule", i.e. $e^{i\frac{\omega}{c}\vec{n}\cdot\vec{x}} = 1$. In a spherical basis, the electric dipole operator is an odd-parity irreducible tensor operator of rank one. It follows that M_{if} is nonvanishing only for i and f states with different parity that satisfy the angular momentum relationship $\Delta m = m' - m = \pm 1$. This means that for the case of the L_3 edge, the dipole selection rules select the unoccupied d orbital with orbital angular momentum $m_l = 0,\pm 1$ for E parallel to the z-axis, and with $m_l = 0,\pm 1,\pm 2$ for E normal to the z-axis [159]. Furthermore, for K edge the dipole selection rules select the unoccupied p orbital. By considering $\vec{n}$ along the z-axis and linearly polarized light in the ab plane (i.e. $\hat{\varepsilon} = \cos\varphi\ \hat{i} + \sin\varphi\ \hat{j}$, where the angle φ is measured relative to the x-axis and $\hat{i}$, $\hat{j}$ are unit vectors along the x-axis and y-axis, respectively), the matrix element can be written as

$$M_{if} = < f/\hat{\varepsilon}\cdot\vec{P}/i > = im\omega_{fi}\left(< f/x/i > \cos\varphi + < f/y/i > \sin\varphi\right) = im\omega_{fi}T_{if} \quad (4\text{-}3)$$

where $T_{if} = \left(< f/x/i > \cos\varphi + < f/y/i > \sin\varphi\right)$ and φ is the angle between the x-axis and the polarization $\hat{\varepsilon}$. For calculation of T_{if}, we need to find out the relation between x and y operators with Racah's spherical tensor operators, $C_m^{(l)}$ [155, 160]. They are given by

$$C_m^{(l)} = \sqrt{\frac{4\pi}{2l+1}}Y_{l,m}(\theta,\phi), \qquad (C_m^{(l)})^* = (-1)^m C_{-m}^{(l)}.$$

$$x = r\frac{1}{\sqrt{2}}[C_{-1}^{(1)} - C_1^{(1)}], \qquad y = r\frac{i}{\sqrt{2}}[C_{-1}^{(1)} + C_1^{(1)}]$$

Such that T_{if} leads to

$$T_{if} = \frac{r}{\sqrt{2}}\left(< f/C_{-1}^{(1)} - C_1^{(1)}/i > Cos\,\varphi + < f/C_{-1}^{(1)} + C_1^{(1)}/i > Sin\,\varphi\right) \quad (4\text{-}4)$$

In this notation, the nonvanishing angular momentum of the dipole matrix elements, $< l', m' / C_{-1}^{(1)} / C_1^{(1)} / l, m >$, are [155]

$$< l+1, m+1 / C_1^{(1)} / l, m >= \sqrt{\frac{(l+m+2)(l+m+1)}{2(2l+3)(2l+1)}}, \quad < l-1, m+1 / C_1^{(1)} / l, m >= -\sqrt{\frac{(l-m)(l-m-1)}{2(2l-1)(2l+1)}}$$

$$< l+1, m-1 / C_{-1}^{(1)} / l, m >= \sqrt{\frac{(l+m+2)(l+m+1)}{2(2l+3)(2l+1)}}, \quad < l-1, m-1 / C_{-1}^{(1)} / l, m >= -\sqrt{\frac{(l-m)(l-m-1)}{2(2l-1)(2l+1)}}$$

where l and m are quantum numbers (l=0, 1, and 2 denote the s, p, and d orbitals, respectively) and $-l \le m \le l$. In the next section, equation (4-4) is used to evaluate the XAS spectra at the CuL_3 edge.

4.2 In-plane polarization dependence of XAS

X-ray absorption spectroscopy (XAS) is one of the powerful methods for elucidating the electronic structure. XAS can provide vital information about HTC by probing unoccupied electronic states near the Fermi level. As discussed in section 2.6.2, superconductivity in HTC is known to originate from the CuO_2 planes and their hole densities, which also produces the conductivity of the normal state.

Several methods have been used to evaluate the hole density in HTC, such as thermopower, iodine titration, and the Hall effect [161]. These experimental techniques probe the entire hole density of the sample. XAS, when performed at a Cu-edge, on the other hand, is a very local probe and can therefore probe the hole density of only the CuO_2 planes. These types of experiments have been used to evaluate the hole density in various polycrystalline cuprates: in $La_{2-x}Sr_xCuO_4$ by Ronay et al. [162], in $Bi_2Sr_2CaCu_2O_{8+\delta}$ by Ghigna et al. [163] and Pham et al. [164], in $Bi_{2-x}Pb_xSr_2Ca_{1-x}Y_xCu_2O_{8+\delta}$ by Merrien et al. [165], and in $Bi_2Sr_{2-x}La_xCuO_{6+\delta}$ and $Bi_{2-y}Pb_ySr_{2-x}La_xCuO_{6+\delta}$ by Schneider et al. [166]. The same method was also later applied to HTC single crystals, but the hole content could not be reliably determined initially. Ariffin et al. [167] have discussed that this difficulty was due to not accounting for the linear polarization of the impinging synchrotron light.

In this section, the effects of the change in the in-plane polarization on determining the hole density of weakly underdoped Bi(Pb)-2212 single crystals are studied using XAS. $Bi_{2-y}Pb_ySr_2CaCu_2O_{8+\delta}$ single crystals with T_C=84 K grown from a liquid solution, as discussed in section 2.4. The crystal characterization has been discussed in section 2.4. The XAS measurements were carried out using synchrotron radiation at BESSY II at the PM3 beamline with the HU-BESSY fluorescence spectrometer chamber, which consists of an electron yield (EY) and a fluorescence yield (FY) germanium detector. The setup of the chamber enables spectra to be collected simultaneously by two detectors. Thus, surface and bulk properties could be investigated by EY and FY, respectively. The detectors were located at an angle of 45° to the surface normal and photons impinged at an angle of 0° to the surface normal (FIG. 4.2a). The electric field vector, $\vec{E}$, of the x-ray beam therefore lay within the CuO_2 plane of the crystals (FIG. 4.2b). The pressure in the chamber was less than 10^{-10} mbar during the measurements, and the samples were cleaved in situ.

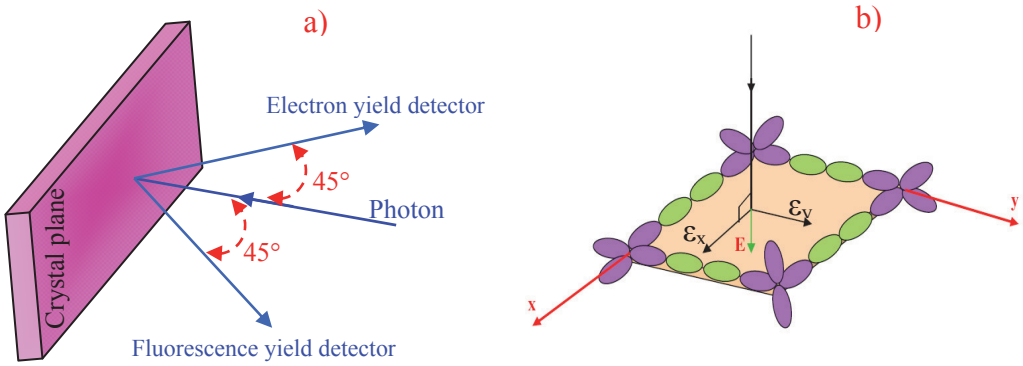

FIG. 4.2: a) Geometry of two detectors located at an angle of 45° to the surface normal, where photons impinge at an angle of 0° to the surface normal. b) The electric field vector, $\vec{E}$, of the x-ray beam lies within the CuO_2 plane of the crystals.

The XAS signal at the CuL_3 edge (925eV-940eV) was recorded at room temperature for azimuthal angles φ between 60° and 236°. The azimuthal angle was measured relative to the b-crystal axis, i.e. the azimuthal angle φ of the electrical field vector of the linearly polarized synchrotron light was

systematically varied in-plane in $1.8° \leq \varphi \leq 20°$ increments. During the measurements, the incident photon flux (I_0) was monitored simultaneously by a gold mesh located after the exit slit of the monochromator. Four scans were performed in each case to obtain good quality statistics. All absorption measurements were normalized to I_0, after which the smooth background was subtracted by a straight line. Each absorption line was fitted by pseudo-Voigt functions. All CuL_3 spectra consisted of two peaks, known as the white line (931.2 eV) and the satellite line (932.2 eV) (see FIG. 4.3a). The peaks were due to dipole transitions from $2p^63d^9 \rightarrow 2p^53d^{10}$ and $2p^63d^9\underline{L} \rightarrow 2p^53d^{10}\underline{L}$, respectively, where the 'ligand hole' $\underline{L}$ denotes a 2p-hole at the oxygen sites surrounding the absorbing Cu atom in the CuO_2 plane. The density of holes per Cu atom for the single crystals was evaluated using a similar method to that given by Ariffin et al. [167] and [168-170], such that

$$n_H = \frac{I_S}{I_S + I_W} \qquad (4\text{-}5)$$

where I_s and I_W denote the intensities of the satellite and white lines, respectively. From equation (4-5), the hole density per Cu atom can be calculated for the entire polarization range from 60° to 236°. The hole density n_H per Cu atom for the entire azimuthal angle series is plotted in FIG. 4.3b in which the CuO bond direction are located at 90° and 180°. Furthermore, the next nearest neighbor oxygens 2nO are at about 67°, 112°, 157.5°, and 202.5°. It should be noted that the spectra of FY has been found similar to EY. Thus, in following the results of EY are presented. FIG. 4.3b reveals a distinct fluctuation in the hole density between 0.136 and 0.155. The average value of the hole density per Cu atom is 0.143. The error bars are due to the statistical uncertainties. To obtain the hole density for the Bi(Pb)-2212 single crystals, we used the same scaling factor of 1.5 as Ref. [167]. The scaling factor is due to geometrical considerations [167]. The average n_H is a reasonable value for the hole density per Cu atom because the T_C of the samples was 84 K, which is close to optimal doping (T_c=95K). Therefore, we refer to the sample as being weakly underdoped. In addition, the average n_H value is validated, using the

empirical formula of Presland et al. [34], as discussed in section 2.3, which produces p=0.132 for our case.

However, such anisotropy is not expected within the dipole approximation theory. One expects the hole density to have the same values for all azimuthal angles in the CuO_2 plane.

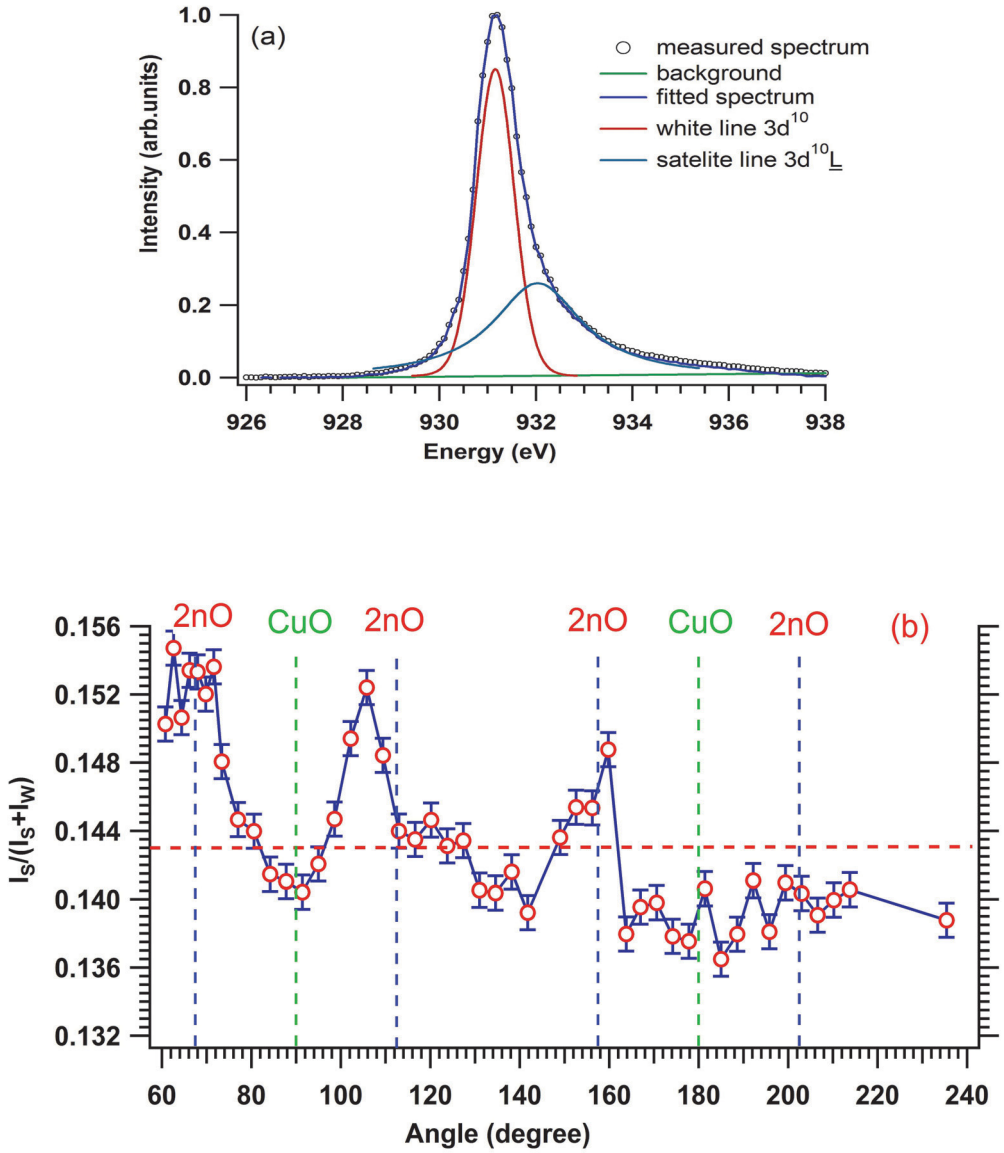

FIG. 4.3: Polarization dependence. a) Two Voigt functions are fitted to the CuL_3 absorption edge of Bi(Pb)-2212 single crystals at 300 K. b) Hole density per Cu atom versus the azimuthal angle φ. The red line is the average density value of 0.143 for the angle φ measured relative to the b-axis. The directions of CuO bonds and second next neighbor oxygen are marked with green and blue broken dashed lines respectively.

The angle dependence of the dipole matrix elements (M_{if}) can be written as

$$M_{if}(\varphi) = < f \mid \hat{\varepsilon} \cdot \vec{P} \mid i > = im\omega_{fi}(< f \mid x \mid i > \cos\varphi + < f \mid x \mid i > \sin\varphi)$$

$$M_{if}(\varphi) = im\omega_{fi}\frac{r}{\sqrt{2}}(< d_{x^2-y^2} \mid C_{-1}^{(1)} - C_{1}^{(1)} \mid p_{3/2} > \cos\varphi + i < d_{x^2-y^2} \mid C_{-1}^{(1)} + C_{1}^{(1)} \mid p_{3/2} > \sin\varphi)$$

$$M_{if}(\varphi) = im\omega_{fi}\frac{r}{\sqrt{2}}\left(\frac{2}{\sqrt{10}}\cos\varphi + i\frac{2}{\sqrt{10}}\sin\varphi\right) = im\omega_{fi}\frac{r}{\sqrt{5}} = const. \qquad (4\text{-}6)$$

where $\hat{\varepsilon}$ denotes the linear polarization direction of the x-ray light, $\vec{P}$ denotes the momentum of the electron, and the $C_m^{(l)}$ are Racah's spherical tensor operators [155, 160], which were introduced in the previous section. The last term of the calculation, the expression (4-6) is a constant. Therefore, an alternate explanation for the observed anisotropy must be found.

The polarisation dependence of the CuL_3 absorption edge has been up to now observed for several Bi(Pb)-2212 single crystals of different hole concentration [171]. Saini et al. [168] have observed a similar clear anisotropy of the XAS measurements of the CuL_3 edge, with the polarization parallel to the two orthogonal Cu-O bond directions in the CuO_2 plane of Bi-2212 single crystals. While these authors detected this anisotropy in only two directions of the copper plane, we have probed the anisotropy in a fine grid of 47 directions in the copper plane.

It has been argued that the experimentally observed lattice displacements in the copper oxide planes are quite complex and anisotropic [172], leading to different Cu-O pair distributions along the a-axis in the orthorhombic and tetragonal crystal structures (i.e. the Cu-Cu or nodal direction and the Cu-O-Cu or antinodal direction, respectively). Therefore, the in-plane polarization dependence could be due to lattice displacements causing an inhomogeneous distribution of the hole density in the CuO_2 plane. Thus, while the unoccupied Cu3d states appear to possess mainly $3d_{x^2-y^2}$-symmetry with some admixture of $3d_{3z^2-r^2}$-symmetry, most of the O2p holes possess (x, y)-symmetry with some holes having p_z-symmetry. This view is supported by O. K Anderson et al. [173], who noted the role of the out-of-plane orbitals. Similar results can also be found in the experiments of the x-ray absorption fine structure of Conradson et al. [174]. Additionally, Bianconi et al. [159] have shown by theoretical

calculations that there exists a 5% component of Cu$d_{3z^2-r^2}$ states at the Fermi level. Moreover, it should be noted that an isolated atom has no orientation dependence in its absorption. The effect of crystallization may produce texture effects at the copper plane. Texture effects may cause an in-plane polarization effect which leads to hole density variations in the CuO_2 plane. These results are also validated by ARPES data at polarizations normal to the mirror plane (see chapter 5). The influence of geometrical anisotropies of the CuO_2 planes, as experimentally observed by EXAFS, as well as electronic extensions by p_z and $d_{3z^2-r^2}$ orbitals has been discussed in several models [123, 175, 176], which argued that the distribution of charge and spin is inhomogeneous in the CuO_2 planes of the cuprates what could possibly explain the observed effects. Finally, an inhomogeneous distribution of the hole density could be due also to the formation of stripes. This is also validated by our ARPES data at four M points of Brillouin zone what is discussed in section 5.4.

On the other hand, Weber et al. [177] submitted that although LDA+ dynamical mean field theory (DMFT) captures the evolution of the ratio of occupancies of the apical and planar oxygens at less than 20% doping, the holes mainly fill the $3d_{x^2-y^2}$ and $p_{x,y}$ orbitals, at larger doping the holes start to fill the $3d_{3z^2-r^2}$ and $p_{\pm z}$ orbitals. Many other models have highlighted the significance of the out-of-plane Cu $3d_{3z^2-r^2}$ and O 2 p_z orbitals in cuprates, such as the five-band Hubbard model [178] and the six-band model [177]. Other studies have considered the suppression of superconductivity by holes at the apical oxygen sites [179, 180] and it is believed that the number of holes in the apical oxygen orbitals increases with doping.

4.3. Temperature dependence of the hole density in Bi(Pb)-2212

The results of this section was published in Physica C and cited as Ref. 181 in this thesis.

One of the most puzzling anomalies of high-T_C cuprates is the strong temperature dependence of the Hall coefficient (R_H) and the hole density (n_H). This has been discussed in section 3.4 where the Hall coefficient first increased

as the temperature decreased to 90 K (for optimally doped crystal), and then decreased upon approaching the superconducting regime. In Ref. 182, for optimal doping, R_H was interpreted as following a 1/T law over a wide temperature range greater than 100 K, in apparent violation of conventional FL theory. Conventional FL theory, which is obtained from Drude theory, gives

$$R_H = \frac{1}{ne} = \frac{V}{n_H e} \qquad (4\text{-}7)$$

where V denotes the unit cell volume, n_H denotes the number of holes per unit cell, n denotes the hole density, and e denotes the elementary charge. The temperature dependence of n_H in cuprates may thus be attributed to the rather strong temperature dependence of R_H. An interesting open question is whether an intrinsic relation can be expected between n_H and R_H, as in simple Drude theory. The temperature dependence of the hole density in Bi(Pb)-2212 single crystals is discussed in this section.

Because the exact hole concentration in Bi-cuprates can not be determined from the chemical composition as easily as in LSCO, for instance, other spectroscopic tools must be found. As discussed in section 4.1, XAS is a powerful technique for probing the unoccupied electronic structure and therefore via hybridization with oxygen states, the hole concentration. However, only a few studies have accounted for the temperature dependence. The XAS technique was used in Refs. 183 and 184 to determine the anomalous temperature dependence of itinerant holes in LSCO and YBCO single crystals for the first time.

To measure the temperature dependence of the hole density, two $Bi_{2-y}Pb_ySr_2CaCu_2O_{8+\delta}$ single crystals, with a fixed lead content of y=0.24, have been used in the weakly underdoped (T_C=84 K) and nearly optimally doped (T_C=89 K) regimes. The crystals were characterized using energy dispersive x-ray analysis (EDX) and ac-susceptibility, as discussed in section 2.4. The XAS measurements were carried out using synchrotron radiation at BESSY II at the PM3 beamline, with the HU-BESSY fluorescence spectrometer chamber. The chamber setup was the same as for the polarization dependence measurements discussed in the previous section 4.2. The XAS

measurements were performed at the CuL_3 edge (925eV-940eV). The electrical field vector $\vec{E}$ of the linearly polarized synchrotron light was aligned parallel to the CuO_2 plane of the crystals. The energy resolution was 100 meV. For each sample, the polarization geometry was held fixed and spectra were taken from room temperature to 10 K in decrements of approximately 10 K. Four scans were made for each case. The incident photon flux (I_0) was monitored simultaneously by a gold mesh located behind the exit slit of the monochromator. All absorption measurements were normalized to I_0, after which the smooth background was subtracted by a straight line. Each absorption line was fitted by a pseudo-Voigt function to account for both intrinsic and experimental broadening, which exhibited Lorentzian and Gaussian shapes, respectively. The chamber set up enabled us to analyze the surface and bulk properties of the superconducting regime up to room temperature by using of an electron yield (EY) and a fluorescence yield (FY) germanium detector.

All of the CuL_3 absorption spectra of the Bi(Pb)-2212 crystals, similar to FIG. 4.3a in the previous section, consist of a main peak at approximately 931.2 eV, known as the white line, that is due to a dipole transition $2p^63d^9 \rightarrow 2p^53d^{10}$ and a shoulder at approximately 1eV above the main peak, called the satellite line, that is associated with the $3d^{10}\underline{L}$ final-state configuration [164]. $\underline{L}$ denotes a $2p$ ligand-hole at the oxygen sites surrounding the absorbing Cu atom in the CuO_2 plane of Bi(Pb)-2212. In other words, this peak is characteristic of the absorption of one photon at a site hosting a double hole, i.e. a Zhang-Rice singlet (ZRS). This peak is given by the $2p^63d^9\underline{L} \rightarrow 2p^53d^{10}\underline{L}$ transition [169, 149, 185, 186]. The hole density per Cu atom in our single crystals is evaluated using equation (4-5), as in the previous section. From equation (4-5), we can calculate the hole density per Cu atom over the entire temperature range from 10 K to 300 K. The comparison clearly reveals that the temperature dependence is a distinct measurable spectroscopic effect. The temperature dependence of the itinerant holes is depicted in FIG. 4.4 a and b for almost optimally doped and underdoped samples, respectively. The term itinerant is adopted from the papers of Garg et al. [184] and Saini et al. [169] with the

implicit idea that the doped holes detected by the satellite intensity are forming the density of carriers. One sees that in the temperature range of T_1 the experimental hole density is at minimum, T_2 is the maximum of n_H at low temperature. In between three areas are defined, whose possible origin will be discussed later.

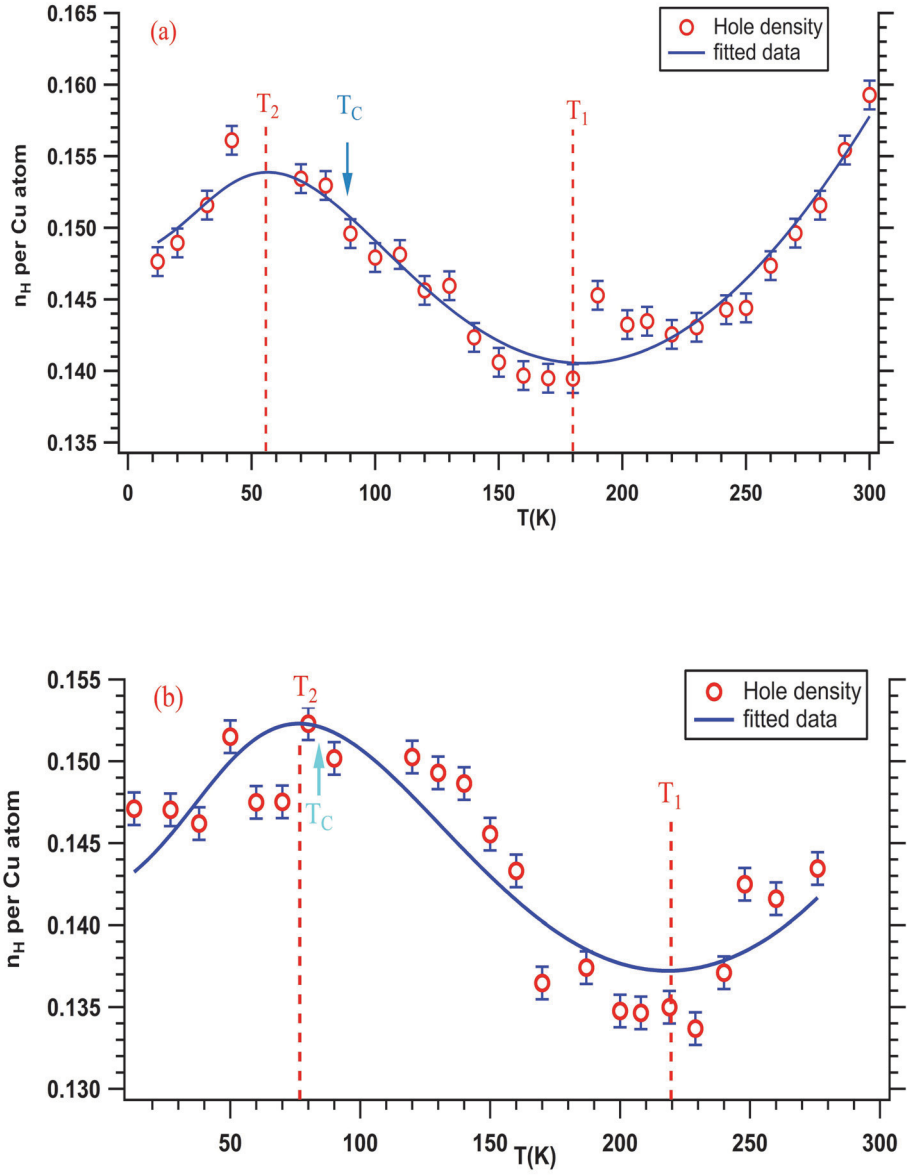

FIG. 4.4: The anomalous temperature dependence of the itinerant hole density n_H of two Bi(Pb)-2212 single crystals for (a) almost optimally doped and (b) underdoped samples, with T_C=89 K and T_C=84 K, respectively. The red circles are experimental data points and the blue lines are a fit to the data.

For instance, in FIG. 4.4a the hole density n_H declines gradually on cooling down and reaches its lowest value of just n_H=0.14 per Cu atom at about 180 K (T_1). It remains almost stable between 180 K and 160 K and then on further cooling rises again reaching a peak value of n_H=0.155 per Cu atom at 50K (T_2), and finally drops again. The trend for underdoped Bi(Pb)-2212 single crystals (FIG. 4.4b) is seen similar with the nearly optimally doped case as the relative change of holes density with temperature is around 20 per cent in both cases. The minimum of the hole density (T_1) and the maximum at lower temperature (T_2) shifts to higher temperature (220 K respectively 80 K).

In both graphs of FIG. 4.4 one minimum (T_1) and one maximum (T_2) in the vicinity of the critical temperature T_C can be identified, which are drawn as broken lines. The minimum around T_1 is quite flat making the hole density there almost stable.

Similar $n_H(T)$ relations and crossover temperatures have been reported from XAS for $La_{2-x}Sr_xCuO_4$ and $YB_2Cu_3O_{7-\delta}$ [183, 184], where they were discussed in the context of an aggregation of holes. Characteristic temperatures were also identified by other methods and discussed with different context and explanation. Based on Rutherford backscattering observed displacement anomalies at comparable temperatures were for instance discussed within a dynamic stripe scenario [187]. In view of the appearance of two characteristic crossover temperatures in the normal state regime of $YBa_2Cu_3O_{7-\delta}$, these temperatures were connected to the stripe phase scenario [54]. In this publication [187], T_1^* was suggested to characterize the aggregation of holes into stripes and T_2^* to correspond to the onset of pairing and superconducting correlations within an isolated stripe. These temperatures lie in the range of our minimum at T_1. In the XAS data of Garg et al. [184] a significant drop in the hole density was reported for YBCO below 100 K as due to Cooper pair formation decreasing the vacant Fermionic states. A similar argument was raised by Sharma et al. [187]. Additionally a comparable behavior has been reported for LSCO [183]. It is common to the last three cited studies and our study on Bi(Pb)-2212 that the number of single particle holes peaks in the

region of T_C and diminishes on both sides, although the YBCO shows more peaks and maxima in the range from 50 K to 200 K than LSCO.

Although these arguments are also in principle capable of describing our results qualitatively, they stay somewhat vague with respect to a quantitative description. Furthermore, it may be noted that for $La_{1.875}Ba_{0.125}CuO_4$, a classical HTC with static stripes, the charge order temperature is just around 50 K and all other ordering like spin ordering occurs at lower temperatures [188]. The range above 50 K to 100 K is generally assumed to be the domain of fluctuating or dynamic stripes.

On the other hand, in several types of experiments structural phase transitions have been observed. i) In acoustic experiments peaks are observed at around 150 and 170 K for Bi-2212 [189]. ii) In the Bi-2212 system a peak between 145 and 167 K is observed in internal friction measurements [190]. iii) Finally, in the Bi-2212 system the behavior of lattice parameters as obtained from neutron diffraction reveals that the b parameter has a distinct minimum at 160 K while a and c lattice parameters vary smoothly [13].

As discussed in section 3.4, the two-band model was used to interpret the temperature dependence of the Hall coefficient in HTC [150-152]. The hole and electron density are both assumed to be temperature-independent in this model, which is not the case in FIG. 4.4. The hole concentration n_H in cuprates has been studied theoretically by Gor'kov and Teitel'baum [12, 191]. Using n_H values derived from Hall effect data of Ref. 192, the authors showed for LSCO that the number of holes per Cu atom, n_H, is given by the relation $n_H=nV_{Cu}$, where n is the hole density and V_{Cu} is the unit volume per Cu, which changes with temperature according to

$$n_H(T,x) = n_0(x) + n_1(x)e^{-\frac{\Delta(x)}{T}} \qquad (4\text{-}8)$$

At low x-values, $n_0(x)=x$ at low x values and n_1 is a constant (n_1= -2.8 for LSCO), but decreases rapidly above x~0.2. The parameter Δ is introduced to denote an activation energy [12]. This framework describes a two-fluid model, which according to Gor'kov and Teitel'baum has a physical origin in the thermal activation of bound electron-hole structures. This idea was further

elaborated by Kusmartsev and Saarela [193]. Ono et al. [192] also used a formula for R_H with two activation energies for undoped and slightly doped high T_c cuprates. The empirical formula of Gor'kov and Teitel'baum (GT) [12] was extracted from the inverse of the Hall coefficient and is appropriate for a two-fluid system. The first component is a temperature-independent constant, while the second component is strongly temperature-dependent and must be considered to be a thermodynamic feature of the system [12].

Of course, the GT formula (4-8) for the thermal behavior of n_H is not sufficient to fit the data in FIG. 4.4 between 15 K and 300 K. To compensate for the inadequacy of the GT formula, we propose that a third term must be added, which is also based on thermodynamic considerations and arises from possible interactions between the hole carriers and the magnetic modes.

In the same manner as Gor'kov and Teitel'baum [12], we assume that the contributions of the individual terms in n_H are additive. The first term, $n_1(x)$, is a constant and represents the largest contribution. In the simplest approximation, $n_1(x)$ is related to the hole concentration from basic Drude theory. The exponential term $n_1(x)e^{-\Delta/T}$ describes the activation of carriers across an activation gap Δ with a characteristic energy. The exponential term produces the strongest effect at elevated temperatures. A new third term, which is given below in equation (4-9), models the interactions between the carriers and excitations of the system in the form of a power law with an exponent α. $n_2(x)$ and $n_3(x)$ are new fitting parameters different from the ones in the GT formula. With this ansatz,

$$n_H(T,x) = n_1(x) + n_2(x)T^{\alpha} + n_3(x)e^{-\frac{\Delta(x)}{T}} \qquad (4\text{-}9)$$

the experimental curves of the two samples were fitted by the least squares method. The fit yielded $\alpha = 1.5 = 3/2$ for the underdoped sample and $1.3 \leq \alpha \leq 1.5 = 3/2$ for the optimally doped sample. We chose $\alpha = 1.5 = 3/2$ for both samples. As a result, we obtained $n_1(x) = 0.142$ and 0.148 for the weakly underdoped sample (T_C=84 K) and the almost optimally doped (T_C=89 K) sample, respectively. This implies that for the optimally doped sample, $n_1(x)$ was very close to the canonical value of 0.16 for optimum doping. Moreover,

Δ=308.4 K and 240.7 K which are equivalent to 0.0265 eV and 0.0207 eV for samples with T_C=84 K and T_C=89 K, respectively. This means that Δ decreases from underdoped to optimally doped samples. The second term, $n_2(x)T^{3/2}$, possibly originates from the interaction of bosonic modes, as discussed below. Phonons are excluded because we assume that phonons are already accounted for by the term $n_0(x)$.

For bosonic excitations, a $T^{3/2}$ term represents the number of magnon modes excited at temperature T, which is known as the Bloch $T^{3/2}$ law in magnetic materials [194]. Therefore, the new term could be due to the number of magnon modes excited at temperature T that interact with the carriers via an exchange interaction. Within this simple approach, the number of free carriers is assumed to be proportional to the number of magnons. Of course, more elaborated theories would be needed to account for the particular shape of the Fermi surface and the details of the magnon modes. Such second-order electron-magnon interactions in antiferromagnetic superconductors have been treated by Machida [195], for instance. In this publication, a detailed theory is developed for a spontaneous magnon emission from an electron and the magnon reabsorption that leads to a change in the electron density of states.

In this context, note (as previously discussed) that reducing the dimension of the crystalline solid to a planar configuration changes the 3/2-exponent towards 1 in the Bloch law [196]. For instance, Crespo et al. [197] have shown that the magnetization approaches a term linear in T for a series of elongated Fe nanoribbons.

The existence of spin excitations in cuprates has been studied by inelastic neutron scattering for some time [198-200]. Because only wave vectors covering 10% of the Brillouin zone are detectable, it is not clear whether the spectral weight of these excitations can sizeably affect the electronic system. On the other hand, evidence for single-magnon excitations could also be investigated by resonant inelastic X-ray scattering (RIXS) at the CuL_3 edge for undoped cuprates [201, 202]. Only very recently, intense paramagnon excitations have been observed using RIXS for a large family of cuprates [201]. Taking advantage of improvements in the RIXS method, the authors

were able to excite paramagnons deep inside the electron-hole continuum (~300 meV).

These observations, together with an inspection of the parameters obtained from fitting the data with the three-term formula of equation (4-9), lead to a number of interesting conclusions. One might expect that the size of $\Delta(x)$= 0.0265 eV and $\Delta(x)$= 0.0207 eV for samples with T_C=84 K and T_C=89 K, which are smaller by a factor of 2.5 to 3 than the values from Gor'kov and Teitel'baum for LSCO [191, 12], better represents the energy scale of the activation effects taking place. This improvement is due to the contribution of the additional exponential term to n_H. The magnitude of the values is strongly reminiscent of the values for the pseudogap. Its possible origin and relation to magnetic excitations or any other source is a matter of ongoing discussion. One is also reminded of the claim by Gor'kov and Teitel'baum that the bound electron hole structure is an origin [12]. The constant $n_1(x)$ contribution to equation (4-9) is varied by the two other temperature-dependent factors by only ~10%, as observed from the parameters shown in FIG. 4.4. Furthermore, the $T^{3/2}$ component has a weaker contribution than the activation component. One can now speculate on whether a two- or a three-fluid system is being considered. In the first case, the break up of magnons would delimit the transition temperature; in the second case, two processes would be competing with each other.

4.4 Temperature and polarization dependence of the O K edge

In addition to the measurements performed at the CuL_3 edge, measurements of the O K edge were also performed on Bi(Pb)-2212 single crystals with T_C=84 K. The chamber setup was the same as for the measurements at the CuL_3 edge in the previous section. The O K edge spectra (525eV to 539eV) were recorded at room temperature using in-plane polarization, such that the azimuthal angle φ is varied from 59° to 220°. The azimuthal angle was measured relative to the b-crystal axis, i.e., the azimuthal angle φ of the electrical field vector of the

linearly polarized synchrotron light was varied systematically in increments of 3.6°. All of the O K edge spectra consisted of two peaks at 528.5 eV and 530.6 eV, which are called the prepeak and peak, respectively (FIG. 4.5a). The prepeak, which is due to the 1s→2p transition, is visible in the hole-doped sample and is known as the Zhang-Rice band. It has been argued that the intensity of the prepeak is proportional to the amount of hole doping. Thus, the values of the prepeak are proportional to the number of itinerant holes in the compound [99, 168, 169, 203]. On the other hand, the higher energy peak, which is approximately 2.1 eV above the prepeak, is visible in the insulating and doped samples. This peak is due to the $1s^2 3d^9 \rightarrow 1s3d^{10}$ transition in the upper Hubbard band, which consists of covalently mixed O 2p and 3d states. In the ground state, the wave function of this band can be written as

$$|\psi>=\alpha|d^9>+\beta|d^{10}\underline{L}> \qquad (4\text{-}10)$$

where $|\alpha|^2$ and $|\beta|^2$ determine the number of 3d holes and the admixture of empty O 2p states, respectively [135]. Using the dipole approximation in the case of in-plane polarization, the electronic states with O-$p_{x,y}$ symmetry can be calculated similarly as in section 4.2 for the CuL_3 edge:

$$M_{if}=<f|\hat{\varepsilon}\cdot\vec{P}|i>im\omega_{fi}\frac{r}{\sqrt{2}}(<p_{3/2}|C_{-1}^{(1)}-C_{1}^{(1)}|s>\cos\varphi+i<p_{3/2}|C_{-1}^{(1)}+C_{1}^{(1)}|s>\sin\varphi)$$

$$M_{if}=im\omega_{fi}\frac{r}{\sqrt{2}}\left(\frac{1}{\sqrt{3}}\cos\varphi+\frac{i}{\sqrt{3}}\sin\varphi\right)=im\omega_{fi}\frac{r}{\sqrt{6}} \qquad (4\text{-}11)$$

where $\hat{\varepsilon}$ denotes the linear polarization direction of the x-ray light, $\vec{P}$ denotes the momentum of the electron, and the $C_m^{(l)}$ are Racah's spherical tensor operators [155, 160]. Note that the second term in the expression above is a constant (i.e. $im\omega_{fi}\frac{r}{\sqrt{6}}$). This means that there is no in-plane polarization expected, while FIG. 4.5b shows that the intensity of the prepeak varies with the angle. As discussed above, the prepeak (the Zhang-Rice band) is visible for the doped sample only and was discussed in section 2.6.2. Thus, from FIG. 4.5b it can be concluded that the hole density, which are formed as ZRS has in-plane polarization behavior. A similar discussion as previously performed for

in-plane polarization of the hole density in section 4.2 can be discussed for polarization dependence of prepeak at the O K edge.

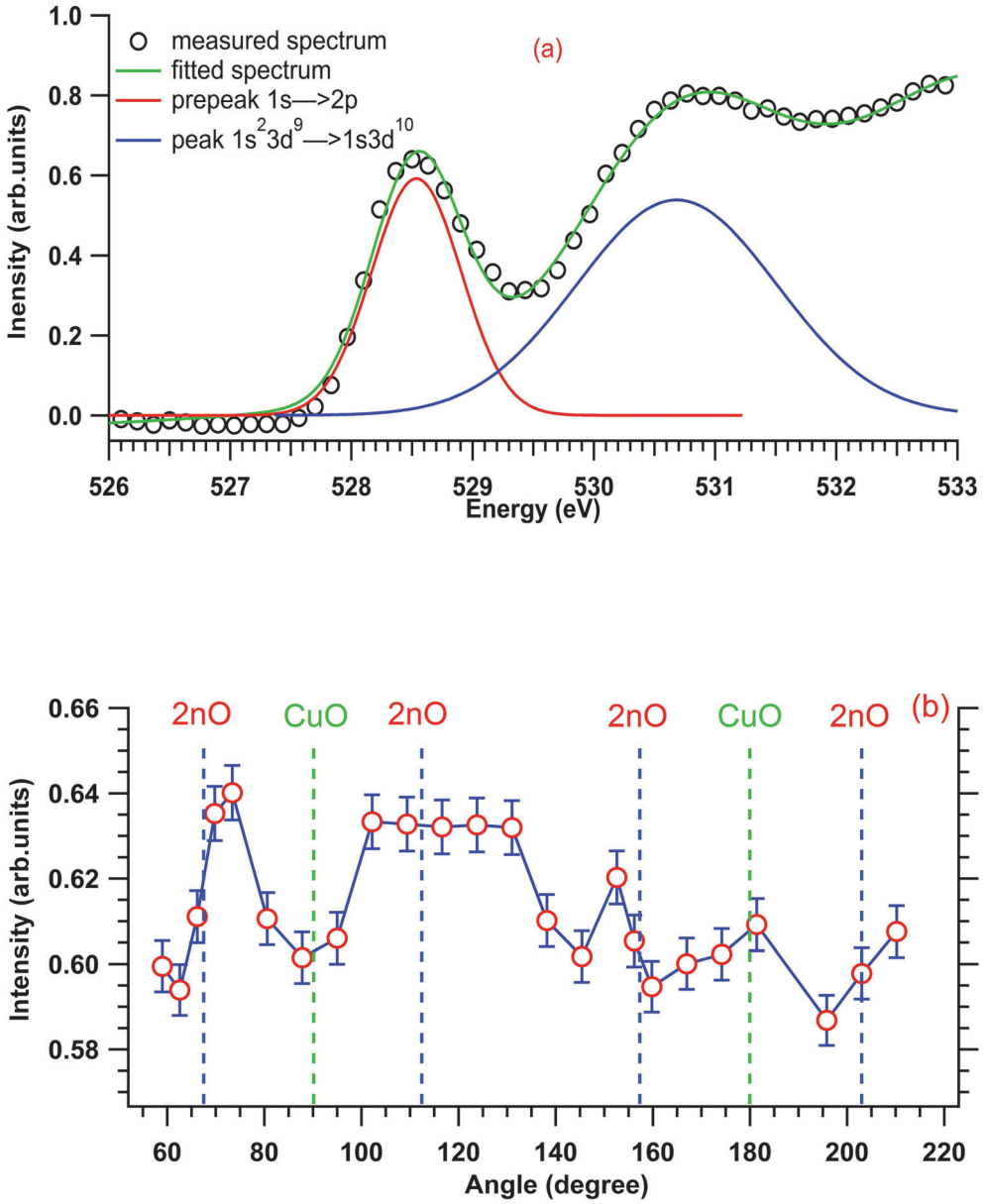

FIG. 4.5: a) Measured spectrum of the O K edge and fitted data: the prepeak and peak are due to the $1s \rightarrow 2p$ and $1s^2 3d^9 \rightarrow 1s3d^{10}$ transitions, respectively. b) The prepeak intensity of underdoped Bi(Pb)-2212 single crystals versus the azimuthal angle. The angle φ is measured relative to the b-axis.

It should be noted that Peets et al. [136] submit that the ZRS picture breaks down in the overdoped regime, as supported by theoretical calculations in Ref. 137. However, Weber [177] has recently calculated that even the inclusion of the apical oxygen did not saturate the occupancy that was observed around doping 0.2, as observed by Peets et al. [136].

On the other hand, the temperature behavior of the O K edge spectra (525eV to 539eV) was investigated at temperatures between 10 K and 300 K. During the measurement, the polarization of the synchrotron light was parallel to the CuO_2 plane at a fixed azimuthal angle of 31°. The angle φ was measured relative to the b-axis. Additionally, the chamber setup was the same as for the measurements at the CuL_3 edge in the previous section. FIG. 4.6 shows the temperature dependence of prepeak intensity, which is almost the same as the temperature dependence of the hole density in the previous section.

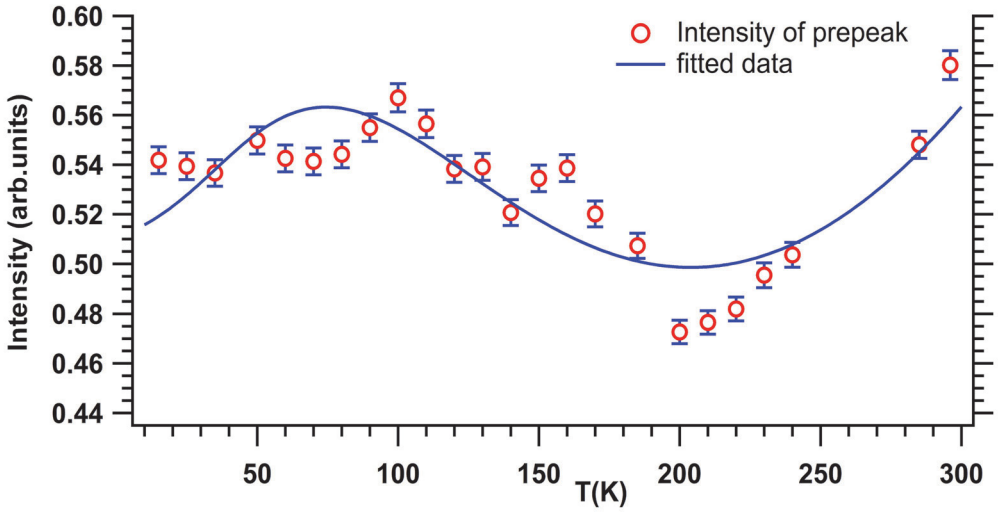

FIG. 4.6: Temperature dependence of the O K edge prepeak intensity is almost the same as the temperature dependence of the hole density at the CuL_3 edge. The spectra were collected at φ=31°. The azimuthal angle was measured relative to the b-axis.

FIG. 4.6 reveals that the prepeak intensity decreased upon cooling, attaining a minimum at approximately 200 K, followed by a rise in the intensity upon further cooling up to a maximum at approximately 100 K, after which the

intensity finally decreased again. However, the fluctuations of prepeak intensity were greater than for the hole density, which was obtained at the CuL_3 edge in the previous section. Finally, the minimum of FIG. 4.6 shifts by about 20K to lower temperature in comparison to FIG. 4.4b.

4.5 Complement

The divalent copper configuration ($3d^9$) is observed for CuO, which is an antiferromagnetic semiconductor with a gap of approximately 1.4 eV [204]. The CuL_3 absorption edge for CuO exhibits a broad white line at 933.2 eV, accompanied by a satellite line on the high-binding energy side at about 9 eV [205]. The satellite line is due to the d^9 configuration in the ground state. In comparison, the CuL_3 absorption edge for CuO_2 has only one peak at 932.4 eV [205], which is narrower than that for CuO. The absence of the satellite line in CuO_2 may be explained in the same way as for nickel dihalides [206-208]. The ground state is approximated by

$$\psi = \cos\theta \mid d^9 > + \sin\theta \mid d^{10}\underline{L} >$$

where cosθ and sinθ depend on the degree of hybridization. In fact, the white and satellite lines in CuO_2 are so close to each other at one peak that they can only be detected using a fitting procedure. The same phenomenon exists for the HTC discussed in section 4.3. Furthermore, as previously discussed in section 4.2, equation (4-5) can be used to calculate the hole density. As discussed in section 4.2, this technique has been used widely for polycrystalline cuprates [162-166] as well as single crystals, such as in Refs. 167 and 168-170. Regarding the polarization of light, two types of polarization geometry can be investigated. The first geometry is called out-of-plane polarization, in which the angle θ between the beam and the crystal plane is varied. This type of polarization has been widely reported in cuprates, such as in Refs. 159, 185, and 186. For instance, Faiz et al. [209] have revealed that the O K edge prepeak intensity is varied by an out-of-plane polarization as shown in FIG. 4.7 for Bi-2212 single crystals. Consequently, Bianconi et al. [159, 185] have attributed the non-zero spectral weight in the E||c-axis orientation to the

presence of Cu 3d holes in the z-direction, i.e. the $3d_{3z^2-r^2}$ band is partially unoccupied.

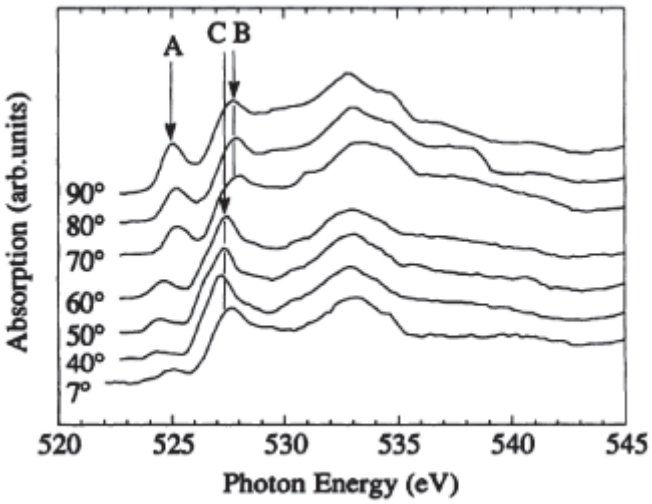

FIG. 4.7: Out-of-plane polarization dependence of the O K edge in Bi-2212 single crystals, from Ref. 209. 90° means in-plane.

The second type of polarization is called in-plane polarization, in which the polarization vector is located in the ab plane of the crystal. This type of polarization has been reported by A.K. Ariffin [167] and B. Müller [171] for (Bi,Pb)-2201 single crystals and was used with the Bi(Pb)-2212 single crystals in this study (see section 4.2). Saini et al. [168] also observed different spectra in Bi-2212 single crystals, using a polarization along the two orthogonal CuO-bond directions. As discussed in section 4.2, this is an unexpected result when using the standard matrix element. B. Müller [171] concluded that the variation in the in-plane hole density follows from a Fourier transform. In addition, following the discussion in section 4.2, I conclude that the in-plane hole density can explained as follows. If we assume that the holes are only located in the $3d_{x^2-y^2}$ orbital, the in-plane polarization is unexpected, as calculated in section 4.2. However, FIG. 4.1c shows that the two transitions $L_{\alpha 1}$ and $L_{\alpha 2}$ are very close to each other for copper and are associated with the $3d_{x^2-y^2}$ and $3d_{3z^2-r^2}$ orbitals, respectively. Thus, similar calculations to those performed in section 4.2 can be performed for the transition to the $3d_{3z^2-r^2}$ orbital. This

calculation results in $T_{if} = \frac{r}{\sqrt{30}}$ in equation 4-4 and 4.6. Therefore, there exist strong evidence for an unisotropic polarization dependence if the occupancy of holes in the $3d_{3z^2-r^2}$ orbital is taken into account. Similar results can be extracted for the in-plane polarization of O K spectra, as discussed in section 4.4. Thus, while the unoccupied Cu3d states appear to possess largely $3d_{x^2-y^2}$-symmetry with an admixture of $3d_{3z^2-r^2}$-symmetry, most O2p holes exhibit (x, y)-symmetry with some holes possessing p_z-symmetry. This view is supported by O. K. Anderson et al. [173], who noted the role of the out-of-plane orbitals. This results is also found from experimental data on the x-ray absorption fine structure by Conradson et al. [174]. Moreover, Weber et al. [177] submitted that although LDA+ dynamical mean field theory (DMFT) captures the evolution of the ratio of occupancies of apical and planar oxygen at less than 20% doping, the holes mainly fill the $3d_{x^2-y^2}$ and $p_{x,y}$ orbitals; at larger doping, the holes start to fill the $3d_{3z^2-r^2}$ and $p_{\pm z}$ orbitals. There have been many other models that focus on the significance of the out-of-plane Cu $3d_{3z^2-r^2}$ and O 2 p_z orbitals in cuprates, such as the five-band Hubbard model [178] and the six-band model [177]. Superconductivity has also been reported to be suppressed by holes at apical oxygen sites [179, 180] and the number of holes in the apical oxygen orbitals is believed to increase with doping. On the other hand, the in-plane polarization of the CuL_3 absorption edge provides a new method for evaluating the hole density of single crystals, as discussed by Ariffin et al. [167] and B. Müller [171]. Here I presented sufficient and new evidence that the in-plane polarization dependence of the XAS signal may microscopically be due to the occupation ratio between states of $3d_{x^2-y^2}$ and $3d_{3z^2-r^2}$ symmetry of the CuO_2 plane of the cuprates.

Chapter 5

Angle resolved photoemission spectroscopy (ARPES)

Angle resolved photoemission spectroscopy (ARPES) is one of the most powerful experimental techniques for mapping the electronic structure of solids. It has been used also to provide valuable information on high-T_C cuprates (HTC). Here, ARPES can be used to study physical properties such as the energy as a function of the wave vector k (band structure) and Fermi surfaces. In this chapter, the basic tenets of ARPES are briefly reviewed in the introduction below. The three-step model and the sudden approximation model are explained. The matrix element for photoemission is also explained. Finally, the temperature and polarization dependence of the DOS at the M point of the Brillouin zones of Bi(Pb)-2212 are presented and discussed.

5.1. Introduction

Hertz discovered the photoelectric effect in 1887 [210]. Photoelectron spectroscopy refers to all techniques based on the application of the photoelectric effect. Einstein [211] explained the phenomenon of the photoelectric effect as being due to the quantum nature of light, where incident light on a sample causes a photon to be absorbed by an electron that then escapes from the material. Therefore, the law of energy conservation can be written as

$$h\nu - E_{kin} = |E_B| - \phi$$

where E_B and ϕ represent the binding energy of the electrons in the solid and the work function (with respect to the Fermi energy E_F), respectively. $h\upsilon$ is the energy of a photon of incident light and E_{kin} is the kinetic energy of the photoemitted electrons. The outgoing electrons are collected by an electron energy analyzer over a finite acceptance angle. Thus, the energy of an electron inside the solid can determined by measuring the kinetic energy of the electron, E_{kin}. This is the principal function of photoemission spectroscopy (FIG. 5.1a). The basic framework of the electronic structure for high-T_C superconductors have been elucidated by angle resolved photoemission spectroscopy (ARPES) [212-214], such as the Fermi surface (FS) mapped in momentum space, the electronic dispersion curve close to the FS, many body effects in electronic excitations, the superconducting gap, and the pseudogap [215-217]. The quality of the sample surface significantly affects data reliability. As ARPES is a surface-sensitive technique, the depth of the photoemitted electron ~10Å for short escapes. Therefore, the Bi-based single crystal is uniquely probed using ARPES for cleavage between the Bi-O layers. This is why ARPES has been used to perform major HTC measurements on Bi-2212 single crystals.

In ARPES experiments, the energy and momentum of the emitted electrons are determined by measuring besides E_{kin} also the angle of the photoemitted electrons. FIG. 5.1b shows the typical geometry of an ARPES experiment. The momentum $\vec{p}$ or the wave vector $\vec{K}$ of the photoelectrons in vacuum can be then determined using

$$\vec{K} = \frac{\vec{p}}{\hbar} \Rightarrow K = \frac{\sqrt{2mE_{kin}}}{\hbar} \qquad (5\text{-}1)$$

where the E_{kin} is the kinetic energy of an electron.

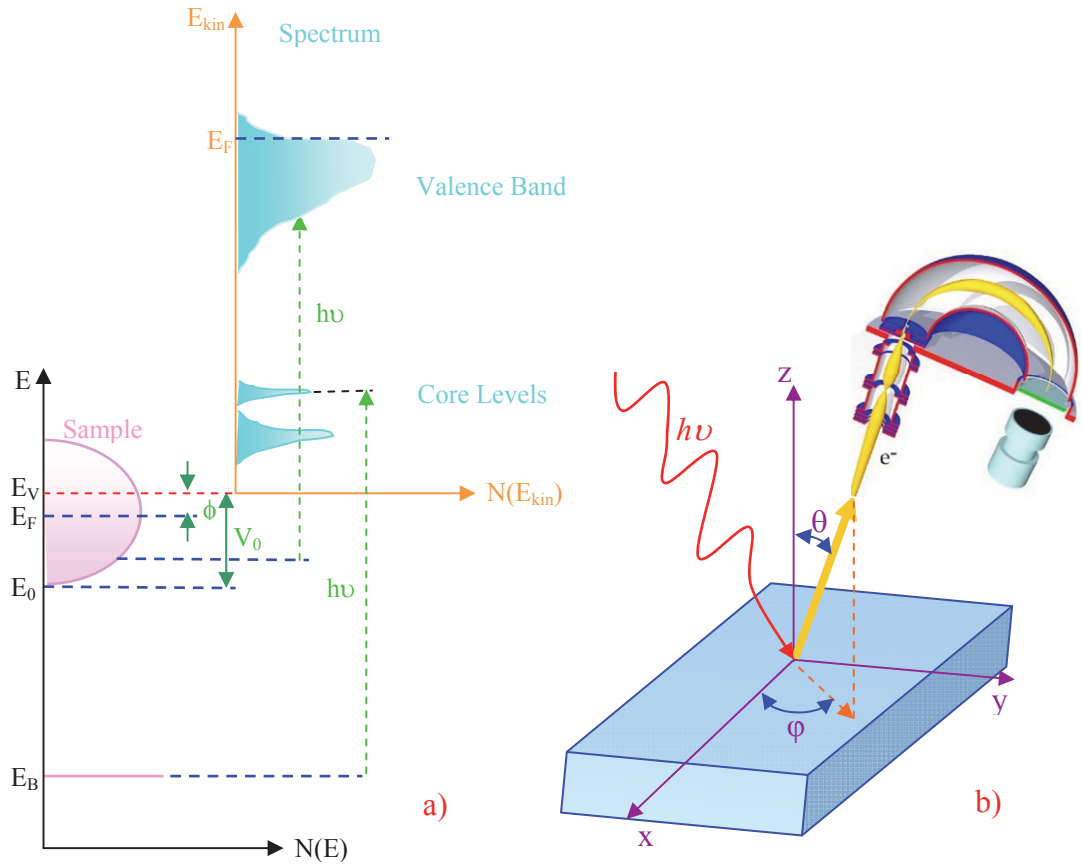

FIG. 5.1: a) Electronic transitions in a photoelectric process. b) Schematic of an ARPES experiment: an incident beam with photon energy $h\nu$ excites photoelectrons at the surface of the sample. For details see the text.

FIG. 5.2 shows that the parallel ($\vec{K}_{\parallel} = \vec{K}_x + \vec{K}_y$) and perpendicular ($\vec{K}_{\perp} = \vec{K}_z$) components of the wave vector in the sample surface (FIG. 5.2b) can be obtained according to

$$K_x = \frac{\sqrt{2mE_{kin}}}{\hbar}\sin\theta\cos\varphi, \quad K_y = \frac{\sqrt{2mE_{kin}}}{\hbar}\sin\theta\sin\varphi, \quad K_z = \frac{\sqrt{2mE_{kin}}}{\hbar}\cos\theta$$
$$K_{\parallel} = \frac{\sqrt{2mE_{kin}}}{\hbar}\sin\theta \qquad (5\text{-}2)$$

where θ and φ are the polar and azimuthal angles, respectively.

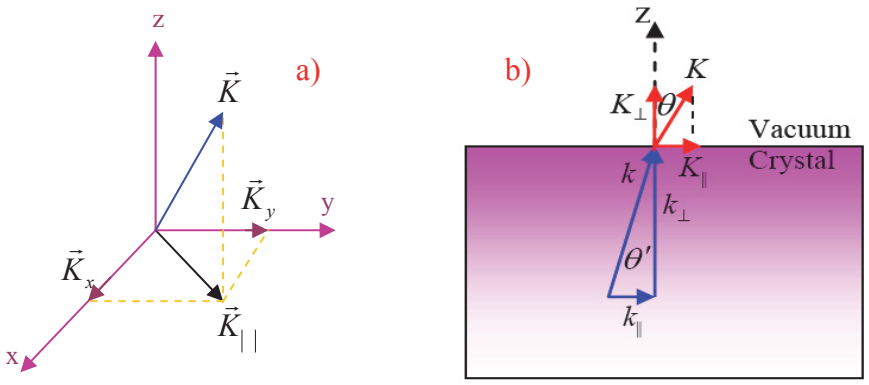

FIG. 5.2: a) Three-dimensional K vector for photoelectrons in vacuum. b) The parallel component of the K vector in the sample surface is conserved both inside and outside the solid.

We seek a relation between the binding energy and the momentum $\boldsymbol{k}$ for the electrons propagating inside the solid. For this purpose, we need to consider the law of momentum conservation, which can be written as follows:

$$K_{//} = k_{//} + G$$

where $k_{//}$ and G are the momentum of the electrons in the solid parallel to the sample surface and a reciprocal lattice vectors G, respectively. The extended-zone scheme produces

$$k_{||} = K_{||} = \frac{\sqrt{2mE_{kin}}}{\hbar}\sin\theta \qquad (5\text{-}3)$$

On the other hand, note that for determining $k_\perp$, the momentum component perpendicular to the sample surface is not conserved due to the abrupt change in the potential along the z-axis. However, $k_\perp$ can be determined if an assumption is made a priori regarding the dispersion of the electron final states in the photoemission process. For instance, the results of the band structure calculation can be used to write

$$E_f(k) = \frac{\hbar^2 k^2}{2m} - |E_0| = \frac{\hbar^2 (k_{||}^2 + k_\perp^2)}{2m} - |E_0| \qquad (5\text{-}4)$$

where E_f and E_0 are referenced to the Fermi energy and the bottom of the valence band, respectively (FIG. 5.1a). After some algebra, $k_\perp$ is finally given by

$$k_{\perp} = \frac{1}{\hbar}\sqrt{2m(E_{kin}\cos^2\theta + V_0)} \qquad (5\text{-}5)$$

where $V_0 = |E_0| + \phi$ is the inner potential (FIG. 5.1a). Therefore, one can obtain $k_{\perp}$ at a known V_0 by measuring E_{kin} and θ. Three methods are used for to determine V_0: i) optimization of the agreement between the experimental and theoretical band structures, ii) equating V_0 to the theoretical zero of the muffin tin potential used in the band structure calculations, and iii) inferring V_0 from the experimentally observed periodicity of the dispersion $E(k_{\perp})$ [218, 219]. From equation (5-3), one can obtain the momentum resolution by

$$\Delta k_{||} = \frac{\sqrt{2mE_{kin}}}{\hbar}\cos\theta\ \Delta\theta \qquad (5\text{-}6)$$

where $\Delta\theta$ corresponds to the finite acceptance angle of the electron analyzer. This equation indicates that the momentum resolution is better at lower photon energies. Moreover, working at low photon energies is advantageous because the photon momentum can be neglected: for instance, for 100 eV energy photons, the momentum is 3% (0.05 $Å^{-1}$) of the typical size of the Brillouin-zone of cuprates. (The BZ was discussed in section 2.2, where $2\pi/a = 1.65^{\circ}A^{-1}$). On the other hand, in my measurements all spectra were taken using a HeIα line (our ARPES system is equipped with a resonance lamp). For a photon energy of 21.2 eV, the momentum resolution is 5% (0.008 $Å^{-1}$) of the typical size of the Brillouin-zone of the Bi-cuprates [69] with the typical angle resolution of $\Delta\theta = 0.1^{\circ}$ of the used Scienta analyzer. The reader may refer to Refs. 220 and 221 for further details on photoemission theory and photoemission spectra calculations.

5.2 Three-step model and the sudden approximation

Fermi's golden rule is used to calculate the transition probability W_{fi} for an optical excitation between the N-electron ground state ψ_i^N and one of the possible final states ψ_f^N :

$$W_{fi} = \frac{2\pi}{\hbar}\left|M_{fi}\right|^2 \delta(E_f^N - E_i^N - h\nu) \qquad (5\text{-}7)$$

where $E_i^N = E_i^{N-1} - E_B^k$ and $E_f^N = E_f^{N-1} + E_{kin}$ are the energies of the initial and final states of the *N*-particle system, respectively (E_B^k is the binding energy of a photoelectron with kinetic energy E_{kin} and momentum k). M_{fi} is called a matrix element (see next section), which is obtained from

$$\prec \psi_f^N \left| H_{\text{int}} \right| \psi_i^N \succ \quad (5\text{-}8)$$

where H_{int} with A^2 omitted (in the linear optical regime A^2 is negligible relative to the linear terms) is given by

$$H_{\text{int}} = \frac{e}{2mc}(\vec{A}\cdot\vec{p} + \vec{p}\cdot\vec{A}) = \frac{e}{mc}\vec{A}\cdot\vec{p} \text{ which is satisfied if } \nabla\cdot\vec{A} = 0 . \quad (5\text{-}9)$$

Here $\vec{p}$ is the electronic momentum operator and $\vec{A}$ is the electromagnetic vector potential, given as

$$\vec{A} = 2A_0\hat{\varepsilon}\cos(\frac{\omega}{c}\vec{n}\cdot\vec{x} - \omega t) \qquad (5\text{-}10)$$

where $\hat{\varepsilon}$ and $\hat{n}$ are the linear polarization and the propagation direction, respectively.

In the one-step model, photon absorption and electron emission and detection are treated as a single coherent process. Berglund and Spicer [222] proposed the three-step model to model the complexity of the actual process. Within this formalism, three steps are assumed for the photoemission process: excitation of the electrons in the bulk, transport of the excited electrons to the surface, and emission of the photoelectrons to the vacuum. The total photoemission intensity is then given by the product of three independent terms, i.e. the total probability for the excitation of the bulk electrons, the scattering probability for the traveling electrons, and the transmission probability through the surface potential barrier.

In the first step, the internal energy of the photoexcited electron in the reduced zone scheme is given by

$$N_{\text{int}}(E,\hbar\omega) \propto \sum_{f,i} |M_{fi}^1(k_i,k_f)|^2 \,\delta(E_f(k_f) - E_i(k_i) - \hbar\omega)\delta(E - E_f(k_f) - \phi) \quad (5\text{-}11)$$

where $E_i(k_i)$ is the energy of the initial bands, $E_f(k_f)$ is the energy of the final band, and $M_{fi}^1(k_i,k_f)$ is the matrix element. The first delta function imposes

energy conservation during the excitation, while the second delta function ensures that the kinetic energy measured outside the sample equals the energy of the final state inside the sample minus the work function. In the second step, the electron-electron interaction is the dominant scattering mechanism, reducing the number of photoexcited electrons reaching the surface with energy E_f. For an isotropic scattering frequency that depends only on the energy E, the electron inelastic mean free path is given by

$$\lambda(E,k) = \tau v_g = (\frac{\tau}{\hbar})\frac{dE}{dk} \qquad (5\text{-}12)$$

where τ is the lifetime and v_g is the group velocity in the final state. A typical value for the mean free path is approximately 10 Å, which makes ARPES so surface-sensitive (FIG. 5.3).

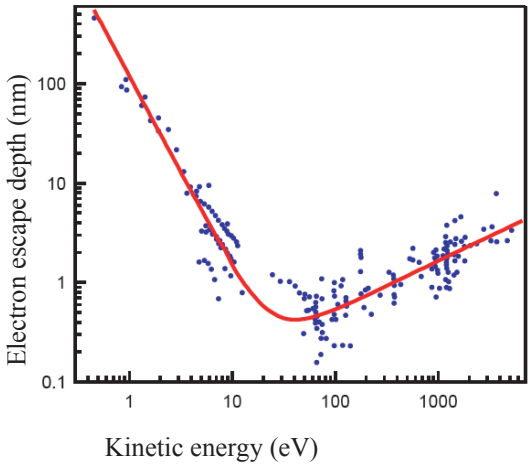

FIG. 5.3: Escape depth of a photoemitted electron as a function of the kinetic energy [223]. Elements and inorganic compounds have been observed to follow this universal curve.

In the final step, the electron escapes into the vacuum under the following condition:

$$(\hbar^2 / 2m)K_\perp^2 \geq E_v - E_0 \qquad (5\text{-}13)$$

where E_0 and $K_\perp$ are the energy of the bottom of the valence band and the perpendicular component of the wave vector of the excited electron,

respectively. E_v is the vacuum energy level. Snell's law can be used to model the excited electron:

$$k_{||} = \sin\theta\sqrt{\frac{2m}{\hbar^2}E_{kin}} = \sin\theta'\sqrt{\frac{2m}{\hbar^2}(E_{kin}+V_0)} \qquad (5\text{-}14)$$

where θ and θ' denote the angles outside and inside the sample, respectively [218]. Accordingly, the critical angle for emission is given by

$$(\sin\theta')_{Max} = \sqrt{\frac{E_{kin}}{E_{kin}+V_0}} \qquad (5\text{-}15)$$

On the other hand, the sudden approximation is used within the many body picture for calculating photoemission spectra. In this limit, it is assumed that the photoemission process is sudden, i.e. an electron is removed instantaneously and the effective potential of the system changes discontinuously at the instant of removal [219]. The ARPES intensity is thus written as

$$I(\boldsymbol{k},\omega)=I_0(\boldsymbol{k})f(\omega)A(\boldsymbol{k},\omega) \qquad (5\text{-}16)$$

where k, ω, and $I_0(\boldsymbol{k})$ are the momentum parallel to the surface, the excitation energy measured relative to the Fermi level, and the squared matrix element, respectively. $I_0(\boldsymbol{k})$ determines the dependence of $I(\boldsymbol{k}, \omega)$ on the polarization of the incident photon which is discussed in next section. The other two terms, i.e. the Fermi function $f(\omega)$ and the spectral function $A(\boldsymbol{k}, \omega)$ (which is proportional to the imaginary part of the single electron Green's function, $A(\boldsymbol{k}, \omega) = (-1/\pi)\mathrm{Im}G(\boldsymbol{k}, \omega+iO^+)$) can be written as

$$f(\omega)=[\exp(\beta\omega)+1]^{-1},\ \beta=(K_BT)^{-1}$$

$$A(k,\omega)= A_-(k,\omega)+ A_+(k,\omega)$$

where $A_-(k,\omega)$ and $A_+(k,\omega)$ are terms corresponding to electron-removal and electron-addition, respectively, that are given by

$$A_\pm(k,\omega) = Z^{-1}\sum_{nm\sigma}\exp(-\beta E_m^N)\left|\prec\psi_n^{N\pm1}\left|a_{k\sigma}\right|\psi_m^N\succ\right|^2\delta(\omega\pm E_m^{N\pm1}\mp E_m^N) \qquad (5\text{-}17)$$

where $a_{k\sigma}=c_{k\sigma}^+$ and $c_{k\sigma}$ for A_+ and A_-, respectively $c_{k\sigma}^+ / c_{k\sigma}$ are the creation/annihilation operators for an electron with momentum k and spin σ.

ψ_m^N is the wavefunction of the *m*-th eigenstate with energy E_m^N, and $Z = \sum_m \exp(-\beta E_m^N)$ is the partition function. Finally, $f(\omega)A(k,\omega) = A_-(k,\omega)$, providing ARPES is used to investigate the occupied states. Further details on ARPES can be found in Ref. 69.

5.3 Matrix elements

Several types of information, such as the shape of the valence band, the parity and the symmetry of the initial state, can be extracted from the ARPES matrix element [224-229]. In the previous section, the matrix element was found by using equation (5-8) with the Hamiltonian defined in equation (5-9). Thus, the matrix element is written as

$$M_{fi} = \frac{e}{mc} < f \mid \vec{A} \cdot \vec{P} \mid i > \qquad (5\text{-}18)$$

Hermanson [224] has explained how ARPES can be used to determine wave function symmetry. The matrix element must clearly be even for a non-zero intensity. Each operator of the matrix element shall now be elaborated on. The final state is a plane wave $e^{-i\vec{k}\cdot\vec{r}}$ which is a momentum eigenket. The momentum operator anticommutes with the parity operator, i.e. $\{\pi, P\}=0$, such that the plane wave is not expected to be a parity eigenket. Thus, the plane wave does not have specific parity. However, with respect to reflection, the final state and the momentum of the final state is located in the mirror plane (plane C in FIG. 5.4c) and has even symmetry; if the final state were odd, the wave function would vanish at the detector (FIG. 5.4) [230]. With respect to the mirror plane $\vec{A}$ can be odd or even when it is normal or parallel to mirror plane, respectively. Thus, $\vec{A} \cdot \vec{P}$ is odd when the polarization is normal to mirror plane and even when the polarization is parallel to mirror plane. Finally, the initial state consists of hybridized Cu3d-O2p states as shown in FIG. 5.4, which possess even symmetry with respect to the (0,0)-(π,0) direction (plane C in FIG. 5.4) and odd symmetry with respect to the (0,0)-(π,π) direction (plane D in FIG. 5.4).

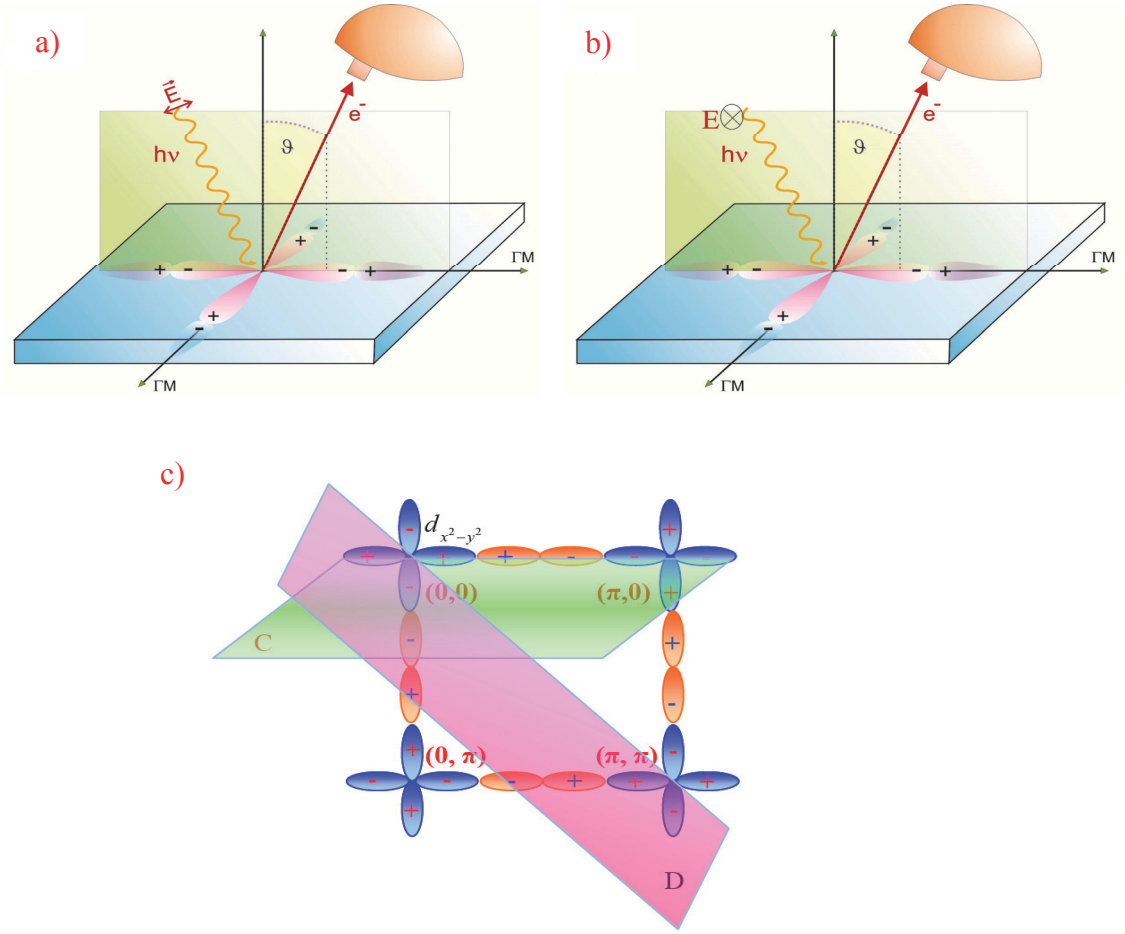

FIG. 5.4: Polarization geometry for the polarization vector. a) In the mirror plane and b) normal to the mirror plane. c) Symmetrical points in the Brillouin zone and two mirror planes, C and D. The initial state consists of hybridized Cu3d-O2p states. The initial state has even symmetry with respect to the (0,0)-(π,0) direction (plane C) and odd parity with respect to the (0,0)-(π,π) direction (plane D).

Table 5.1 shows the symmetry of the matrix element in two different polarizations, with respect to the (0,0)-(π,0) direction (i.e. the CuO-bond direction). It can be concluded that no intensity is observed when the measurement is performed at a polarization normal to the mirror plane. However, we shall see in the next section that a non-zero intensity is indeed

observed for polarization normal to the mirror plane. A possible explanation for this behavior is also given in the following section.

Table 5.1: The symmetry of the photoemission matrix element for two different polarization geometries with respect to the (0,0)-(π,0) direction of the CuO_2 plane of Cuprates.

	$< f \|$	$\vec{A} \cdot \vec{P}$	$\| i >$	$< f \| \vec{A} \cdot \vec{P} \| i >$	intensity
$\varepsilon_{\perp}$	even	odd	even	odd	0
$\varepsilon_{\|\|}$	even	even	even	even	≠0

5.4 Spectral line shape at the M point of the Brillouin zone

The results of this section will submitt to Phys. Rev. Lett. and cited as Ref. 231 in this thesis.

ARPES measurements of Bi-2212 in the (π,0) region of **k**-space (FIG. 5.5) have been extensively discussed. For instance, Shen and Schrieffer [232] submitted that for underdoped samples, the spectra at (π,0) provide evidence of strong photohole coupling to a collective mode, with a spectral function peak near Q=(π,π) as observed in neutron scattering. Moreover, Norman and Ding [233] presented a model to argue that the presence of the sharp peak in the superconducting state reflects a rapid change in the imaginary component of the self energy, Im∑, at T_C. On other hand, Anderson and Ren [234] conjectured that changing the spectral weight in Bi-2212 from Γ to M may be the hallmark of spin charge separation. Next, the spectral line shape in the (π,0) region of **k**-space is regarding the superconducting and normal states, the temperature and polarization behavior, the polarization dependence of the four M points of the BZ, the doping dependence, and the dependence on excitation energy.

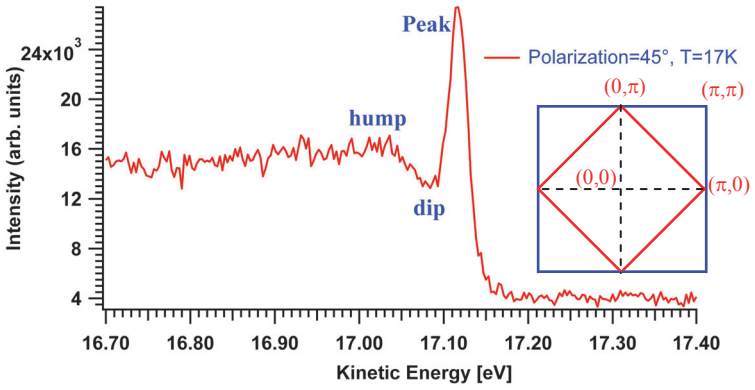

FIG. 5.5: ARPES spectrum of the (π,0) region of **k**-space at 17 K and at 45° polarization of the vector polarization $\hat{\varepsilon}$ with respect to the direction (0,0)-(π,0) for a Bi(Pb)-2212 single crystal at optimal doping (T_C=95 K). The inset show four directions in **k**-space.

The ARPES spectra of Bi-2212 are different in the normal state and the superconducting state. In the normal state the spectra are very broad. In the BZ direction (0,0)-(π,0) they exhibit much larger widths than in the nodal direction (0,0)-(π/2, π/2). This behavior corresponds to a large anisotropy in the scattering rate along the Fermi surface [232, 235], which has been considered in several theories which attempted to explain the anomalous transport and optical properties in HTC [236]. On the other hand, in the superconducting state the spectra near (0, π) exhibit the well known peak-dip-hump (PDH) line shape (FIG. 5.5) [237]. The polarization geometry is described later in this section. Campuzano et al. [238] have suggested that the energy position of the dip is related to the (π, π) resonance mode observed in neutron scattering experiments. Wen et al. [239] and Carlson et al. [240] have related the intensity of the peak to the condensate fraction of the superconducting state. The hump is related to the normal-state peak. Shen et al. [241] postulated that the different spectra above and below T_C in Bi-2212 compounds show a momentum transfer of spectral weight, which may be consistent with the presence of stripes.

In a first ARPES experiment the temperature dependence of Bi(Pb)-2212 was investigated at the (π, 0) point of the BZ for temperatures between 17 K and

100 K. The measurements were performed on almost optimally and optimally doped Bi(Pb)-2212 single crystals, respectively, with T_C=91 K and 95 K. The ARPES setup was equipped with a resonance lamp emitting photons of energy 21.2 eV (He Iα line) and a polarizer (SPECS, Berlin) yielding linearly polarized light of about 90%. In order to recoverthe intensity loss due to polarization the He radiation beam is focused onto the sample by a collecting capillary. The sample was cleaved in the UHV chamber with a base pressure of less than 5×10^{-10} mbar. During the measurements, the polarization was fixed at -45° (FIG. 5.7) and the temperature was measured by a diode mounted at the base of the cryostat in the vicinity of the sample. The overall spectral resolution was found to be 14 meV from a gold Fermi edge measurment. The angle resolution of the 100 mm Scienta energy detector was 0.1°. All measurements were performed with a pass energy of 2 eV.

Both samples exhibited a similar spectral near E_F structure between 17 K and 100 K. The spectra for the optimally doped sample are shown in FIG. 5.6, where there are different intensities in the sharp peak at the (π,0) or M point. The peak appears to decrease with increasing temperature, while all the peak positions are almost the same. Closer examination of the spectra at 100 K reveals that the intensity is strongly reduced but the peak still exists. Note that this is above T_C of 95 K of the crystal. Clearly, the peak does not vanish at T_C.

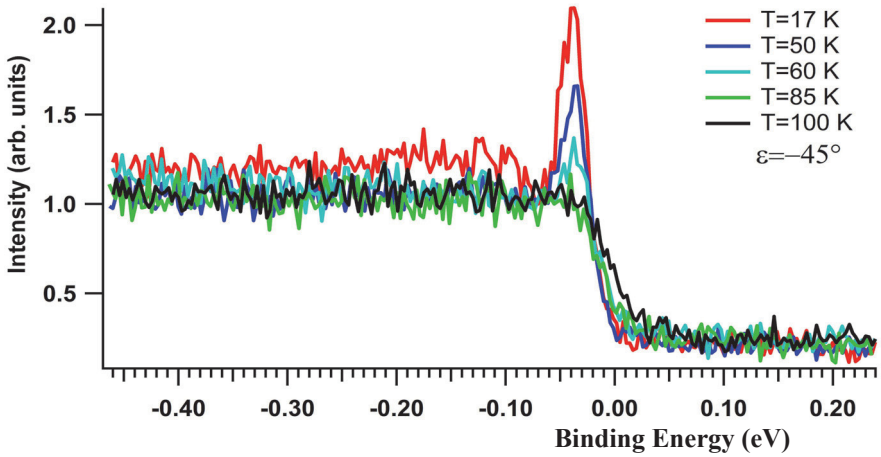

FIG. 5.6: Temperature dependence of the spectral line shape at the M point of the BZ of optimally doped Bi(Pb)-2212 for temperatures from 17 K to 100 K, at fixed -45° polarization geometry for a photon energy of 21.2 eV.

These results imply that the sharp peak at E_F has its origin in the pseudo gap which closes for optimally doped Bi(Pb)-2212 at a temperature slightly above T_C (~110 K) [242]. Similar behavior has also been reported by other groups for optimally doped Bi-2212 [243] and for (Bi,Pb)-2201 single crystals [244].

For the two-CuO_2 layer material Bi-2212 (has 2 CuO_2 layers per unit cell as discussed in section 2.1) at optimum doping, where T^* is only slightly above T_C, this difference is often overseen. For the one-CuO_2 layer material Bi-2201 at optimum doping T_C is much lower (~30 K) and T^* is also at about 110 K the sharp peak has clearly been observed for above T_C [244]. Thus, the sharp peak can be said to vanish at T^*. However, a sharp peak above T_C is not predicted by mean field theories. Moreover, Loesser et al. [245] have reported that a sharp peak also exists above T_C in overdoped Bi-cuprates.

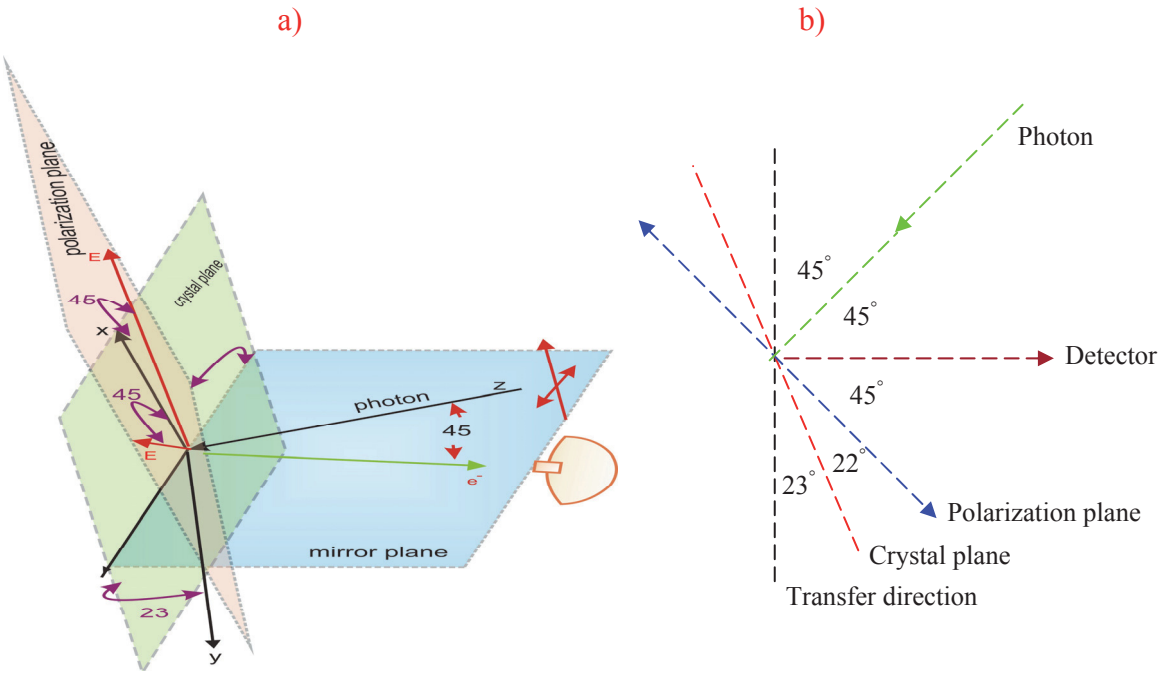

FIG. 5.7: a) Three polarization geometries: 0° polarization denotes the polarization vector normal to the mirror plane and +45° and -45° with respect to 0°. b) Sample planes, depicted from the top view for ease of viewing.

The ability to change the polarization direction of the linearly polarized He radiation in our ARPES setup enabled us to also investigate the polarization dependence very systematically, e.g. for spectra at the (π,0) or M point of the BZ. FIG. 5.7 shows a schematic of the sample and polarization plane, where Γ-M is along the CuO-bond direction. Moreover, the polarization geometries are also shown in FIG. 5.7a for ε=0° (polarization normal to the mirror plane), +45°, and -45°, respectively. The figure shows that the polarization vector lies in the ab plane only at zero polarization, whereas the polarization vector is outside the ab plane for the 45° and -45° polarizations. The data on the polarization dependence were collected at three different polarization geometries, i.e. 0°, 45°, and -45°, for the almost optimally and the optimally doped Bi(Pb)-2212 single crystals. The measurements were performed at 17 K.

Three spectra at polarization of the 0°, 45°, and -45° are shown in FIG. 5.8 for an almost optimally doped Bi(Pb)-2212 single crystal with T_C=91 K.

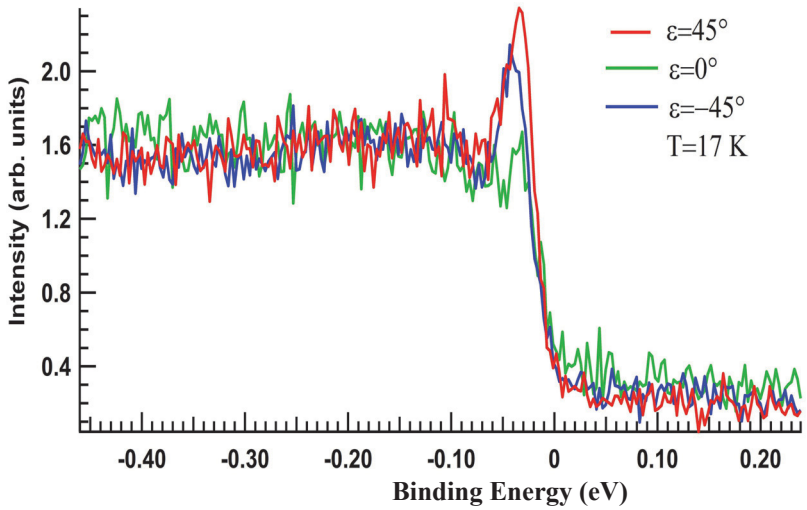

FIG. 5.8: Polarization dependence at the (π,0) or M point of the BZ of an almost optimally doped Bi(Pb)-2212 single crystals at 17 K. The red, green, and blue lines correspond to the 0°, 45°, and -45° polarization geometries, respectively.

The spectral line shape changes with the polarization: the peak intensity at 45° polarization is larger than at -45° polarization, while the lowest intensity is

observed at 0° polarization. From matrix element considerations, no peak is predicted for the 0° polarization and spectra of same intensity are predicted for the 45° and -45° polarizations. These unexpected results will be discussed later. FIG. 5.9 shows that the peak position of the sharp peak varies with the polarization geometry. The analysis was improved by fitting the sharp peak of each spectrum by a Gaussian function. The binding energy of the sharp peak lies in between -36 meV and -44 meV and the highest and lowest binding energies correspond to the 0° and -45° polarizations, respectively. The measurements were repeated at 50 K for the unexpected peak at 0° polarization.

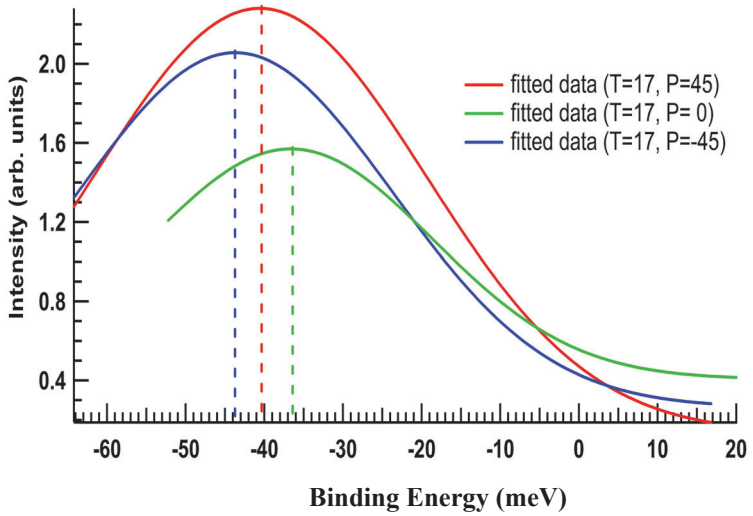

FIG. 5.9: Data from a fit of the sharp peak (similar to FIG. 5.8) by a Gaussian function. The energy position of the sharp peak varies with light polarization. All spectra were taken at 17 K.

FIG. 5.10 shows the spectra for the M point of the BZ for the 0° polarization at 17 K and 50 K. The spectra show that the unexpected peak still exists at 50 K. However, the peak intensity is strongly decreased at 50 K, similarly as in FIG. 5.6 for the -45° polarization.

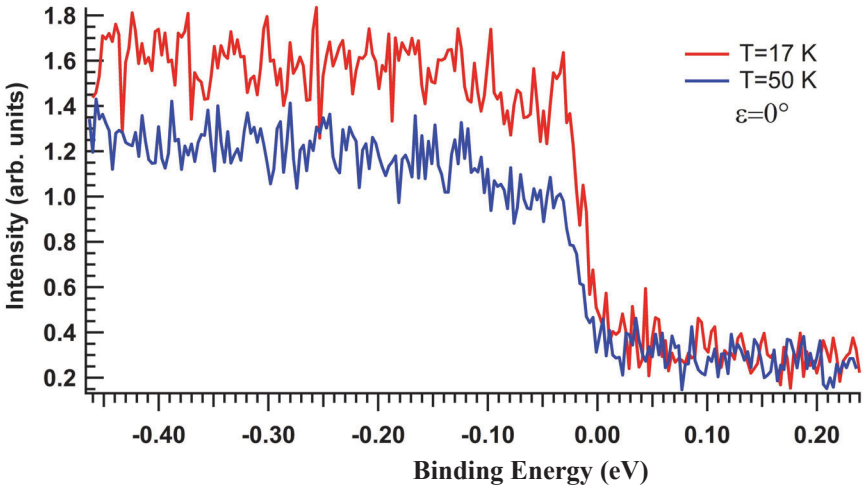

FIG. 5.10: Comparsion of two spectra at the 0° polarization for temperatures of 17 K and 50 K, shown by the red and blue lines, respectively.

To elucidate the polarization dependence, we should examine the matrix element, the simplest form of which was presented in section (5.3). Substituting the vector potential of equation (5-10) into equation (5-18) gives

$$M_{fi} = \frac{e}{mc} < f \mid A_0 e^{i\frac{\omega}{c}\hat{n}.\vec{x}} \hat{\varepsilon} \cdot \vec{P} \mid i > \qquad (5\text{-}19)$$

where the exponential term can be expanded as follows:

$$e^{i\frac{\omega}{c}\hat{n}\cdot\vec{x}} = 1 + i\frac{\omega}{c}\hat{n}\cdot\vec{x} + \frac{1}{2}(i\frac{\omega}{c}\hat{n}\cdot\vec{x})^2 + \ldots$$

The dipole approximation only accounts for the first term of the expansion. Equation (5-19) is then transformed to

$$M_{fi} = \frac{A_0 e}{mc}\hat{\varepsilon}\cdot < f \mid \vec{P} \mid i > \qquad (5\text{-}20)$$

In the simplest approximation the final and initial states correspond to a plane wave ($e^{i\vec{K}_f\cdot\vec{x}}$) and a $d_{x^2-y^2}$ orbital, respectively. After some algebra, equation (5-20) can be evaluated by

$$M_{fi} \sim \hat{\varepsilon}\cdot\vec{K}_f \int d^3x e^{-i\vec{K}_f.\vec{x}} \frac{x^2 - y^2}{r^2} \qquad (5\text{-}21)$$

The first term in equation (5-21), i.e. ($\hat{\varepsilon}\cdot\vec{K}_f$), changes with the polarization geometry. For instance at the 0° polarization, the angle between $\hat{\varepsilon}$ and $\vec{K}_f$ is 90°, which yields M_{fi}=0, as given in the previous section and table (5.1). The angle takes its highest value for $\hat{\varepsilon}\,||\,\vec{K}_f$. The $\hat{\varepsilon}\cdot\vec{K}_f$ for the 45° and -45° polarizations ($\vec{K}_f=\hat{j}K_f\cos 45^\circ+\hat{k}K_f\sin 45^\circ$ where $\hat{j}$ and $\hat{k}$ are unit vectors along the y-axis and z-axis respectively), leads to

$$\hat{\varepsilon}=45^\circ:\hat{\varepsilon}=\hat{\mathrm{i}}\cos 45^\circ+\hat{\mathrm{j}}\sin 45^\circ\rightarrow\hat{\varepsilon}\cdot\vec{\mathrm{K}}_{\mathrm{f}}\sim\sin 45^\circ\cos 45^\circ=0.5$$
$$\hat{\varepsilon}=-45^\circ:\hat{\varepsilon}=\hat{\mathrm{i}}\cos 45^\circ-\hat{\mathrm{j}}\sin 45^\circ\rightarrow\hat{\varepsilon}\cdot\vec{\mathrm{K}}_{\mathrm{f}}\sim-\sin 45^\circ\cos 45^\circ=-0.5$$

Thus, the same spectra should be observed for both polarizations. However, measurements of the polarization dependence revealed two types of unexpected behavior, as shown in FIG. 5.8: 1) different spectral behavior for the 45° and -45° polarizations and 2) observation of a peak at the 0° polarization, which was also observed at 50 K, as shown in FIG. 5.10. Both phenomena can not be explained using the dipole approximation discussed above. However, the peak can be explained from symmetry considerations by accounting for the other orbitals.

The polarization dependence of the spectral line shape (i.e. at 0°, 45°, and -45° polarizations) at the four M points of the BZ were carried out on optimally doped Bi(Pb)-2212 single crystals with T_C=95 K. All measurements were performed at a temperature of 17 K by a helium lamp light source, while the resolution of each spectrum was now 14 meV, as derived from gold spectra. The spectra for the 0°, 45°, and -45° polarizations are shown in FIG. 5.11 by green, red, and blue lines, respectively, for ease of viewing. The spectral line shape at the first M point assigned M_1 is depicted in FIG. 5.11a) for the three polarization geometries. The positions of the M points of the BZ are shown in the inset of FIG. 5.11a).

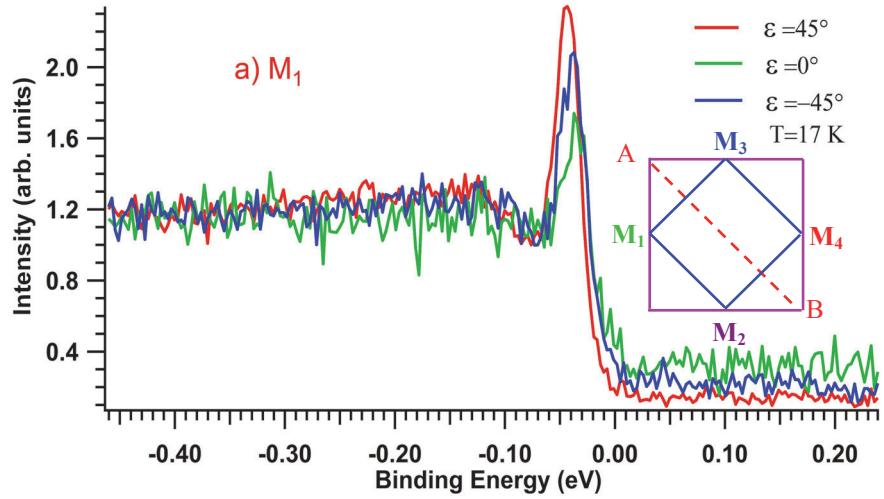
a) M1
ε =45°
ε =0°
ε =–45°
T=17 K
A
M3
M1
M4
B
M2
Intensity (arb. units)
2.0
1.6
1.2
0.8
0.4
-0.40
-0.30
-0.20
-0.10
0.00
0.10
0.20
Binding Energy (eV)

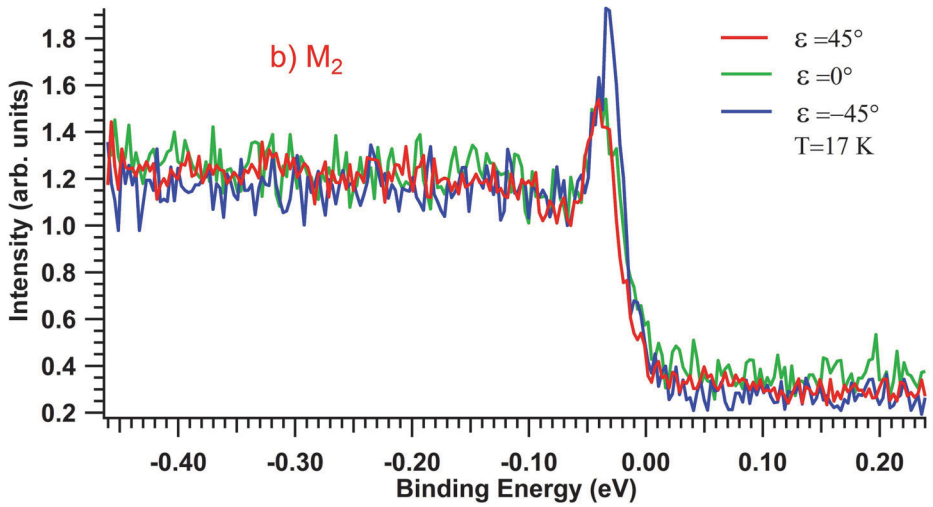
b) M2
ε =45°
ε =0°
ε =–45°
T=17 K
Intensity (arb. units)
1.8
1.6
1.4
1.2
1.0
0.8
0.6
0.4
0.2
-0.40
-0.30
-0.20
-0.10
0.00
0.10
0.20
Binding Energy (eV)

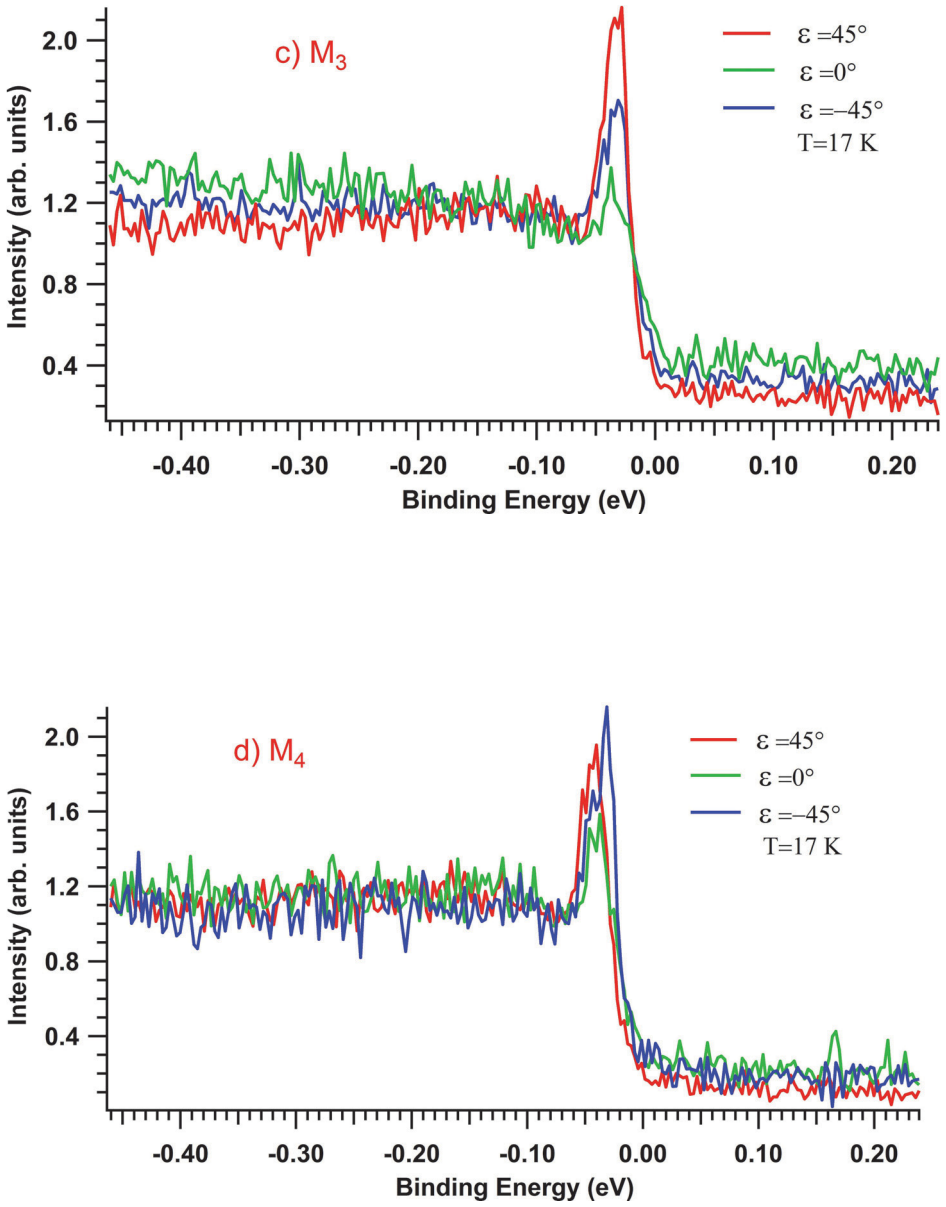

FIG. 5.11: Polarization dependencies of the spectral line shape at the different M points of the BZ assigned by a) M_1, b) M_2, c) M_3, and d) M_4. The position of each M point in the Brillouin zone is depicted in the inset of a). The dashed line between points A and B will be discussed in the text.

For M_1 the sharp peak is clearly observed for all three polarization geometries. Moreover, the intensity at the 45° polarization is greater than in the other two directions. The lowest intensity corresponds to the 0° polarization. As previously discussed, no peak should be observed at the 0° polarization and the

45° and -45° polarizations should exhibit similar spectra. These two phenomena have been unexpectedly found in this study, as discussed above.

Very different behavior is observed for the polarization measured at the M_2 point (FIG. 5.11b). A sharp peak was also observed for the three polarizations, but in this case the intensity corresponding to the -45° polarization is greater than in the other two directions. Thus, the symmetry between the M_1 and M_2 points was broken and the two points presented opposite polarization effects at the 45° and -45° polarizations.

The sharp peak was also observed at M_3 and M_4 for the three polarizations, which is shown in c and d of FIG. 5.11, respectively. M_3 and M_4 exhibit opposite polarization effects for the 45° and -45° polarizations, showing that symmetry is also broken for M_3 and M_4. Finally, we conclude from the measurements presented in FIG. 5.11 that the points M_1, M_3 and M_2, M_4 exhibit similar polarization behavior. The first result in FIG. 5.11 indicates rotational symmetry-breaking, which has been also previously found for HTC. For instance, Fauque et al. [246] used polarized neutron scattering to find rotational symmetry-breaking below T^*. This symmetry-breaking has also been observed using the Nernst effect [247]. Recently, rotational symmetry-breaking was also confirmed by Poccia et al. [248]. Thus, the AB line shown in the inset of FIG. 5.11a at 45° from the Cu-O-Cu direction, can be used as a mirror plane in the BZ. This is another unexpected result that has been found in this study. This result also can not be understood within the dipole approximation for two-dimensional materials, which predicts that the four M-points should exhibit the same spectra. The results in FIG. 5.11 indicate a one-dimensional direction for the Bi(Pb)-2212 single crystals that could be interpreted as e.g. stripes. Thus, the formation of magnetic stripes leads to a one-dimensionality of the charge, causing the four points to exhibit two-by-two similar spectra. This view is supported by Shen et al. [241], as mentioned above. Additionally, Saini et al. [249] found a clear difference between the Γ-M=$(0,\pi)$ and Γ-M=$(\pi,0)$ directions when the photon polarization was along the Γ-M=$(0, \pi)$ and Γ-M=$(\pi, 0)$ directions. The authors found evidence for charge stripes along the

diagonal direction in Bi-2212 single crystals and for small k'_F (~0.2π) along the (π, 0) direction of the Brillouin zone [249, 250]. Saini et al. [249] described the charge fluctuations in terms of the nesting wave vector q_c=2k'_F (~0.4π). Note that one-dimensional, incommensurate, low-frequency spin fluctuations with wave vector q_s~(0.2π, 0) have also been observed in cuprates using inelastic neutron scattering [251-253]. These fluctuation are expected to be associated with charge fluctuations of wave vector 2q_s, which is similar to the nesting vector q_c, as discussed by Saini et al. [249]. Finally, the lattice modulation in the copper oxide plane for Bi-2212 has been shown to be at 45° from the Cu-O-Cu direction (similar to the AB line in the inset of FIG. 5.11a), with a wave vector in the (~0.2π,~0.2π) direction forming a superlattice of stripes [254-257].

Progressing from undoped and underdoped samples to overdoped samples, the broad spectrum in the (π, 0) region of **k**-space continuously evolved into a sharp peak [258]. However, the spectra along the (0, 0)–(π, π) direction revealed that a sharp peak structure is independent of the amount of doping in the Bi-2212 samples. Moreover, a similar dispersion relationship, in the form of a $d_{x^2-y^2}$ gap function, has been observed between undoped and underdoped samples at the maximum peak positions from (π/2, π/2) to (π, 0) [259]. These results reveal that there is a close relationship between antiferromagnetism and superconductivity.

Kordyuk et al. [260] have shown that the spectral line shape at M changes with the excitation energy (18-65 eV) in the superconducting state of an overdoped Bi(Pb)-2212 sample (FIG. 5.12). FIG. 5.12 shows that the peak, dip, and hump are absent at the following photon energies: 39 eV, 25 or 42 eV, and 50 eV. Attention should be paid to the fact that in the (π,0) region of **k**-space PDH in the superconducting state, both the peak and dip originate from only a single spectral function in the many body picture [260, 261]. Thus, the imaginary part of the self-energy changes drastically on entering the superconducting state.

Thus, all the spectra in FIG. 5.12 must be same as only external parameters have been changed, which the spectral functions are insensitive to. Therefore, the results of Kordyuk et al. [260] strongly oppose self energy effects for a single spectral function. These results are supported by Chuang [262], who noted that the spectral weight depends strongly on the incident energy hν. The matrix element in equation 5-18 could also depend on the energy, as discussed in Ref. [32].

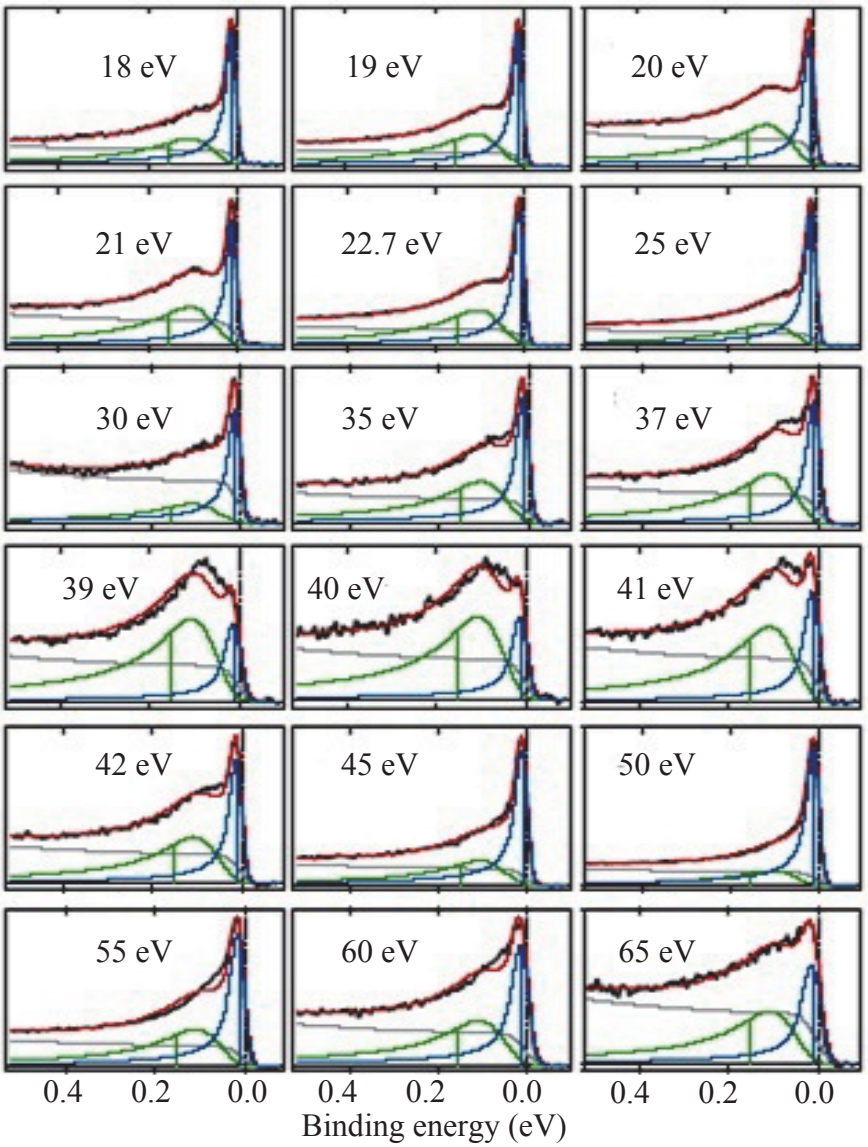

FIG. 5.12: Photoemission spectra series of the emissions at the Fermi energy of an overdoped (T_C=69 K) Bi-2212 sample in the superconducting state for different excitation energies, from Ref. 260.

Chapter 6

Density Functional theory

Over the last decade, the calculation of material properties by Density Functional Theory (DFT) has become a very active area of research in condensed matter physics: approximately 10,000 publications appeared in 2010 alone (www.isiknowledge.com). In this chapter, density functional theory is reviewed as a powerful technique for the investigation of the electronic structure of solids. The basic tenets of DFT are briefly discussed in the introduction below. The exchange and correlation energy within DFT is reviewed. Some methods such as the APW, LAPW, and APW+lo methods are explained. Additionally, the underestimation of the band gap within DFT is discussed. Finally, the electronic structure of Bi(Pb)-2212 using DFT is discussed.

6.1 Introduction

DFT is an extremely successful approach for describing the ground state properties of insulators, semiconductors, and metals, where an interacting system of electrons is described in terms of the charge density rather than in terms of the many body wave function. A short review of DFT is presented here. The reader may refer to Ref. 263-265 for further details on DFT.

The Hamiltonian for a solid with nuclei, each with mass M_i, and electrons, each with mass m_e, which are located at R_i and r_i, respectively, can be written as [263, 264]

$$\widehat{H} = -\frac{\hbar^2}{2}\sum_i \frac{\nabla^2_{\vec{R}_i}}{M_i} - \frac{\hbar^2}{2}\sum_i \frac{\nabla^2_{\vec{r}_i}}{m_e} - \frac{e^2}{4\pi\varepsilon_0}\sum_{i,j}\frac{Z_i}{\left|\vec{R}_i - \vec{r}_j\right|} + \frac{e^2}{8\pi\varepsilon_0}\sum_{i\neq j}\frac{1}{\left|\vec{r}_i - \vec{r}_j\right|} + \frac{1}{8\pi\varepsilon_0}\sum_{i\neq j}\frac{Z_i Z_j}{\left|\vec{R}_i - \vec{R}_j\right|} \quad (6\text{-}1)$$

where the first and second terms are the kinetic energy operators of the nuclei and the electrons, respectively. The next three terms represent the Coulomb interactions between electrons and nuclei, electrons and other electrons, and nuclei and other nuclei, respectively. It is difficult to find the eigenvalues and eigenvectors of the Hamiltonian in equation (6-1). To solve this problem, the velocities and masses of the nuclei are taken to be lower and higher than for the electrons, respectively (as assumed by Born-Oppenheimer). Thus, the first and last terms in equation (6-1) are zero and constant, respectively, reducing equation (6-1) to

$$H = T + V_{e\text{-}e} + V_{ext} \quad (6\text{-}2)$$

where the first term denotes the kinetic energy of the electrons and the next two terms represent the potential energy of the electron-electron interactions and the interaction of the electrons with the external field, respectively. In fact, the Coulomb interaction between the atomic nuclei and the electron cloud in equation (6-1) is used as the last term in equation (6-2). The ground state energy functional can be found from two theorems by Hohenberg and Kohn [266].

First theorem: There is a one-to-one correspondence between the ground-state density ρ(r) of a many-electron system and the external potential V_{ext} ($\rho(\vec{r}) \leftrightarrow V_{ext}$). The immediate consequence is that the ground state expectation value of any observable $\hat{A}$ is a unique functional of the exact ground state electron density [264]:

$$< \psi \mid \hat{A} \mid \psi >= A[\rho] \qquad (6\text{-}3)$$

Second theorem: When the Hamiltonian $\hat{H}$ is given by $\hat{A}$, the ground state total energy functional is of the form [264]

$$\begin{aligned} E_{V_{ext}}[\rho] &=< \psi \mid \hat{T} + \hat{V} + \hat{V}_{ext} \mid \psi >=< \psi \mid \hat{T} + \hat{V} \mid \psi > + < \psi \mid \hat{V}_{ext} \mid \psi > \\ E_{V_{ext}}[\rho] &= F_{HK}[\rho] + \int \rho(\vec{r}) V_{ext}(\vec{r}) d\vec{r} \end{aligned} \qquad (6\text{-}4)$$

where the first term $F_{HK}[\rho]$ is called the Hohenberg-Kohn density functional, which is universal for any many-electron system. Equation (6-4) has a minimum at the ground-state density corresponding to V_{ext} [264]. Recognizing that the correlation energy is part of the exact total energy but absent in the Hartree-Fock solution, $F_{HK}[\rho]$ can be rewritten as [264]:

$$F_{HK} = T_0 + V_H + V_{xc} \qquad (6\text{-}5)$$

where T_0, V_H, and V_{xc} are the kinetic energy of a non-interacting electron gas, the Hartree contribution, and the exchange-correlation energy functional, respectively. Therefore, for a known exchange-correlation energy, the energy functional can be written as [264]

$$E_{V_{ext}}[\rho] = T_0[\rho] + V_H[\rho] + V_{xc}[\rho] + V_{ext}[\rho] \qquad (6\text{-}6)$$

The corresponding Hamiltonian of equation (6-5) is called the Kohn-Sham Hamiltonian, which is given by [264]

$$\hat{H}_{KS} = \hat{T}_0 + \hat{V}_H + \hat{V}_{xc} + \hat{V}_{ext} = -\frac{\hbar^2}{2m_e}\vec{\nabla}_i^2 + \frac{e^2}{4\pi\varepsilon_0}\int \frac{\rho(\vec{r}')}{|\vec{r} - \vec{r}'|} d\vec{r}' + V_{xc} + V_{ext} \qquad (6\text{-}7)$$

where the exchange-correlation potential in equation (6-6) is calculated from the following functional derivative

$$\hat{V}_{xc} = \frac{\delta V_{xc}}{\delta \rho} \qquad (6\text{-}8)$$

Finally, the exact ground state density of an N-electron system is given by

$$\rho(\vec{r}) = \sum_{i=1}^{N} \varphi_i(\vec{r}) * \varphi_i(\vec{r}) \qquad (6\text{-}9)$$

where the $\varphi_i(\vec{r})$ are the single-particle wave-functions of the N-lowest time-independent solution of the Kohn-Sham equation, i.e.,

$$\hat{H}_{KS}\varphi_i = \varepsilon_i\varphi_i \qquad (6\text{-}10)$$

The unknown exchange-correlation energy in equation (6-7) is discussed in the next section.

6.2 Exchange and correlation energy

In the previous section, equation (6-9) was obtained using a single approximation, i.e. the Born-Oppenheimer approximation, in which the exchange-correlation functional was unknown. Therefore, a reasonable approximation must be used to find the exchange-correlation functional.

For this purpose, functionals such as the local density approximation (LDA) [266] and the generalized gradient approximation (GGA) are used. The exchange-correlation energy within the LDA has the following form:

$$E_{xc}^{LDA}[\rho] = \int \rho(\vec{r})\varepsilon_{xc}(\rho(\vec{r}))d\vec{r} \qquad (6\text{-}11)$$

where ε_{xc} and $\rho(\vec{r})$ are the exchange-correlation energy per particle of a homogeneous electron gas and the electron density, respectively. The exchange-correlation energy can be calculated as a function of the electron density ($\varepsilon_{xc} = -\frac{3}{4}(\frac{3}{\pi})^{1/3}\rho^{4/3}$). The LDA functional appears to work well for systems with low density variations because the LDA was derived for a homogeneous electron gas. The LDA remains one of the most successful approximations for some classes of solids, e.g. the 5d transition metals [267]. On the other hand, within the GGA formalism, the gradient of the electron density is used to better describe the electronic structure of an atom. There are several versions of the GGA such as Perdew-Burke-Ernzerhof (PBE) [268], Wu-Cohen 2006 (WC) [269], and Perdew et al. 2008 (PBEsol) [270]. A review of the LDA and the GGA can be found in Refs. 267 and 271. In particular, Ref.

272 discusses some new GGA approximations. The exchange-correlation energy in the GGA is given by [267, 271]

$$E_{xc}[\rho] = \int \varepsilon_{xc}^{GGA}(\rho(r), \nabla\rho(r)) d^3r = \int \varepsilon_{xc}^{LDA}(r_s(r)) F_{xc}(r_s(r), s(r)) d^3r \qquad (6\text{-}12)$$

where F_{xc}, r_s, and s are the enhancement factor, the Wigner-Seitz radius, and the reduced density gradient, respectively, which can be written in the following form:

$$F_{xc}(r_s, s) = F_x(s) + F_c(r_s, s), \quad r_s = (\frac{3}{4\pi\rho})^{1/3}, \quad s = \frac{\nabla\rho}{\left[2(3\pi^2)^{1/3}\rho^{4/3}\right]}, \qquad (6\text{-}13)$$

where the enhancement factor from two versions of the GGA (i.e. PBE and WC) is

$$F_x^{PBE}(s) = 1 + \kappa - \frac{\kappa}{1 + \frac{\mu}{\kappa}s^2}, \qquad F_x^{WC}(s) = 1 + \kappa - \frac{\kappa}{1 + \frac{x(s)}{\kappa}}, \qquad (6\text{-}14)$$

where $\kappa = 0.804$, $\mu = 0.21951$, and

$$x(s) = \frac{10}{81}s^2 + (\mu - \frac{10}{81})s^2 e^{-s^2} + Ln(1 + cs^4) \text{ (c=0.0079325)} \qquad (6\text{-}15)$$

In the PBEsol GGA formalism, which is based on PBE, μ equals $\frac{10}{81}$ [267].

PBEsol is an improvement over PBE for several types of solids [273, 274], as well as for 4d and 5d transition metals [275, 276]. Wu and Cohen [269] have shown that the WC functional is a significant improvement over the LDA and PBE in terms of the geometrical parameters and the bulk modulus of solids. It has been argued that both the LDA and GGA approximations usually underestimate the band gaps [277]. It will be discussed in section 6.4.1 when the band gap in a ternary ZrS_xSe_{2-x} semiconductor for x = 0, 1, and 2 can be estimated by DFT in good agreement with experimental data [277]. Aditionally, the effect of lithium intercalation on the electronic structure of the ternary compound semiconductors $ZrSe_{2-x}S_x$ is discussed in section 6.4.2. Finally, in section 6.5, I shall compute the electronic structure of Bi-2212 using the GGA functional and GGA+U, where U is calculated by an ab initio method. However, we shall see that the band gap cannot be found,

necessitating an exact description of the electronic structure of the Bi-2212 system.

6.3. APW, LAPW, and APW+lo methods

In the augmented plane wave (APW) method, electron states are described in different spatial regions close and far away from the nuclei [278-281]. The electrons are modeled by atomic-like wave functions and by plane waves, respectively, in these two regions the behavior of the electrons is similar to that of a free atom and a free electron, respectively. The regions are modeled by building a sphere with radius R_α around each atom, such that the sphere volume is smaller than the lattice cell and the spheres centered at different sites do not overlap. These spheres are called muffin-tin (MT) spheres. Thus, the space is divided into regions inside (S_α) and outside (I) the MT spheres, called the MT and interstitial regions, respectively, as shown in FIG. 6.1.

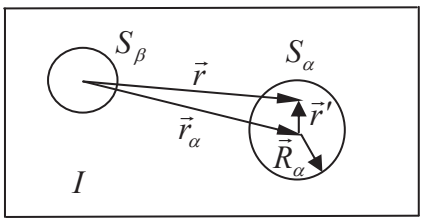

FIG. 6.1: Two different spatial regions (MT and interstitial regions (I)) that are modeled by the APW method for electron states [264].

Assuming that the potential inside the spheres is spherically symmetric, the corresponding wavefunctions, for a given energy inside and outside the MT spheres, can be written as [280, 281]

$$\phi(\vec{r}) = \begin{cases} \Omega^{-1/2} \sum_G c_G e^{i(\vec{G}+\vec{k})\cdot\vec{r}} & r \in I \\ \sum_{lm} A_{lm}^{\alpha,\vec{k}+\vec{G}} u_l^\alpha(r,E) Y_m^l(\hat{r}) & r \in S_\alpha \end{cases} \qquad (6\text{-}16)$$

where Ω and $c_G / A_{lm}^{\alpha,\vec{k}+\vec{G}}$ are the cell volume and the expansion coefficient, respectively. The Y_m^l are the spherical harmonics and the u_l^α are the solutions to the corresponding Schrödinger equation, i.e.,

$$[-\frac{d^2}{dr^2}+\frac{l(l+1)}{r^2}+V(r)-E_l]ru_l^\alpha(r,E)=0 \qquad (6\text{-}17)$$

where $V(r)$ is the spherical component of the potential in the sphere. The basis wavefunctions in equation (6-16) can be chosen to have the form of plane waves because the MT potential is constant outside the spheres. $A_{lm}^{\alpha,\vec{k}+\vec{G}}$ and E are two undetermined parameters in equation (6-16). By expanding the plane waves in the spherical harmonics using the spherical Bessel function j_l, the solutions at the sphere boundary can be found to determine the coefficients $A_{lm}^{\alpha,\vec{k}+\vec{G}}$ [281]:

$$A_{lm}^{\alpha,\vec{k}+\vec{G}}=\frac{4\pi i^l}{\Omega^{1/2}u_l(R)}\sum_G c_G j_l(|\vec{k}+\vec{G}|R)Y_m^{l\,*}(\vec{k}+\vec{G}) \qquad (6\text{-}18)$$

Thus, the $A_{lm}^{\alpha,\vec{k}+\vec{G}}$ are determined by the plane wave coefficients, the energy parameters E_l, and c_G. The $\phi(\vec{r})$ function inside the spheres in equation (6-16) is called the APW. An infinite number of $A_{lm}^{\alpha,\vec{k}+\vec{G}}$ exist from equation (6-18), which needs to be truncated for computational purposes at some value l_{max}. Note that the $l_{\max}Y_m^{l_{\max}}$ have at most $2l_{max}$ nodes along the great circle of the α-sphere for $\theta=0\to 2\pi$ at any fixed φ angle equal to $\frac{2l_{\max}}{2\pi R_\alpha}=\frac{l_{\max}}{\pi R_\alpha}$ nodes per unit length. When the plane wave has at least a similar number of nodes per unit length which leads to

$$R_\alpha G_{\max}=l_{\max} \qquad (6\text{-}19)$$

because the shortest period of the plane wave, $\lambda=\frac{2\pi}{G_{\max}}$, has $2/(2\pi/G_{\max})$ nodes per unit length. Equation (6-19) enables us to determine an appropriate l_{max} for a given G_{max}. The APW basis functions with boundary conditions have thus been determined. The E parameter has not yet been determined: thus, we

set E in the $u_l^\alpha(r,E)$ of each APW equal to the eigenvalue (or band energy) $\varepsilon_{\vec{k}}^n$ of the eigenstate of the crystal wavefunction $\psi_{\vec{k}}^n(\vec{r})$, where $\varepsilon_{\vec{k}}^n$ the very quantity we seek. The problem is solved iteratively, using an initial guess for $\varepsilon_{\vec{k}}^n$ that allows the APWs to be determined to construct the Hamiltonian matrix and the overlap matrix (the APWs are not orthogonal). Consequently, the following secular equation [281] is produced

$$(\hat{H} - E\hat{S}) \cdot \vec{a} = 0 \qquad (6\text{-}20)$$

The root of equation (6-20) is the initial guess for $\varepsilon_{\vec{k}}^n$. Typically, E must be guessed again. This procedure is repeated until a root is found, as shown in FIG. 6.2. The d-bands have been observed to require a large number of APWs compared to the s- and p-bands [281].

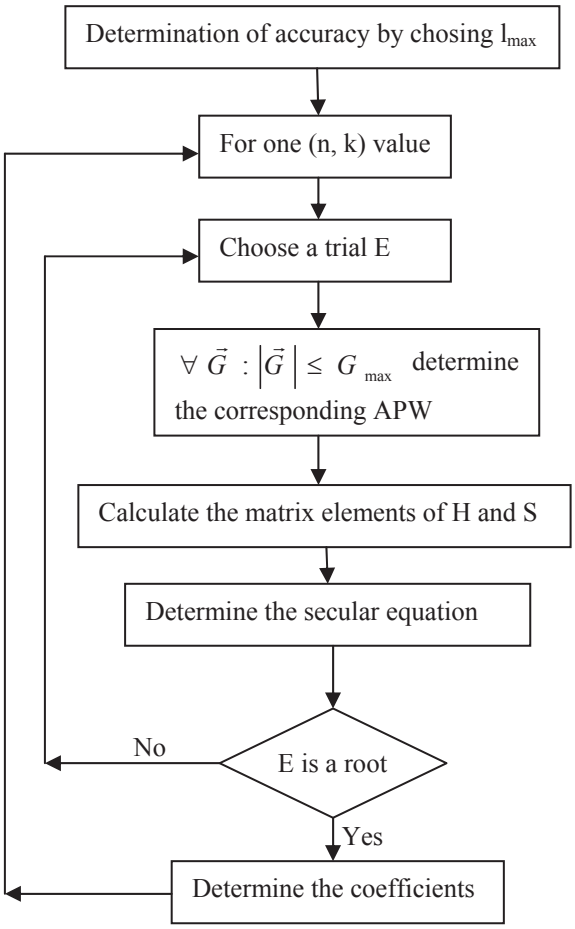

FIG. 6.2: Schematic of the APW method [264].

Within the APW method, as discussed above, the $u_l^{\alpha}(r,E)$ must be constructed at an unknown eigenenergy $E=\varepsilon_{\vec{k}}^{n}$. To solve this problem, the $u_l^{\alpha}(r,E)$ are calculated at a certain energy E_l, similarly to the APW method, where the energy derivative $u_l^{\alpha}(r,E)Y_m^l(\hat{r})$ satisfies following equation [280, 281]

$$[-\frac{d^2}{dr^2}+\frac{l(l+1)}{r^2}+V(r)-E_l]r\dot{u}_l^{\alpha}(r,E)=ru_l^{\alpha}(r,E) \qquad (6\text{-}21)$$

and $\dot{u}_l^{\alpha}(r',E)=\left.\frac{\partial u_l^{\alpha}(r,E)}{\partial E}\right|_{E=E_l}$. These functions are matched to the values and derivatives of the plane waves at the sphere boundaries. This method for augmented plane waves is called the linearized augmented plane wave (LAPW). The wavefunction in terms of the LAPW method is written as follows [280, 281]:

$$\phi(\vec{r})=\begin{cases}\Omega^{-1/2}\sum_G c_G e^{i(\vec{G}+\vec{k})\cdot\vec{r}} & r\in I\\ \sum_{lm}[A_{lm}^{\alpha,\vec{k}+\vec{G}}u_l(r,E)Y_m^l(\hat{r})+\quad B_{lm}^{\alpha,\vec{k}+\vec{G}}\dot{u}_l(r,E)Y_m^l(\hat{r})] & r\in S_{\alpha}\end{cases} \qquad (6\text{-}22)$$

where $A_{lm}^{\alpha,\vec{k}+\vec{G}}$ and $B_{lm}^{\alpha,\vec{k}+\vec{G}}$ are two coefficients that are determined from the boundary condition. After some algebra, $A_{lm}^{\alpha,\vec{k}+\vec{G}}$ and $B_{lm}^{\alpha,\vec{k}+\vec{G}}$ are obtained as [280, 281]

$$\begin{aligned}A_{lm}^{\alpha,\vec{k}+\vec{G}}&=4\pi R^2\Omega^{-1/2}i^l{Y_m^l}^{*}a_l;\quad a_l=[j_l'(n)_l\dot{u}_l^{\alpha}-j_l(n)\dot{u}_l'^{\alpha}]\\ B_{lm}^{\alpha,\vec{k}+\vec{G}}&=4\pi R^2\Omega^{-1/2}i^l{Y_m^l}^{*}b_l;\quad b_l=[j_l(n)_l u_l'^{\alpha}-j_l'(n)u_l^{\alpha}]\end{aligned} \qquad (6\text{-}23)$$

The LAPWs (similarly as in the APW method) are just plane waves in the interstitial region, whereas the LAPWs inside the MT spheres have more variational freedom than the APWs. This can be explained by Taylor expanding $u_l(r,E)$ as follows:

$$u_l^{\alpha}(r,E)=u_l^{\alpha}(r,E_l)+(E-E_l)\dot{u}_l^{\alpha}(r,E)+... \qquad (6\text{-}24)$$

This means that if E_l differs slightly from the band energy, a linear combination can reproduce the APW function constructed at the band energy. The APW method produces exactly the correct wavefunction for a converged plane wave set and a muffin-tin potential, while the LAPW method produces errors of order $(E-E_l)^2$ and $(E-E_l)^4$ for the wave function and the band energy, respectively. The accuracy of the plane wave method is determined by G_{max}. A better parameter for controlling the accuracy is the product $R_{\min}^{\alpha} K_{\max}$ in the APW and LAPW methods. This parameter also has been used in electronic structure calculations for Bi(Pb)-2212 and $CaCuO_2$.
Some advantages of the LAPW method include that E_l is a fixed parameter and that the basis set is energy-independent.

In the APW method discussed above, the difficulty lies in the energy dependence of the APW basis set. To solve this problem, Sjostedt et al. [282] developed the APW+lo method, in which the basis set is energy-independent and has the same size as the APW method. Further details on the APW+lo method can be found in Ref. 282.

6.4 DFT and the underestimation of the band gap

It has been argued that both the LDA and GGA approximations usually underestimate the band gaps [277] for semiconductors and insulators. Additionally, the failure of the LDA and GGA functionals to find bands gap in strongly correlated materials, such as high-T_C cuprates, transition metal oxides, 3d itinerant magnets, and heavy-fermion compounds [283] is well known. Typically, in the DFT calculation the underestimation of the band gap when compared with experimental data is about 30%–100%. DFT would correctly describe the electronic structure of solids if the exchange-correlation functional that is used was exact. The exchange-correlation energy was discussed in section 6.2. Tran and Blaha have solved the band gap problem for some classes of materials by introducing a new potential known as the MBJ potential [284], which has the following form [284]:

$$v_{x,\sigma}^{MBJ}(r) = cv_{x,\sigma}^{BJ}(r) + (3c-2)\frac{1}{\pi}\left(\frac{10t_\sigma(r)}{12\rho_\sigma(r)}\right)^{1/2} \quad (6\text{-}25)$$

where ρ_σ is the electron density, t_σ is the kinetic energy, and $v_{x,\sigma}^{BJ}$ is the Becke-Roussel potential [285] that is given by

$$v_{x,\sigma}^{BJ}(r) = -\frac{1}{b_\sigma(r)}\left(1 - \frac{1}{e^{x_\sigma(r)}} - \frac{x_\sigma(r)}{2e^{x_\sigma(r)}}\right) \quad (6\text{-}26)$$

Here x is determined from a nonlinear equation involving ρ, $\nabla\rho$, and $\nabla^2\rho$. And

$$c = \alpha + \beta\left(\frac{1}{V}\int_{cell}\frac{|\nabla\rho(r')|}{\rho(r')}d^3r'\right)^{1/2} \quad (6\text{-}27)$$

where V is the unit volume cell and α and β are two free parameters.

However, hybrid functionals also improve the band gap but they are too much expensive than the MBJ potential. In this class of functionals (i.e. hybrid functionals) a fraction of semilocal exchange is replaced by Hartree Fock exact exchange (i.e. $E_{xc}^{hybrid} = E_{xc}^{SL} + \alpha(E_x^{HF} + E_x^{SL})$). For instance, in the well known B3LYP [286, 287] functional which has been widely used the fraction is α=0.2. In the next two sections the capability of MBJ potential to improve the band gap is revealed in ZrS_xSe_{2-x} and $LiZrSe_{2-x}S_x$ compounds. We will see in section 6.4.1 that the band gap in a ternary ZrS_xSe_{2-x} semiconductor can be estimated more accurately by the MBJ potential than by the LDA and GGA functionals. Furthermore, the effect of lithium intercalation to the band gap size of $ZrSe_{2-x}S_x$ Zr by the MBJ potential is discussed in section 6.4.2.

6.4.1 Improvement of the band gap determination of ZrS_xSe_{2-x} by MBJ

The results of this section was published in Phys. Rev. B **84**, 125205 (2011) and J. of electron spectroscopy and related phenomena which is cited as Ref. 277 in this thesis.

The layered 1T-metal dichalcogenides have been found to possess interesting anisotropic optical, mechanical, and transport properties. Observation of charge density waves, superconductivity, sometimes their coexistence in some members, and many technology applications (such as solar cells and fuel cells), cause them to be a unique subject for intensive experimental and theoretical

research [288]. Zirconium dichalcogenide compounds attracted much interest due to their suitability for a number of applications. For instance, recently electrical transport properties and prototype optoelectronic devices based on individual ZrS_2 nanobelts have been discussed in [289].

The general formula of the dichalcogenides is MX_2 (M the metal and X the chalcogenide) where in the ZrS_xSe_{2-x} compound M represents Zr and X is Se or S, i.e. the zirconium planes are sandwiched between two sulphur/selenium layers. Therewith the hexagonal crystal structure of ZrS_xSe_{2-x} compound consists of X-M-X atomic trilayer units, which are joined by strong covalent bonds inside the layers, whilst relatively weak Van der Waals forces hold the sheets together. ZrS_2 and $ZrSe_2$ have the P-3m1 space group while ZrSeS has the P3m1 space group. The calculations have been performed by the Wien2k code (MBJ) [290] and the computational method is as following.

First, experimental lattice parameters were used [291]. Subsequently, the k-points, G_{max} and $R_{MT}K_{max}$ (where R_{MT} represents the smallest muffin-tin radius and K_{max} is the maximum size of reciprocal lattice vectors) are optimised by starting from $G_{max}=12\ (au)^{-1}$, $R_{MT}K_{max}=6$ and k-points=100 while the valence wave functions inside the spheres are expanded up to $L_{max}=10$. A self-consistent iteration process was repeated until the charge convergence of 0.000001 e was reached. The convergence is obtained using the $G_{max}=14\ (au)^{-1}$, 500 k-points mesh in the irreducible Brillouin zone, and $R_{MT}K_{max}=8.5$. Second, using optimized values of $R_{MT}K_{max}$, G_{max}, and k-points and experimental lattice parameters the volume was optimised by minimizing the total energy of the crystal to the volume in the PBEsol functional and then the theoretical lattice constants were extracted (Table 6.1). Finally, the density of states (DOS) and band structure can be calculated by considering the exchange-correlation energy.

Tran and Blaha [284] proposed a new potential that combines the modified Becke-Johnson potential [285] and LDA which gives a similar precision as obtainable with the more expensive hybrid functionals and GW methods while the MBJ potential is computationally as cheap as LDA or GGA.

Table 6.1: Calculated optimized lattice parameters within the PBEsol functional for $ZrSe_2$, ZrS_2, and ZrSeS with hexagonal crystal structure. The experimental lattice parameters are given in parentheses from Ref. [291].

Compound	a, b (Å)	c (Å)	Space group
$ZrSe_2$	3.789 (3.758)	6.165 (6.114)	P-3m1
ZrS_2	3.654 (3.660)	5.795 (5.804)	P-3m1
ZrSeS	3.713 (3.709)	6.010 (6.004)	P3m1

Therewith it can obtain accurate band gaps. For testing the MBJ potential, the electronic structure of the ZrS_xSe_{2-x} semiconductor for x = 0 and 2 as well as for the ternary compound with x=1 has been calculated by six different exchange-correlation energy approximations which are: LDA, Perdew-Burke-Ernzerhof (PBE) [268], Wu-Cohen 2006 (WC) [269], Perdew et al. 2008 (PBEsol) [270], Engel-Vosko (EV) approximation [292, 293], and MBJ.

After analysing the results we have classified them in two groups; the first group contains PBE 96, LDA, WC, and PBEsol and gives similar electronic structures for each compound (i.e. $ZrSe_2$, ZrS_2, and ZrSeS). For each compound the band gap that is calculated by LDA is distinctly smaller than that from the two other methods EV and MBJ (Table 6.2). The band gaps which are calculated within this first group for $ZrSe_2$, ZrS_2, and ZrSeS are all also significantly less than the experimental data based on ARPES which has reported by Moustafa [294]. The second group contains EV and MBJ as E_{xc} functionals and gives band gaps almost comparable with the experimental results. But obviously EV is not as good as MBJ. Furthermore, the calculation based on MBJ has been performed in two modifications: by considering spin-orbit (SO) interaction and without it (WSO). Additionally, the indirect band gaps are presented in Table 6.3. Comparing these values with other methods in Table 6.2, it is clear that MBJ improved the band gap value. However the band gap decreases when considering SO interaction.

The results point out that the band gap linearly decreases from ZrS_2 to $ZrSe_2$ in all exchange-correlation energy methods which agrees with experimental data as discussed by Moustafa [294].

Table 6.2: Comparison of the indirect band gap for $ZrSe_2$, ZrS_2, and ZrSeS calculated with the six different exchange-correlation energy methods. For the MBJ method the band gap is given by considering with (SO) and without (WSO) spin-orbit interaction. The band gap linearly decreases from ZrS_2 to $ZrSe_2$ in all exchange-correlation energy methods. The energy units are electron volt.

Compound	PBE 96	LDA	WC	PBEsol	EV	MBJ		Experiment [294]
						WSO	SO	
ZrS_2	0.967	0.929	0.974	0.968	1.34	1.41	1.40	1.7
ZrSeS	0.78	0.54	0.582	0.72	1.17	1.18	1.13	1.40
$ZrSe_2$	0.56	0.49	0.51	0.51	0.86	0.92	0.81	1.18

The results show that among the functions we tested, MBJ remains superior for the estimating of the band gap. Such that recently, there are several research papers that have published the evaluation of the electronic structure of solids by the MBJ method [295, 296].

Table 6.3: Comparison of the direct band gap for $ZrSe_2$, ZrS_2, and ZrSeS calculated within the six different exchange-correlation energy methods. For the TB-MBJ method the direct band gap is given by considering with (SO) and without (WSO) spin-orbit interaction. The band gap linearly decreases from ZrS_2 to $ZrSe_2$ in all exchange-correlation energy methods. The energy units are electron volt.

Compound	PBE 96	LDA	WC	PBEsol	EV	TB-MBJ		Experiment [294]
						WSO	SO	
ZrS_2	1.62	1.52	1.57	1.57	1.88	2.05	2.01	2.10
ZrSeS	1.33	1.24	1.28	1.28	1.54	1.66	1.60	1.80
$ZrSe_2$	1.04	0.97	1.01	1.01	1.24	1.35	1.24	1.61

Tran and Blaha [284] have used the MBJ potential for several solids, such as strongly correlated 3d transition metal oxides (e.g. NiO), wide band gap insulators, and small band gap sp semiconductors and have demonstrated that for most cases the MBJ potential yields band gaps which are in good

agreement with experiment leading to typical errors of less than 10%. Recently, the MBJ potential has also been used for the II-VI-semiconductors CdTe and HgTe by Feng et al. [297] where their results point out that the MBJ potential reveals even for these compounds good agreement with experimental data while a significant difference is seen in LDA. Therefore MBJ potential has been found as an accurate method for the electronic structure of solids [295, 296].

6.4.2 Effect of lithium intercalation on the band gap of $ZrSe_{2-x}S_x$ by MBJ

The results of this section submitted to Cond. Matt. Phys. and cited as Ref. 298 in this thesis.

The observation of superconductivity upon the intercalation of elements into the Van der Waals gap of a transition metal dichalcogenide (TMDC) and subsequent suppression of charge density wave (CDW) formation causes these modifications to be a unique subject for experimental and theoretical research, whose foundations were laid by Wilson and Yoffe [299]. This is due to two reasons. First, pristine and intercalated TMDCs are suitable for a number of technological applications and second, it is believed that the origin of superconductivity in dichalcogenides and high-T_C cuprates are possibly related [300]. Regarding the first point, ternary $ZrSe_{2-x}S_x$ and $LiTiS_2$ have been discussed as promising candidates for third generation photovoltaic applications and cathodes in low voltage systems, respectively [301, 302, 303]. Regarding the second point, the way electronic order is established, leading to superconductivity, CDWs, or their coexistence in the TMDCs is a puzzling physical problem. Superconductivity can be seen for instance in TMDCs by intercalation of lithium or copper, i.e. by chemical pressure or under hydrostatic pressure both leading also to a T_C increase [304]. For instance, transition temperatures for Li_xZrS_2 and Li_xZrSe_2 have been reported in the 1.00 K-1.94 K and 0.50 K-1.05 K regime, respectively, for powder material [305] what has been confirmed for $x>0.4$ also for Li_xZrSe_2 single crystals [306, 307]. In some cases the CDW must be suppressed prior to the formation of the

superconducting state [11]. But also, a possible interrelation between superconductivity and the CDW state has been discussed by the observation of superconductivity in $CuTiSe_2$ [11]. There is increasing consensus that the mechanism leading to CDW formation is of excitonic nature [304, 308-312] at least for some TMDCs. The alternative, often used concept of nesting, previously often applied to describe the origin of a CDW, is based on the Peierls electronic instability for a purely one-dimensional metal. This was adapted to two-dimensional systems claiming the CDW to occur if the Fermi surface contours coincide when shifted along the observed CDW wave vector. However the importance of this concept for two-dimensional CDW systems was questioned recently [313].

The structure of quasi two-dimensional layered $ZrSe_{2-x}S_x$ is similar to other 1T transition metal dichalcogenides. The zirconium planes are sandwiched between two sulphur/selenium (chalcogenide) layers. Therewith the structure consists of trilayers, which are bonded by strong covalent bonds inside these trilayers, whilst relatively weak Van der Waals forces (VWF) act between the outer chalcogenide planes. Therefore the weak Van der Waals forces between the trilayers allow the insertion of e.g. lithium atoms between these two adjacent chalcogenide planes forming a $LiZrSe_{2-x}S_x$ intercalated crystal. $LiZrSe_{2-x}S_x$ has a hexagonal crystal structure. The experimental lattice parameters and atomic positions are presented in table 6.4.

The computational Method was the same as applied for ZrS_xSe_{2-x} in the previous section. The self-consistency is obtained using $G_{max}=14\ (au)^{-1}$, a 500 k-point mesh in the irreducible Brillouin zone, and $R_{MT}K_{max}=8.5$. Using optimized values of $R_{MT}K_{max}$, G_{max}, and number of k-points the theoretical lattice constants were extracted (see Table 6.4) by minimizing the total energy of the crystal to the volume in the PBE functional and were compared with experimental results. For the quaternary compound LiZrSeS no experimental lattice constants have been reported. Therefore, we used the average experimental values of $LiZrS_2$ and $LiZrSe_2$ for the experimental lattice constants. Finally, by the theoretical lattice constants (see Table 6.4) the

density of states (DOS) and band structure were calculated within i) PBE functional and ii) MBJ potential.

For the three TMDC compounds $LiZrSe_2$, $LiZrS_2$, and LiZrSeS our band structure calculations show that the VBM and the CBM are located at the Γ and L points, respectively. The terms VBM and CBM relate to the parent compounds without lithium intercalation, i.e. to ZrS_xSe_{2-x}.

Table 6.4: Calculated optimized lattice parameters within the PBE functional for $LiZrSe_2$, $LiZrS_2$, and LiZrSeS with hexagonal crystal structure. The experimental lattice parameters are given in parentheses [303, 305].

Compound	a, b (Å)	c (Å)	Space group	Atomic position			
					x	y	z
$LiZrSe_2$	3.761 (3.732)	6.690 (6.637)	P-3m1	Li	0	0	0.5
				Zr	0	0	0
				Se	2/3	1/3	0.75
				Se	1/3	2/3	0.25
LiZrSeS	3.699 (3.691)	6.498 (6.483)	P3m1	Li	0	0	0.5
				Zr	0	0	0
				Se	2/3	1/3	0.75
				S	1/3	2/3	0.25
$LiZrS_2$	3.630 (3.65)	6.295 (6.33)	P-3m1	Li	0	0	0.5
				Zr	0	0	0
				S	2/3	1/3	0.75
				S	1/3	2/3	0.25

Therefore, the lowest former unoccupied conduction band now crosses the

Band structures were calculated along the symmetrical lines of the Brillouin zone (see inset of FIG. 6.3d), i.e. from the Γ point with the coordinates (000) to

the K point (0.33333 -0.66667 0), to the M point (0.5 -0.5 0), to the A point (0 0 0.5), to the H point (0.33333 -0.66667 0.5), and to the L point (0.5 -0.5 0.5). Intercalated lithium causes a shift by about 2 eV towards lower binding energies for all bands when compared to the pristine ZrS_xSe_{2-x} system. Fermi level. From this reason metallic behaviour appears in the band structure of $LiZrS_xSe_{2-x}$, while the parent compound ZrS_xSe_{2-x} is a semiconductor with band gap values of 1.41 eV, 1.18 eV, and 0.92 eV for x=2, 1, and 0, respectively [277].

FIG. 6.3 shows the band structure and DOS for $LiZrS_2$ by MBJ and PBE (right and left sides, respectively) in which four groups of bands can be discerned. The first one with the highest binding energy at -14 eV has mainly sulphur-s state contributions. The second group is about from -7 eV to -2 eV in which the contribution of sulphur-p states is larger than that of Zr-d states.

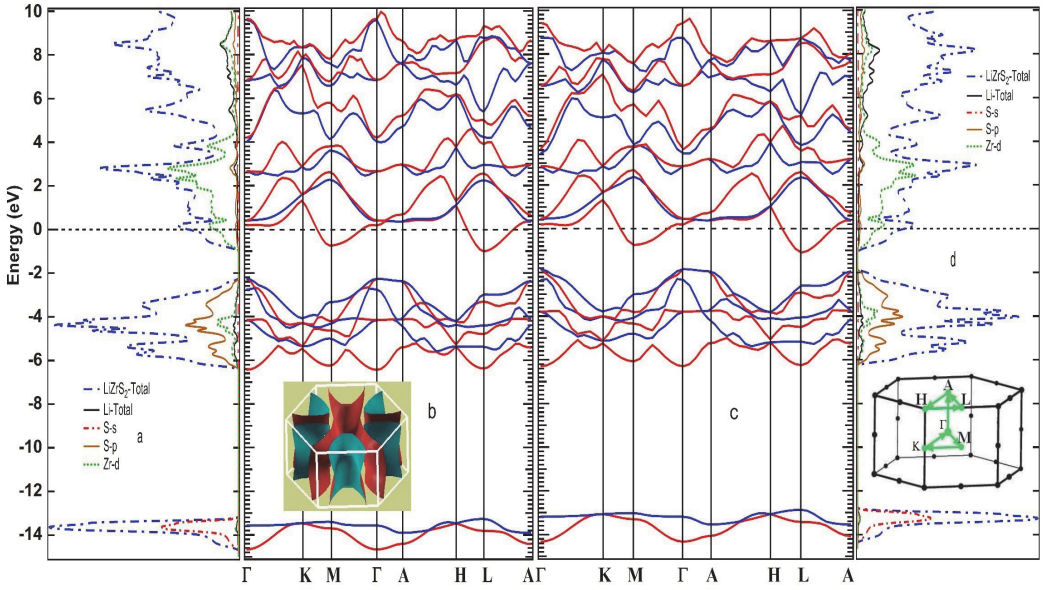

FIG. 6.3: Band structure and partial and total density of states (DOS) of $LiZrS_2$ calculated within the MBJ method (a and b) and PBE functional (c and d). The band structure shown in red and blue for ease of viewing. The insets in b and d show the Fermi surface of $LiZrS_2$ and Brillouin zone.

Furthermore, in the sulphur-p DOS the contribution of p_x+p_y is larger than p_z. The third group consists of bands from -1 to 3 eV which cross the Fermi level. In this group contributions of Zr-d states are stronger than that of sulphur-p

states. The last group which is situated above 3 eV has more contributions of sulphur than of zirconium states.

All bands are shifted down by about 2 eV towards lower energy in comparison with ZrS_2 [277] causing the third group of bands to cross the Fermi level. Metallic behaviour appears due to intercalated Li into the crystal structure. The energy gap between ΓM and ΓL for $LiZrS_2$ compounds within MBJ method and PBE functional are presented in Table 6.5. The band structures and partial and total DOS of $LiZrSe_2$ of the two cases are shown in FIG. 6.4. Furthermore, FIG. 6.4 shows the revealed comparison of MBJ and PBE functional. It can be noticed a similar appearance as for $LiZrS_2$.

Table 6.5: Comparison of the energy gap between ΓM and ΓL for $LiZrS_xSe_{2-x}$ compounds within MBJ method and PBE functional.

Compound	$E_{\Gamma M}$		$E_{\Gamma L}$	
	MBJ	PBE	MBJ	PBE
$LiZrS_2$	1.522	1.106	1.259	0.754
LiZrSeS	1.214	0.849	0.955	0.509
$LiZrSe_2$	0.933	0.607	0.702	0.273

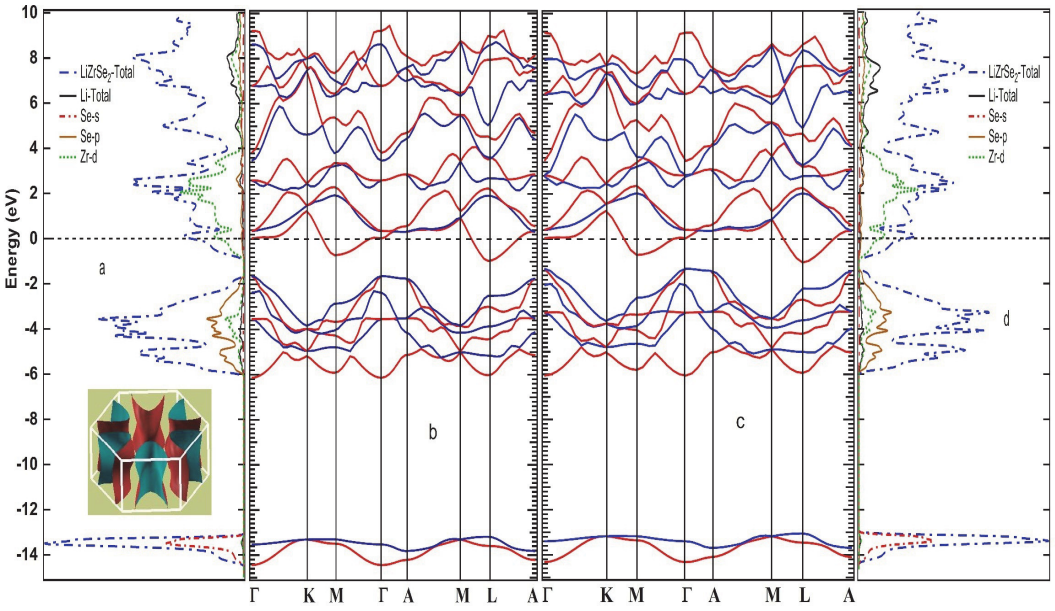

FIG. 6.4: The results of MBJ method (a and b) and PBE functional (c and d) for $LiZrSe_2$. The band structure is shown in red and blue for ease of viewing. The inset in a) shows the Fermi surface of $LiZrSe_2$.

The $E_{\Gamma M}$ gaps is 0.933 eV (Table 6.5) while in comparison with the parent compound $ZrSe_2$ (in the previous section) almost the same values is seen, i.e. 0.92 eV.

For the quaternary LiZrSeS compound the partial and total DOS and band structure are depicted in FIG. 6.5 by MBJ and PBE functional in the right and left side, respectively. The separation of the first group of bands around -14 eV binding energy into two bands can be seen in FIG. 6.5 which causes two different peaks in the total DOS. The lowest energy peak shows mainly contributions of Se-s states and the second one mainly contributions from S-s states (FIG. 6.5a). The energy between these two peaks is about 0.35eV. Moreover, the contribution of sulfur-p is more than that of selenium-p at the second group of bands. In addition, the $E_{\Gamma M}$ gap is 1.214 eV (Table 6.5) and 0.849eV for MBJ and PBE, respectively. While in ZrSeS the band gaps is 1.18 eV [277].

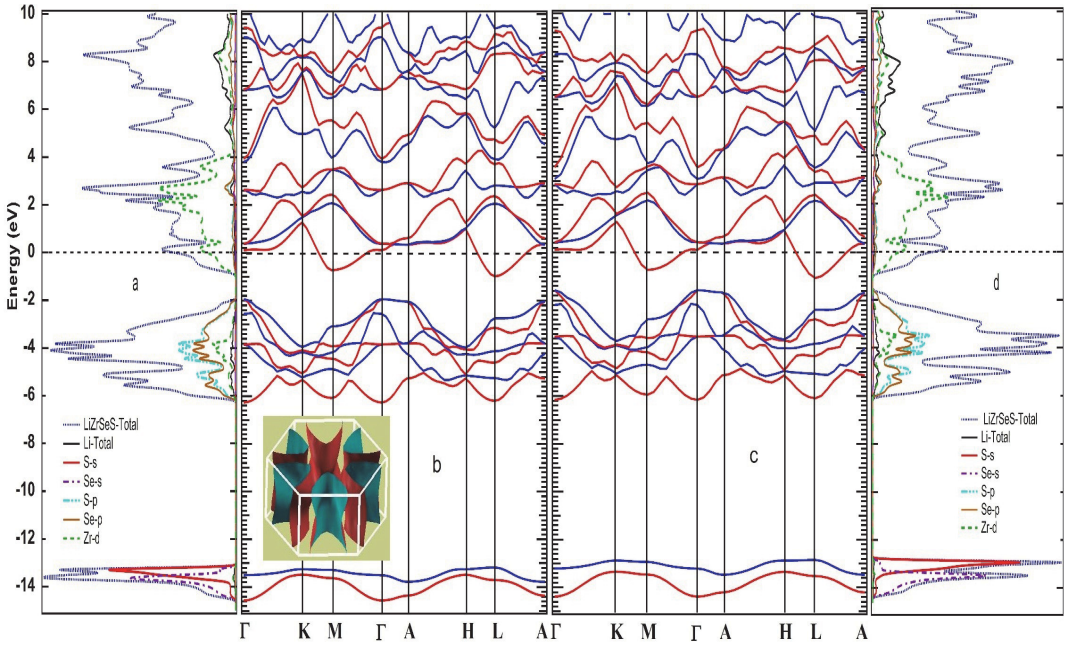

FIG. 6.5: Band structure and partial and total density of states (DOS) of LiZrSeS calculated within the MBJ method (a and b) and PBE functional (c and d). The band structure is shown in red and blue for ease of viewing. The inset in b shows the Fermi surface of LiZrSeS.

In Table 6.5 it is clearly revealed that the $E_{\Gamma M}$ and $E_{\Gamma L}$ gaps by MBJ potential are bigger than PBE functional. Unfortunately, there is not any experimental data for comparison.

Charge density waves and superconductivity as collective phenomena are often assumed to have common underlying physics. However the detailed mechanisms which are responsible to CDW formation and superconductivity are still an issue of condensed matter physics far from being understood. It will therefore continue to be a matter of an ongoing debate also in the TMDCs. For instance in Cu_xTiSe_2, only when the CDW transition reaches zero temperature a superconducting dome appears [11]. In Ref. 314 and 315 competition of CDW formation and superconductivity in Sulfur and in the high-T_C cuprates has been discussed. The occurrence of the above quoted phenomena can be due to different origins. In a simple model the interplay between conduction electrons, phonons, and excitons can be expressed by the following Hamiltonian [310].

$$H=H_{non\text{-}e}+H_{e\text{-}p}+H_{exc} \qquad (6\text{-}28)$$

where $H_{non\text{-}e}$ describes the bands of noninteracting electrons, while the last two terms are due to electron-phonon and electron-hole interactions, respectively (where creation of an exciton is due to Coulomb interaction between electrons and holes). A CDW may appear in different scenarios like i) directly due to $H_{e\text{-}p}$ (same as the Jahn-Teller effect) or ii) by forming an excitonic insulator H_{exc}, or iii) by a combination of the last two effects [310, 316]. The same holds for superconductivity [310, 316].

$LiZrSe_{2-x}S_x$ (x=0,1,2) may pose a means to disentangle the interactions and features leading to CDW and superconductivity. From experimental studies [306] it is known that these materials at certain lithium content possess a transition to the superconducting state but possibly no CDW state, because the resistivity curve shows linear behaviour down to the onset of superconductivity. As for a nearly pure Zr-d metal with some S/Se p-state admixture the conducting properties will result only from these states, forming large barrels along the LML lines of the Brillouin zone as in the case of other

TMDCs. The decisive difference is the lacking Fermi surface centred around the Γ point formed from transition metal p states in other TMDCs like $TiTe_2$, $TaSe_2$, and others. So at least the superconducting properties are clearly ascribable to the Zr-d and S/Se p-states. In the context of the possible competition of superconducting and charge ordered state (CDW) it is also worthwhile to discuss the excitonic background of the charge density wave in certain transition metal dichalcogenides. Recent publications showed for $TiSe_2$ [317], that the interaction of p-electrons from the Γ point with d- holes at the L point lead to excitonic states whose spanning vectors are the reason for the CDW state. As shown by these detailed studies by using the dipole moment of adsorbed H_2O the p-d band overlap between Gamma and M-point is the decisive parameter whether a CDW forms or not. One may argue then that this electron hole interaction is not possible in the case of LiS_xSe_{2-x} because the p-type bands at the Gamma point are shifted to higher binding energies, bringing them to an energy separation of 2 eV from the Fermi level and 1 eV from the d-bands. This makes an exciton formation between them impossible. Therefore one may be able to study the reduced Hamiltonian $H=H_{non\text{-}e}+H_{e\text{-}p}$ without the H_{exc}-term.

Regarding electronic systems with reduced dimensionality providing access to basic physical concepts like the Fermi liquid TMDCs have played an important role [318]. Here for instance the line shape of photoelectrons emitted from the $3d_z^2$ band of $TiTe_2$ have been fitted with Fermi liquid and non-Fermi liquid spectral functions. Its property as potential Fermi liquid reference compound has found ample discussion [319]. However, relatively early it was noted by Allen and Chetty [320] that the transport properties do not one by one correspond to the ARPES data. First, the electron phonon coupling constant λ_{tr} = 0.7-0.8 derived from the conductivity measurements suggested a suppression of the superconductivity by some effect like a CDW or any other reason, since no transition to the superconducting state was observed down to 1.1 K. Interestingly a weak CDW related hysteresis was reported by deBoer et al. [321] on slightly non stoichiometric $Ti_{1.01}Te_2$ from magnetic susceptibility data around 150 K, but so weak, that it was not detectable in the arrangement of the

atoms. An almost linear resistivity curve was reported [322]. Second, the resistivity derived from the ARPES data was found to be quadratic and strongly deviating from the linear behavior found from experiment [321]. In this context Claessen et al. [322] reported on a detailed comparison of the dispersion of the $3d_z^2$ band between DFT theory and ARPES. The observed renormalization was ascribed to electron-electron interaction. It may from these reasons be interesting to study the more simple system $LiZrSe_{2-x}S_x$ (x=0, 1, 2) also by ARPES and transport measurements. This can possibly provide an alternative access to the dispersion of a d_z^2 band crossing the Fermi surface. Any potential disturbing influence from other Fermi surface sheets, especially the chalcogenide p bands centred around the Γ point in TMDCs like $TiTe_2$ should not be present, so that the electron-electron renormalisation of the d_z^2 band can be compared on a different system.

6.5 Electronic structure of Bi-2212

The results of section 6.5 will submit to Phys. Rev. B and cited as Ref. 323 in this thesis.

The band structure of $Bi_2Sr_2CaCu_2O_8$ has also been calculated by DFT with experimental lattice parameters [324-327]. While the optimization of the volume and atomic positions were not taken in their calculation. The results revealed a metallic ground state instead of the AFM insulator realized in nature. Additional, Bellini et al. [328] have investigated the effect of optimization of the crystal parameters and atomic positions in the electronic structure of averagely distorted orthorhombic Bi-2212 compound by full-potential method. This calculation revealed a metallic ground state for undoped Bi-2212 compound. However, Bellini et al. [328] have shown that only within the orthorhombic distorted cell it is possible to reproduce the secondary structures of Fermi surface observed in photoemission spectra.

The electronic structure of Bi(Pb)-2212 by DFT is calculated in this section. The calculations were performed within the DFT framework using the Wien2k

[290] and Quantum Esperesso packages [329]. The full-potential method is used in Wien2k, while the pseudo-potential method is used in Quantum Esperesso. As similar results were obtained by both packages, only the results of Wien2k package are presented here. The calculation method is discussed in the next section.

6.5.1 Computational method

Experimental lattice parameters and atomic positions from Ref. [14] were used in the tetragonal structure, as discussed in section 2.1. The k-points, G_{max} and $R_{MT}K_{max}$ (where R_{MT} represents the smallest muffin-tin radius and K_{max} is the maximum size of the reciprocal lattice vectors) were optimized by convergence tests beginning at $G_{max}=12$ $(au)^{-1}$, $R_{MT}K_{max}=6$ and k-points=100, while the valence wave functions inside the spheres were expanded up to $L_{max}=10$. A self-consistent iteration was repeated until a charge convergence of 0.00001 e was reached. The convergence was obtained using $G_{max}=14$ $(au)^{-1}$, a 500 k-points mesh in the irreducible Brillouin zone, and $R_{MT}K_{max}=8.5$. Using the optimized values of $R_{MT}K_{max}$, G_{max}, and the k-points and experimental lattice parameters, the volume was optimized by minimizing the total energy of the crystal over the volume in the PBE functional. FIG. 6.6 shows the fitting parameters obtained from the Murnaghan equation of state [330], after which the theoretical lattice constants were extracted, as presented in Table 6.6.

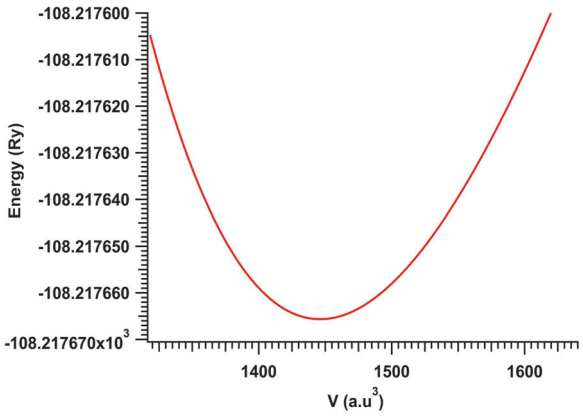

FIG. 6.6: Volume optimization by minimizing the total energy in the PBE functional. The parameters were fitted using the Murnaghan equation of state [330].

The density of states (DOS), the band structure, and the x-ray absorption spectra of the CuL_3 and O K edges were calculated using the theoretical lattice constants from several classes of the GGA and MBJ functionals.

Table 6.6: Experimental and theoretical lattice parameters, where the theoretical parameter is obtained by using the PBE functional.

	a (Å)	c (Å)
Experimental	3.812	30.66
Theoretical	3.774	30.35

It is well known that the LDA and GGA functionals fail to find band gaps in strongly correlated materials, such as high-T_C cuprates, transition metal oxides, 3d itinerant magnets, and heavy-fermion compounds [331]. This problem with the GGA or LDA functionals is believed to be due to not accounting sufficiently for the correlation effects of the localized d and f orbitals. One approach to solving the problem is to use the LDA/GGA+U method [89], in which U is called the onsite Coulomb energy and is also known as the Hubbard U. The Hubbard parameter U can be calculated by the ab initio method. In the Wien2k package, it is also possible to add the local screened Coulomb Hubbard correlations U between localized orbitals to the one-particle component of the LDA or GGA Hamiltonian, which is known as the DFT+U method. This separates the system into two subsystems: i) the Coulomb d-d interaction is accounted for by a term $\frac{1}{2}\sum_{i\neq j} n_i n_j$ for the localized d or f orbitals, and ii) delocalized orbitals, such as s or p orbitals, are described by the LDA or GGA functionals. The Hubbard parameter, U, is described as the cost in Coulomb energy for placing two electrons at the same site [332]. For instance, U for d-electrons is given by

$$U=E(N_d+1)+ E(N_d-1)-2E(N_d) \qquad (6\text{-}29)$$

where $E(N_d)$ is the ground state energy with N_d electrons in the d orbital. Schnell et al. [333] used this method to find that a value of 5eV for the U

parameter in the fcc copper crystal. In the present work, the Hubbard U in the $CaCuO_2$ and Bi-2212 cuprates has been calculated using the method proposed by Anisimov and Gunnarsson [332], which has also been discussed by Madsen and Novak [333]. These authors have argued that the screened Coulomb integral $F_{eff}^{o} = U - J$ can be estimated using screened Coulomb integral F_{eff}^{0} which is given by [332]

$$F_{eff}^{0} = \varepsilon_{3d\uparrow}(\frac{n+1}{2},\frac{n}{2}) - \varepsilon_{3d\uparrow}(\frac{n+1}{2},\frac{n}{2}-1) - \varepsilon_{F}(\frac{n+1}{2},\frac{n}{2}) + \varepsilon_{F}(\frac{n+1}{2},\frac{n}{2}-1) \quad (6\text{-}30)$$

where $\varepsilon_{3d\uparrow}$ is the spin-up 3d-eigenvalue and ε_F is the Fermi energy. Using this method, values of 6.258 eV and 6.476 eV have been obtained for U in $CaCuO_2$ and Bi-2212, respectively.

LDA/GGA+U method has been widely used for evaluation of the electronic structure of HTC [334- 336]. For instance, Czyzyk and Sawatzky [334] have investigated the electronic structure of La_2CuO_4 and $LaCuO_3$ by the localized spherical wave method. They have found AFM ground state by LDA+U method in which U was 7.42 eV and 11 eV respectively, for Cu and La. Furthermore, Lopez et al. [335] have discussed the electronic structure of $YBa_2Cu_3O_{6+y}$ by GGA+U method based on pseudo potential method. They have found AFM gap by U_{eff}=9 eV. Finally, recently Moreira et al. [336] have applied LDA+U method to $HgBa_2Ca_{n-1}Cu_nO_{2n+n}$ (n=1, 2, 3) with U value of 8 eV and 5 eV respectively, for Cu and Hg atoms. Their results point out to the crucial role of HgO_2 to magnitude of the insulating gap as well as inability of LDA+U method to find AFM band gap in n=3 compound of the last family of $HgBa_2Ca_{n-1}Cu_nO_{2n+n}$.

6.5.2 Band structure and density of states

As discussed in section 2.1, the crystal structure of Bi-2212 can be described as a stack of basic Bi-2201 units with a $CaCuO_2$ slab inserted. It is a good idea to first determine the electronic structure of $CaCuO_2$, which has a tetragonal structure with space group number 123 (P4/mmm). The experimental lattice

parameters for calculating the electronic structure of $CaCuO_2$ were taken from Ref. 337 (a=3.86Å, c=3.20Å).The theoretical lattice parameters were found using the PBE functional with G_{max}=14, $R_{MT}K_{max}$=8.5, and a 600 k-points mesh in the irreducible Brillouin zone (a convergence test was performed for G_{max}, $R_{MT}K_{max}$, and the k-points prior to the calculation). The iteration process was repeated until a charge convergence of 0.000001 e was reached. The theoretical lattice parameters a=3.83°A and 3.176°A were calculated using the PBE functional. Finally, the calculations were performed using the LDA and several classes of GGA formalisms such as PBE, WC, PBEsol and MBJ. Using these different formalisms, the ground state was found to possess metallic properties, instead of being an AFM insulator. The calculation was therefore repeated with the GGA+U, where a value of 6.258 eV from an ab initio calculation was used for U, as discussed in the previous section. The results from the MBJ+U method were comparable to the experimental data. The calculation of the electronic structure of $CaCuO_2$ by MBJ+U is discussed next. The band structure and the DOS of $CaCuO_2$ are shown in FIG. 6.7. The band structure around the symmetry point of the BZ reveals a band gap of approximately 1.52 eV. The band gap is comparable to the experimentally measured energy gap of 1.5eV [338]. However, several electronic structure calculations for $CaCuO_2$ based on the local spin density approximation (LSDA), the linear muffin tin orbital atomic sphere approximation [339], the linearized augmented plane wave method [340], and the full potential linear muffin tin orbital method [341] have not found an antiferromagnetic ground state with an energy gap of 1.5eV [338]. In addition, LSDA+U calculations have produced AFM gaps of approximately 2.1eV and 1.96 eV for U=7.5 eV [89] and 5 eV [342], respectively.

FIG. 6.7 shows the DOS of the spin-up and spin-down states to the left and right sides of the band structure, respectively. Both the valence band maximum and the conduction band minimum are located at the A point. This indicates an AFM ground state with a direct gap of 1.52 eV. The O-p and Cu-d states appear to contribute significantly to the valence band, with the spin up (SU) O-

p_y and O-p_z states being smaller than those of the other orbitals in the valence band close to the Fermi level.

The conduction bands consisted of significant contributions from the copper $d_{x^2-y^2}$ spin down (SD) states. In addition, the splitting of the Cu-$d_{x^2-y^2}$ SU and SD states into the lower Hubbard (LHB) and upper Hubbard (LHB) bands, respectively, with an energy separation of approximately 10 eV, were significant when the O-p and other Cu-d states were located between the LHB and LHB bands.

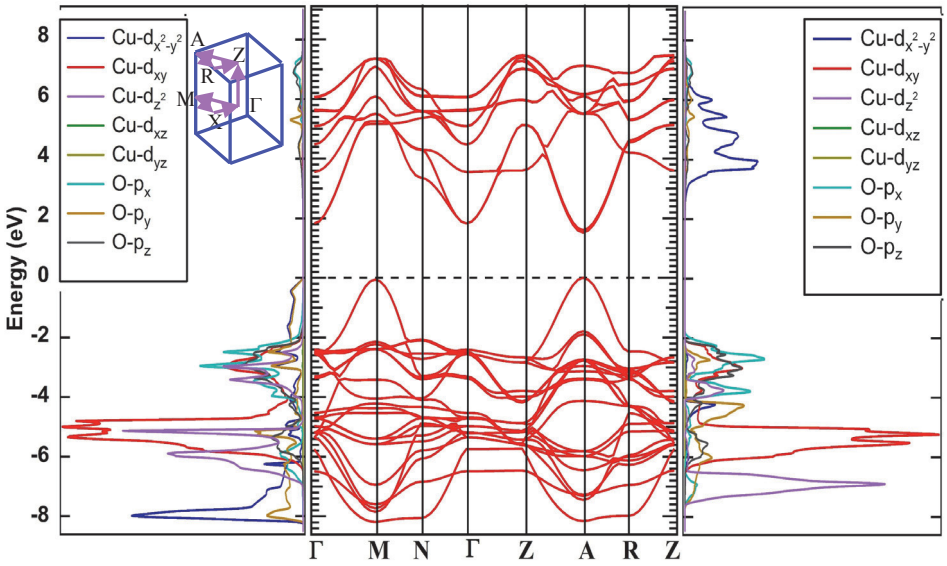

FIG. 6.7: Band structure and DOS of a $CaCuO_2$ compound, calculated using the MBJ+U method with U=6.258 eV. The right and left sides show the DOS of the SD and SU states.

This calculation also showed that the AFM ground state was not accessible by using the GGA+U method, in which the GGA was one of the PBE, WC, and PBEsol functionals. The roles of the O-p_y spin-up states and the copper $d_{x^2-y^2}$ spin-up states at the Fermi level were also obtained. With this information, we can now examine the Bi-2212 cuprate, which has two more Sr-O and Bi-O planes than the $CaCuO_2$ compound. Electronic structure calculations of the undoped Bi-2212 cuprate by GGA, GGA+U, and MBJ+U did not find the AFM ground state and predicted metallic properties instead. This result is used to discuss the electronic structure of the undoped Bi-2212 cuprate next.

The calculated band structure of the Bi-2212 cuprate, using the PBE functional, along the Γ→M→X→Γ directions of the BZ is shown in the middle of FIG. 6.8. This calculation predicts metallic behavior for the undoped Bi-2212 compound instead AFM insulating behavior. As discussed in section 2.1, three different oxygen sites exist in the Bi-2212 compound: oxygen in the Cu-O plane, apical oxygen in the Sr-O plane, and oxygen in the plane of Bi atoms. The left side of FIG. 6.8 shows the DOS in the Cu-O plane for individual orbitals. The right side of FIG. 6.8 also shows the DOS of these three different oxygen sites. The DOS clearly shows the role of oxygen in the Cu-O and Sr-O planes in the valence and conduction bands, respectively. In fact, the role of the apical oxygen, which was discussed in chapters two and four, is supported by this calculation. Furthermore, the role of the oxygen in the Bi-O plane in the valence and conduction bands is significant. The DOS on the left side of FIG. 6.8 shows that the contribution of the copper $d_{x^2-y^2}$ orbital at the Fermi level is also significant. A large contribution is observed from the Cu-d_{xz+yz} orbital in the valence band.

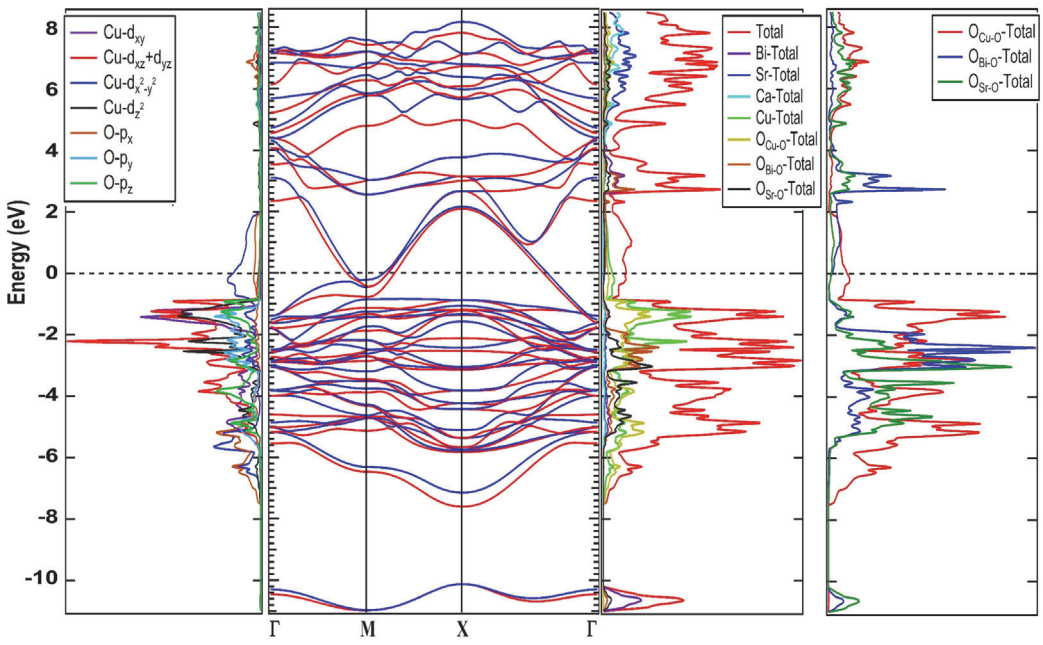

FIG. 6.8: Band structure and DOS (shown in red and blue for ease of viewing) of the Bi-2212 compound, calculated using the PBE functional. (The DOS in the Cu-O plane for individual orbitals is shown on the left. The DOS of the three different oxygen sites are shown on the right (see text)).

The contribution of the Bi atoms correspond to a lower energy of about -10 eV, while the contributions of the Sr and Ca atoms correspond to higher energies of more than 4 eV. As discussed above, the PBE functional failed to produce an AFM ground state for the undoped Bi-2212 compound.

However, this calculation leads to several significant results. The calculated band structure of the undoped Bi-2212 cuprate, based on the PBE+U method with U=6.476 eV, is shown in the middle of FIG. 6.9.

The contributions of all the orbitals in the CuO_2 plane with spin-up and spin-down states are shown on the left and right sides, respectively. This calculation, as in the MBJ+U results for $CaCuO_2$, produced splitting of the Cu-$d_{x^2-y^2}$ orbitals for the SU and SD states into the LHB and UHB bands, respectively. The energy separation of the LHB and UHB is observed to be approximately 2 eV less than that obtained for the $CaCuO_2$ compound in FIG. 6.7.

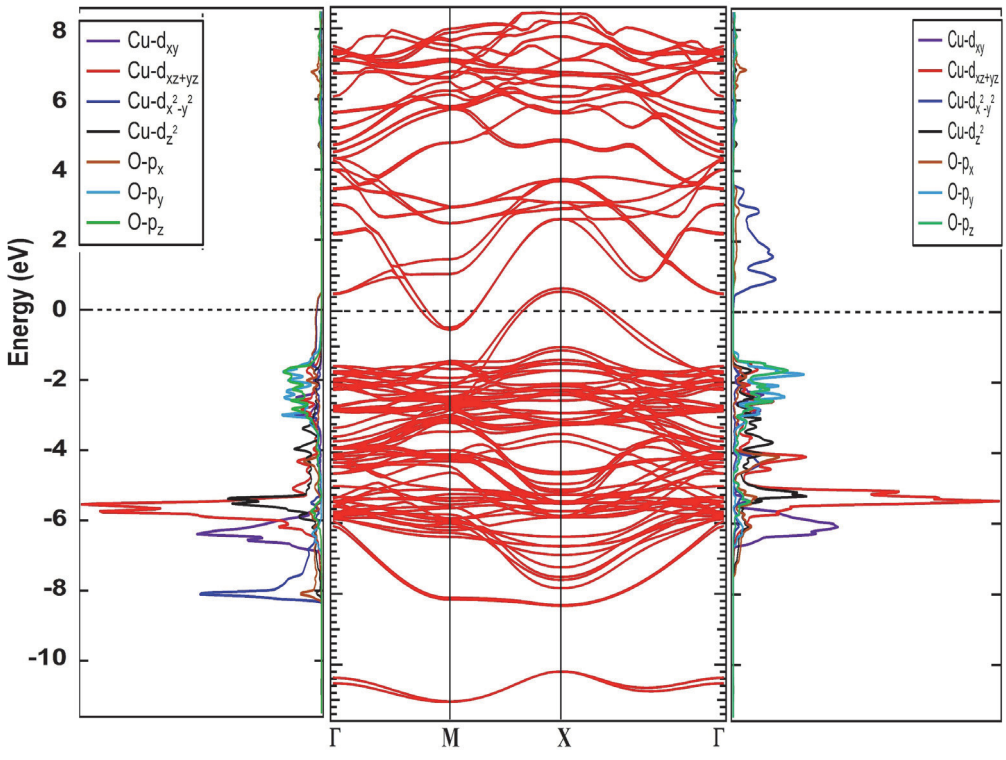

FIG. 6.9: The band structure of Bi-2212 calculated with the PBE+U functional is shown in the middle of the figure. The DOS of the individual orbitals in the CuO_2 plane with spin-up and spin-down states are shown on the left and right side, respectively. The splitting of the Cu-$d_{x^2-y^2}$ orbitals into the LHB and UHB bands can also be observed (see text).

Thus, the LHB is about -8 eV for both compounds, while the UHB is located at approximately 4 eV and 2 eV for $CaCuO_2$ and the undoped Bi-2212 compounds, respectively. However, this result is due to the failure of PBE+U to find an AFM ground state, which prevents some of the bands that cross the Fermi energy could not shift to lower energies. These bands are located around the M and the X points of the Brillouin zone.

FIG. 6.10a shows the band structure of an undoped Bi-2212 cuprate close to the Fermi level, which was calculated using the PBE and PBE+U functionals. It can be observed that some of the bands that cross the Fermi level at the M and the X points of the Brillouin zone have different curvatures for the PBE and PBE+U methods.

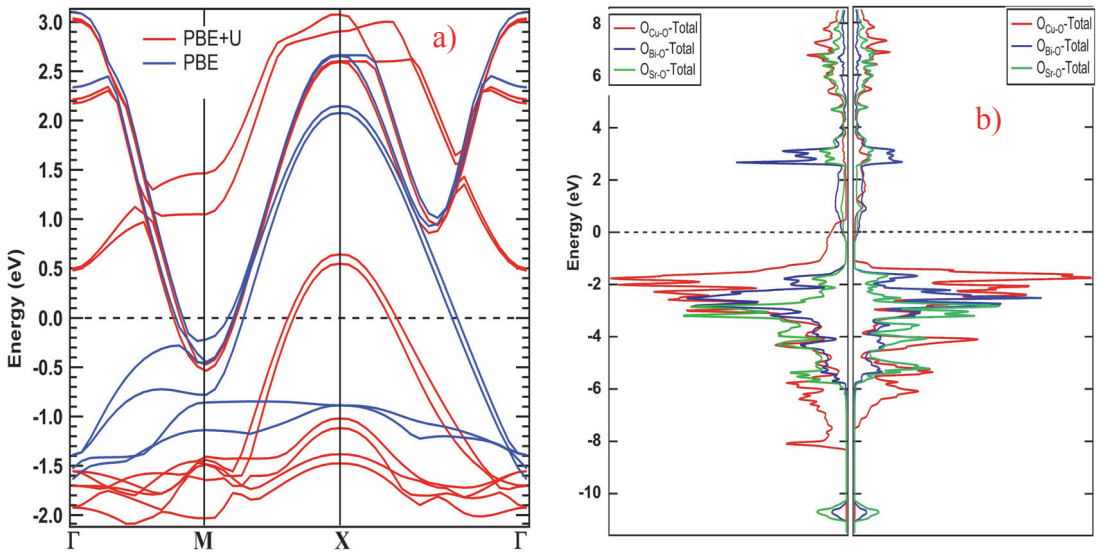

FIG. 6.10: a) Comparison of the band structure of the undoped Bi-2212 cuprate calculated by the PBE and PBE+U methods, which are shown by blue and red lines, respectively. b) DOS for three different oxygens sites in the undoped Bi-2212 compound using the PBE+U method, where the SD and SU states are presented on the right and left side, respectively.

For instance, two bands cross the Fermi level near the X point of the Brillouin zone (FIG. 6.10a) using the PBE functional, while the bands shifts approximately 1.5 eV to lower energy using the PBE+U functional. The behavior of the electron-like bands at the M point of the Brillouin zone is

almost the same for both functionals. The PBE+U method resulted in the separation of some bands at the Fermi level, but the method also failed to find an AFM ground state, as in the calculation based on the PBE functional.

FIG. 6.10b shows the DOS of the SU and SD states for the three different oxygen sites in the undoped Bi-2212 compound, calculated using the PBE+U functional, on the right and left side, respectively. The SU and SD states for the planar oxygen (i.e. the oxygen in the CuO_2 plane) play a greater role in the valence band than for the other orbitals. However, the SU and SD states of the apical oxygen play a greater role in the conduction band than for the other orbitals. These results are almost the same as for the calculations using the PBE functional in FIG. 6.8.

Additionally, FIG. 6.11 shows the band characters of undoped Bi-2212 by the PBE+U method. It is revealed that the bands crossing the Fermi energy have Sr-atom (FIG. 6.11d), apical oxygen (FIG. 6.11g), and minor Bi-atom (FIG. 6.11a) characters. In the Sr-atom as shown in FIG. 6.11h the role of the d-orbital is larger than that of the other orbitals. These results also revealed the role of the apical oxygen as discussed in chapter 4.

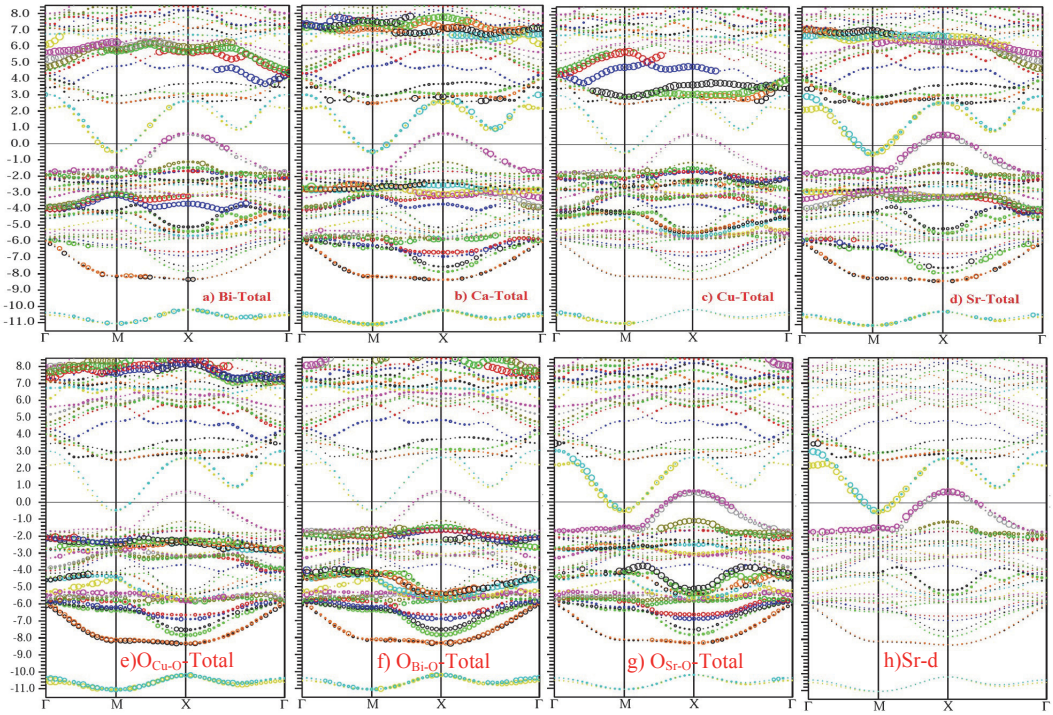

FIG. 6.11: The band characters of undoped Bi-2212 by the PBE+U method.

Finally, FIG. 6.12 shows the electron density in the CuO_2 plane of undoped Bi-2212 calculated using the PBE functional, where the electron density at the copper sites is much greater than at the oxygen sites.

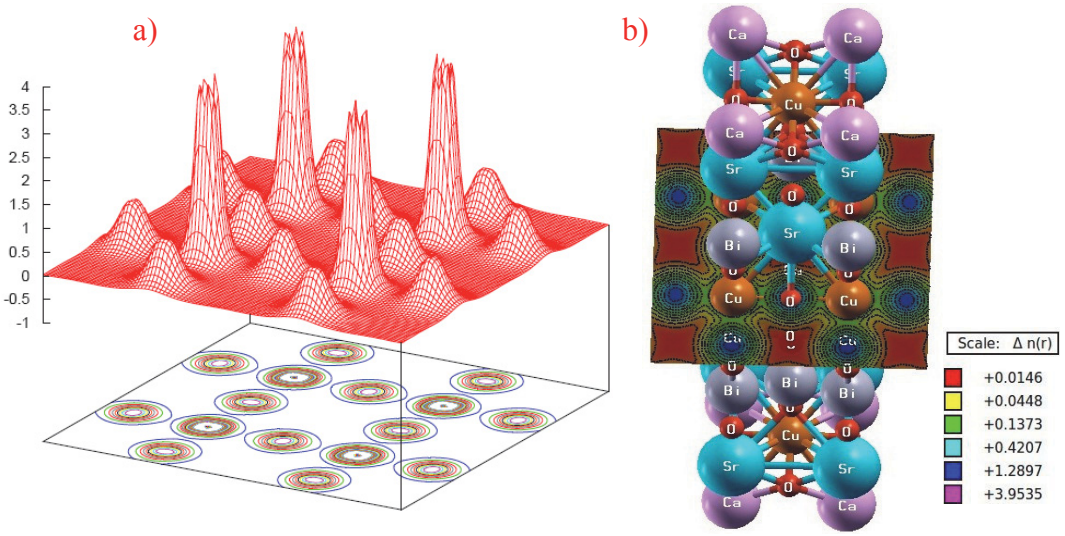

FIG. 6.12: Electron density in the CuO_2 plane in a) three-dimensions and b) two-dimensions. The electron density was calculated using the PBE functional.

The failure of PBE+U could be due to the doped charge from Sr-O and Bi-O planes which supported by band characters in FIG. 6.11a and d. This effect in the Bi(Pb)-2212 cuprate appears to make it impossible to find an AFM ground state using the LDA/GGA functionals and also the GGA+U method. This problem has solved in $HgBa_2Ca_{n-1}Cu_nO_{2n+n}$ with n=1, 2 by U=8 eV and 5 eV for Cu and Hg atoms, respectively [336], while the problem still exists for n=3. Thus, we tried to produce the AFM ground state within PBE+U method by including the Hubbard U for the Bi, Sr, and O atoms which means that the system is manipulated. However, including the Hubbard U also did not produce the AFM ground state in the undoped Bi-2212 cuprate. Finally, we tried using a very large value for U, such as 10 eV, in the calculation. Unfortunately, the AFM ground state was still not predicted. As discussed

above similar inability of GGA+U has found in $HgBa_2Ca_{n-1}Cu_nO_{2n+n}$ with n=3 [336].

It should be noted that my calculations for the electronic structure of the undoped high-T_C cuprate $YBa_2Cu_3O_6$ reveal an AFM ground state by the PBE +U and MBJ+U method. The calculations have been performed with G_{max}=14 $(au)^{-1}$, $R_{MT}K_{max}$=8.5, k-points=500, and U=8 eV within the theoretical lattice parameters (a=b=3.877Å, c=11.867 Å). They were extracted from experimental data of Ref. 343 by minimizing the total energy in the PBE functional. The parameters were fitted using the Murnaghan equation of state [330] as discussed in section 6.5.1. The results of the band structure and DOS calculationed by PBE+U are given in FIG. 6.13. It reveals an AFM ground state with a gap of 0.71 eV which is lower than in experimental data.

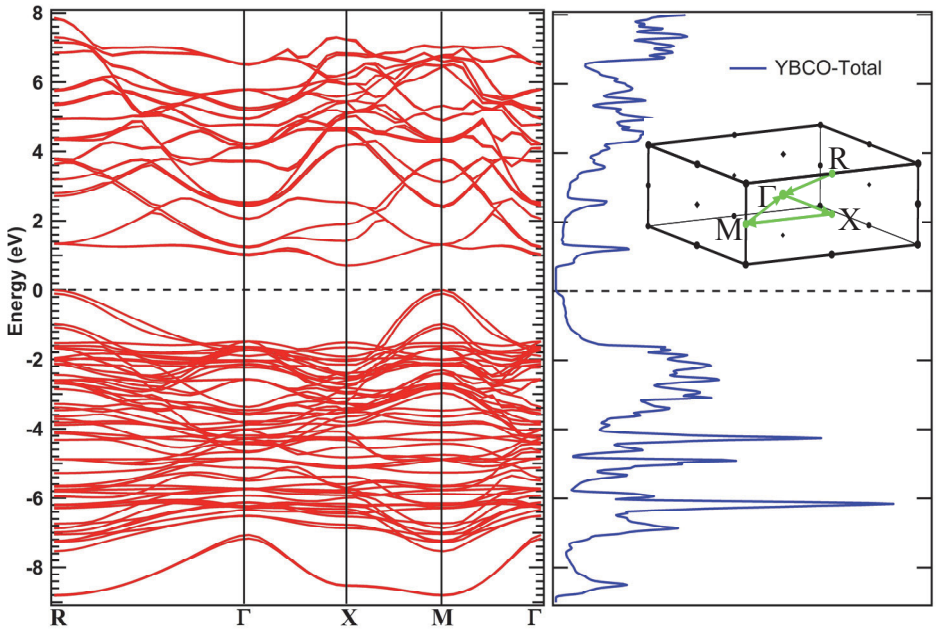

FIG. 6.13: Band structure of undoped $YBa_2Cu_3O_6$ calculated with the PBE+U functional (left). Right: Total DOS of undoped $YBa_2Cu_3O_6$. The inset shows the Brillouin zone.

Furthermore, FIG. 6.14 shows the band structure and DOS of undoped $YBa_2Cu_3O_6$ calculated by the MBJ+U method. It clearly reveals a larger band gap which is 1.53 eV. We should keep in mind that $YBa_2Cu_3O_6$ has two CuO_2 planes which are sandwiched between two Ba-O layers. Bi-2212, however,

contains two slabs such that each slab contains one formula unit of $Bi_2Sr_2CaCu_2O_8$. So the two CuO_2 planes are sandwiched by two SrO and BiO layers as discussed in section 2.1. Therefore, Bi-2212 has more layers than YBCO, and as mentioned above, doped charge from the Sr-O and Bi-O planes could be the failure of GGA+U to find no AFM ground state in the Bi-2212.

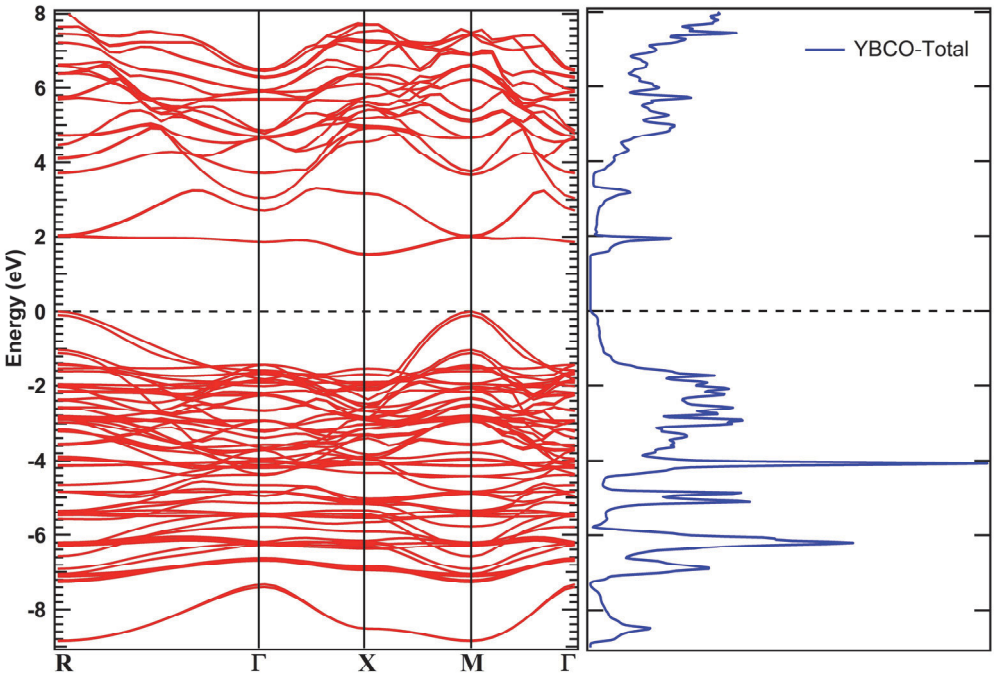

FIG. 6.14: Band structure and DOS of undoped $YBa_2Cu_3O_6$ calculated with the MBJ+U functional.

6.6 X-ray absorption spectroscopy by DFT

Experimental measurements using XAS for the temperature and polarization dependence of Bi(Pb)-2212 single crystals was discussed in chapter four. Several significant conclusions were drawn, including the inability of the Gor'kov and Teitel'baum formula to fit our data. The problem was solved by adding an additional term (i.e., $T^{3/2}$) to the Gor'kov and Teitel'baum formula. The role of the other orbitals, which was validated by the ARPES data in chapter 5 and the DFT calculation in the previous section, is discussed here. Next, XAS calculations by DFT with the Wien2k code are presented for the undoped Bi-2212 cuprate. However, the polarization and temperature

dependence of the XAS spectra can not be calculated with the Wien2k package.

In 1987, Müller and Jepsen [344] calculated x-ray absorption spectra (XAS) for the first time using DFT. They used the linear augmented-plane-wave method (as discussed in section 6.3) for calculating the *K*-edge photoabsorption spectra of the 4*d* metals, so their results were in good agreement with the measured data. XAS spectra can also be calculated using the multiple scattering method (MSM), which works in real space. This method was developed by Durham et al. [345]. Later, Greaves calculated the XAS spectra of copper using the MSM method, as discussed in Ref. 346. However, the advantage of calculating the spectra by DFT with the Wien2k code is that several physical properties, such as the band structure, the density of states, and the electron density can be derived from the same calculation, as discussed in the previous section. Note that DFT can not predict excited state properties, as it is a ground state theory. Thus, DFT can only be used to calculate ground state properties.

In the Wien2k package, the dipole x-ray emission intensity is given by [347]

$$I(\omega) \sim \omega^3 \sum_{\nu} |< \psi_c \,|\, \vec{r} \,|\psi_\nu >|^2 \; \delta(E_\nu - E_c - \omega) \qquad (6\text{-}31)$$

where ψ_ν is the eigenstate of a Hamiltonian H with eigenenergy E_ν, and ψ_c denotes the core eigenstate localized around an atom with eigenenergy E_c.

Within the muffin-tin approximation, equation (6-31) can be written as [348]

$$I(\omega) \sim \omega^3 [f_{l,l-1}(E) n_{A,l-1}(E) + f_{l,l+1}(E) n_{A,l+1}(E)] \qquad (6\text{-}32)$$

where $f_{l,l'}$ is the oscillatory strength given by

$$f_{l,l'} = \frac{l + l' + 1}{2(2l' + 1)} A_{l,l'}^2 \Big/ \int_0^{r_s} R_{Vl}^2 r^2 dr \qquad (6\text{-}33)$$

where r_s is the radius of a muffin-tin sphere, R_{Vl} is the solution of the radial Schrödinger equation corresponding to the eigenenergy E_ν, and $A_{l,l'}$ represents integrals involving the core and valence wave function as follows:

$$A_{l,l'} = \int_0^{r_s} R_{cl}(r) R_{Vl}(r) r^3 dr \qquad (6\text{-}34)$$

FIG. 6.15 shows the calculated CuL_3 absorption spectra for the undoped Bi-2212 cuprate, where the energy is related to the Fermi energy. This calculation was performed using the PBE functional with a 500 k-points mesh in the irreducible Brillouin zone. We could not find any significant difference between spectra for a high value of k-point such as the 5000 k-point mesh in the irreducible Brillouin zone. It was not possible to account for the polarization geometry in the calculation. The white line in FIG. 6.15 is due to a dipole transition $2p^63d^9 \rightarrow 2p^53d^{10}$ that was qualitatively produced using the PBE functional. This peak occurs at an absorption energy of 931.2 eV, as discussed in section 4.2.

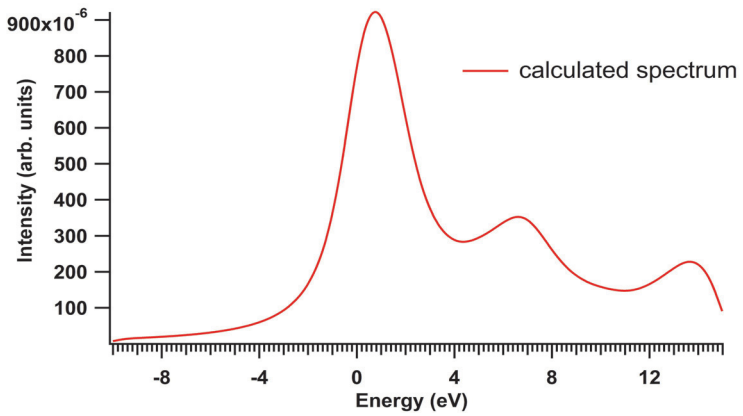

FIG. 6.15: Calculated CuL_3 absorption spectra for the undoped Bi-2212 cuprate using the PBE functional. The energy is related to the Fermi energy.

The DFT calculation produced two additional peaks at approximately 7 eV and 14 eV, which have not been observed experimentally by x-ray absorption spectroscopy on an undoped Bi-2212 cuprate.

The smooth background was subtracted by a straight line for the white line analysis in FIG. 6.16. The absorption line was fitted by pseudo-Voigt functions. FIG. 6.16 shows that the CuL_3 spectra consist of two peaks, known as a white line (0.56528 eV) and a satellite line (1.914 eV), as discussed in section 4.2. The peaks are due to a $2p^63d^9 \rightarrow 2p^53d^{10}$ dipole transition and a $2p^63d^9\underline{L} \rightarrow 2p^53d^{10}\underline{L}$ transition, respectively, where the 'ligand hole' $\underline{L}$ denotes a 2p-hole at the oxygen sites surrounding the absorbing Cu atom in the CuO_2

plane. The hole density was calculated using a similar method to that discussed in section 4.2:

$$n_H = \frac{I_S}{I_S + I_W} \qquad (6\text{-}35)$$

where I_S and I_W are the intensities of the white line and the satellite line, respectively. A hole density of 0.113 holes per copper atom was found for the undoped Bi-2212 cuprate using the PBE functional. However, the experimental evidence indicated a zero hole density. Thus, the PBE functional can successfully qualitatively reproduce the CuL_3 absorption spectra of undoped Bi-2212 cuprate, but fails to quantitatively evaluate the hole density in the copper plane of the undoped Bi-2212 cuprate. For the undoped cuprate, the satellite line should be close to zero or vanish.

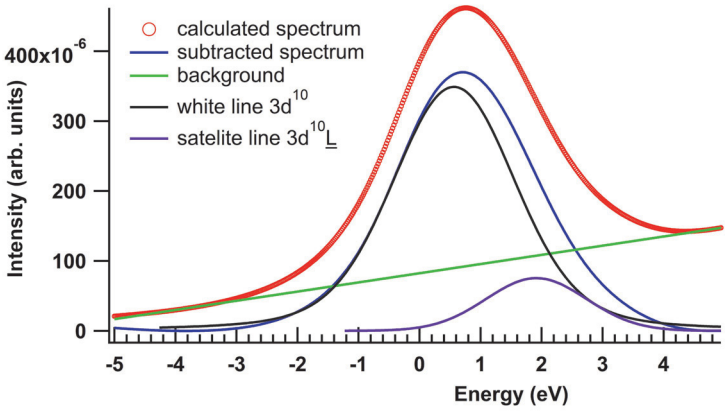

FIG. 6.16: Calculated CuL_3 absorption spectra using the PBE functional for the undoped Bi-2212 cuprate. The spectrum consists of two peaks, known as a white line (0.56528 eV) and a satellite line (1.914eV).

The O K edge spectrum of the undoped Bi-2212 cuprate is shown in FIG. 6.17, as calculated (in the same manner as for the CuL_3 edge) by the PBE functional. As discussed in section 4.4, the O K absorption spectra for Bi(Pb)-2212 single crystals consists of a prepeak and a second peak due to the transitions from $1s \rightarrow 2p$ and $1s^2 3d^9 \rightarrow 1s 3d^{10}$, respectively. In chapter 4, it was also discussed that the intensity of the prepeak is proportional to the hole density in the CuO_2 plane. Thus, there was no prepeak in the experimental data for the undoped

compound. However, FIG. 6.17 clearly shows a prepeak for the undoped Bi-2212 cuprate. This also results from the failure of the PBE functional to produce quantitatively accurate absorption spectra for the O K edge in the undoped Bi-2212 cuprate. However, PBE qualitatively produces an O K edge spectrum for the undoped Bi-2212 cuprate.

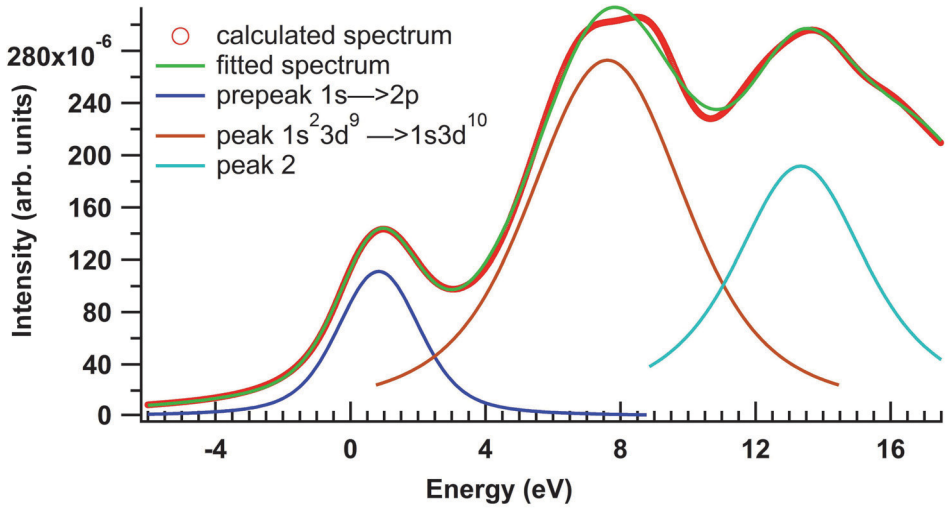

FIG. 6.17: O K edge spectrum for the undoped Bi-2212 cuprate, calculated using the PBE functional. The energy is related to the Fermi energy.

Chapter 7

Conclusions

In this thesis, the electronic structure of Bi(Pb)-2212 of high-T_C cuprates was investigated. Several critical experiments were carried out using XAS and ARPES. In addition, DFT calculations were performed.

Two types of measurements were performed by XAS:

1) The temperature dependence of the hole density was measured, which is a key for addressing the following issues: i) The Gor'kov and Teitel'baum formula could not fit our data of the entire temperature range from 10 K till 300 K. The deviations were solved by adding a new term to the Gor'kov and Teitel'baum formula. ii) The new term could be due to a contribution of magnons in the high-T_c cuprate Bi-2212, what has also been recently confirmed in other high-T_C cuprates as discussed in section 4.3. As discussed in chapter one, many researchers believe that magnetic interactions play a fundamental role in the pairing mechanism of cuprates. Also magnetic interactions may prove to be important in d-wave pairing. iii) The results rule out the two-band model that has been used to explain Hall effect data. iv) The temperature dependence of the hole density and the temperature dependence of R_H strongly challenge the description of cuprates as Fermi liquids or marginal Fermi liquids. v) The CuL_3 and O K absorption edge spectra have also been calculated by DFT using the PBE functional. The PBE functional was

successful in qualitatively producing the CuL_3 and O K absorption spectra of the undoped Bi-2212 cuprate.

2) The polarization dependence of the hole density showed an inhomogeneous hole distribution in the copper oxide plane, and highlighted the role of the other d orbitals (as has also been discussed by Anderson et al. [173]). This idea is also validated by the ARPES data in chapter five and the DFT results in chapter six.

ARPES measurements on the polarization and temperature dependence of the density of states at the M point show that

i) the sharp peak at E_F indicates a temperature dependence on the scale of T^* and not on T_C.

ii) the sharp peak also exhibited a polarization behavior, such that two unexpected observations were found in this work, which can not be understood within the dipole approximation using Fermi's golden rule. The first was the observation of the sharp peak for a polarization geometry normal to the mirror plane what is dipole forbidden for $d_{x^2-y^2}$ derived states. However, the peak can be explained from symmetry considerations by accounting for the other orbitals. The second observation was that the spectra for the 45° and -45° polarization geometries were different.

iii) measurements of the polarization dependence at all four M points of the Brillouin zone revealed a two-by-two similar polarization behavior. This could be due to some directional charge ordering along the 45° to CuO bonds, such as e.g. stripes.

The DFT calculations on the Bi-cuprates produced the following results:

i) Electronic structure calculations based on LDA and GGA predicted metallic properties for the undoped cuprate instead of an AFM ground state.

ii) The Hubbard U parameter was calculated for $CaCuO_2$ and Bi-2212 compounds. The electronic structure of both materials was then calculated

based on the GGA+U method. The AFM ground state was obtained only for $CaCuO_2$, showing the splitting of the upper Hubbard bands and the lower Hubbard bands, as well as the role of the oxygen orbitals in the two compounds. The strong correlations in the CuO_2 plane of Bi-2212 seem to make it impossible to produce the AFM ground state by the LDA/GGA functionals and the GGA+U method.

iii) For YBCO, however, the AFM ground state is confirmed by PBE+U and MBJ+U calculations for the undoprd material.

[1] J. Bardeen, L.N. Cooper and J.R. Schrieffer, Phys. Rev. **106**, 162 (1957); **108**, 1175 (1957)

[2] J. G. Bednorz and K. A. Müller: Z. Phys. B-Condensed Matter, 64 189 (1986)

[3] M. K. Wu, J. R. Ashburn, C. J. Torng, P. H. Hor, R. L. Meng, L. Gao, Z. J. Huang, Y. Q. Wang, and C. W. Chu, Phys. Rev. Lett. **58**, 908 (1987)

[4] P.W. Anderson, Science **235**, 1196 (1987)

[5] G. Chen and W.A. Goddard III, Science **239**, 899 (1988)

[6] S.-C. Zhang, Science **275**, 1089 (1997)

[7] N. Nagaosa, Science **27**5, 1078 (1997)

[8] D.J. Scalapino, Science, **284**, 1282 (1998)

[9] S. V. Borisenko, A. A. Kordyuk, A. N. Yaresko, V. B. Zabolotnyy, D. S. Inosov, R. Schuster, B. Büchner, R. Weber, R. Follath, L. Patthey, and H. Berger, Phys. Rev. Lett. **100**, 196402 (2008)

[10] D. Moncton, J. Axe, and F. DiSalvo, Phys. Rev. B **16**, 801 (1977)

[11] E. Morosan, H. W. Zandbergen, B. S. Dennis, J. W. G. Bos, Y. Onose, T. Klimczuk, A. P. Ramirez, N. P. Ong and R. J. Cava, Nature Physics **2**, 544 (2006)

[12] L. P. Gor'kov and G. B. Teitel'baum, Phys. Rev. B **77**, 180511 (2008) ;
L. P. Gor'kov and G.B. Teitel'baum, Journal of Physics: Conference Series **108**, 012009 (2008)

[13] P. A. Miles, S. J. Kennedy, A. R. Anderson, G. D. Gu, G. J. Russell, and N. Koshizuka, Phys. Rev B **55**, 14632 (1997)

[14] J. M. Tarascon, Y. LePage, P. Barboux, B. G. Bagley, L. H. Greene, W. R. McKinnon, G. W. Hull, M. Giroud, and D. M. Hwang, Phys. Rev. B **37**, 9382 (1988); K. Yvon and M. Francois Z. Phys. B Condensed Matter **76**, 413 (1989)

[15] S. A. Sunshine, T. Siegrist, L. F. Schneemeyer, D. W. Murphy, R. J. Cava, B. Batlogg, R. B. VanDover, R. M. Fleming, S. H. Glarum, S. Nakahara, R. Farrow, J. J. Krajewski, S. M. Zahurak, J. V. Waszczak, J. H. Marshall, P. Marsh, L. W. Rupp, and W. F. Peck, Phys. Rev. B **38**, R893 (1988); J. B. Torrance, Y. Tokura, S.J. LaPlaca, T.C. Huang, R.J. Savoy, A.I. Nazzal, Solid State Com. **66**, 703 (1988)

[16] M. A. Subramanian, C. C. Torardi, J. C. Calabrese, J. Gopalakrishnan, K. J. Morrissey, T. R. Askew, R. B. Flippen, U. Chowdhry, and A. W. Sleight, Science **239**, 1015 (1988)

[17] V. V. Zadorozhnii, O. I. Dubrovskii, E. R. Likhachev, nd S. I. Kurgankii, J. of Stru. Chem., 39, 876 (1998); J.H. Sharp, Br. Ceram. Trans. J. **89**, 1-7 (1990)

[18] R. M. Hazen, C. T. Prewitt, R. J. Angel, N. L. Ross, L. W. Finger, C. G. Hadidiacos, D. R. Veblen, P. J. Heaney, P. H. Hor, R. L. Meng, Y. Y. Sun, Y. Q. Wang, Y. Y. Xue, Z. J. Huang, L. Gao, J. Bechtold, and C. W. Chu, Phys. Rev. Lett. **60**, 1174 (1988)

[19] V. Petricek, Y. Gao, P. Lee, and P. Coppens, Phys. Rev. B **42**, 387 (1990)

[20] A. F. Marshall, B. Oh, S. Spielman, M. Lee, C. B. Eom, R. W. Barton, R. H. Hammond, A. Kapitulnik, M. R. Beasley, and T. H. Geballe, Appl. Phys. Lett. **53**, 426 (1988)

[21] Y. Gao, P. Lee, P. Coppens, M. A. Subramania, and A. W. Sleight, Science **241**, 954 (1988)

[22] Y. Le Page, W. R. McKinnon, J.-M. Tarascon, and P. Barboux, Phys. Rev. B **40**, 6810 (1989)

[23] M. D. Kirk, J. Nogami, A. A. Baski, D. B. Mitzi, A. Kapitulnik, T. H. Geballe, and C. F. Quate, Science **242**, 1673 (1988)

[24] H. W. Zanderbergen, W. A. Groen and F. C. Mullhoff, Physica C **156**, 325 (1988)

[25] P. Goodman, P. Miller, T. J. White, and R. L. Withers, Acta Crystallogr. B **48**, 376 (1992)

[26] H. Zhang and H. Sato, Physica C **214**, 265 (1993)

[27] A. A. Levin, Yu. I. Smolin, and Yu. F. Shepelv, J. Phys. Condens. Matter **6**, 3359 (1994)

[28] M. B. Walker and Q. Wieming, Phys. Rev. B **45**, 8085 (1992)

[29] G. Calestani, C. Rizzoli, M. G. Francesconi, and G. D. Andreetti, Physica C **161**, 598 (1989)

[30] T. J. Lee, C. F. Huang, C. C. Teo, T. S Khor, H. C. Ku, K. W. Yeh, Y. Huang, H. H. Hung, Kiwako Sakabe, and Noriyoshi Sakabe, CHINESE JOURNAL OF PHYSICS **38**, 243 (2000)

[31] T. Yokoya, T. Takahashi, T. Mochiku, and K. Kadowaki, Phys. Rev. B **51**, 3945 (1995)

[32] A. Bansil and M. Lindroos, Phys. Rev. Lett. **83**, 5154 (1999)

[33] S. Legner. Die Fermifläche des Kupratsupraleiters $Bi_2Sr_2CaCu_2O_{8+\delta}$: Ergebnisse der winkelaufgelösten Photoemissionsspektroskopie. Dissertation, IFW Dresden/TU Dresden, 2003.

[34] M. R. Presland, J. L. Tallon, R. G. Buckley, R. S. Liu, and N. E. Flower, Physica C **176**, 95 (1991)

[35] L. Dudy. Nature and organization of the CuO_2-plane as experimentally probed in the prototype high-temperature superconductor Bi2201. PhD thesis, HU Berlin, (2008)

[36] J. Orenstein, A.J. Millis, Science **288**, 468 (2000)

[37] P. W. Anderson, in *The Theory of Superconductivity in the High-T_c Cuprates*, (Princeton Univ. Press, Princeton, New Jersey, 1997), Chap. 3

[38] R. S. Markicwicz, T. Das, A. Bansil, arXiv:1011.2141v1

[39] Ch. Renner, B. Revaz, J-Y. Genoud, K. Kadowaki, and Ø. Fischer Phys. Rev. Lett. **80**, 149 (1998)

[40] B. Wuyts, V. V. Moshchalkov, and Y. Bruynseraede, Phys. Rev. B **53**, 9418 (1996)

[41] T. Tamegai and Y. Iye, Phys. Rev. B **44**, 10167 (1991)

[42] T. Watanabe, T. Fujii, and A. Matsuda, Phys. Rev. Lett. **79**, 2113 (1997)

[43] T. Yoshida, M. Hashimoto, I. M. Vishik, Z.-X. Shen, A. Fujimori, J. Phys. Soc. Jpn. **81**, 011006 (2012)

[44] M. Hashimoto, R.-H. He, I. M. Vishik, F. Schmitt, R. G. Moore, D. H. Lu, Y. Yoshida, H. Eisaki, Z. Hussain, T. P. Devereaux, and Z.-X. Shen, Phys. Rev. B **86**, 094504 (2012)

[45] H. Ding, T. Yokoya, J. C. Campuzano, T. Takahashi, M. Randeria, M. R. Norman, T. Mochiku, K. Kadowaki, and J. Giapintzakis, Nature **382**, 51 (1996)

[46] D. N. Basov, S. I. Woods, A. S. Katz, E. J. Singley, R. C. Dynes, M. Xu, D. G. Hinks, C. C. Homes, and M. Strongin, Science, **283**, 49 (1999)

[47] G.-q. Zheng, W. G. Clark, Y. Kitaoka, K. Asayama, Y. Kodama, P. Kuhns, and W. G. Moulton, Phys. Rev. B **60**, R9947 (1999)

[48] G. V. M. Williams, J. L. Tallon, E. M. Haines, R. Michalak, and R. Dupree, Phys. Rev. Lett. **78**, 721 (1997)

[49] J. W. Loram, K. A. Mirza, J. R. Cooper, and W. Y. Liang, Phys. Rev. Lett. **71**, 1740 (1993)

[50] J. Bobroff, H. Alloul, P. Mendels, V. Viallet, J.-F. Marucco, and D. Colson, Phys. Rev. Lett. **78**, 3757 (1997)

[51] M. R. Norman, H. Ding, M. Randeria, J. C. Campuzano, T. Yokoya, T. Takeuchi, T. Takahashi, T. Mochiku, K. Kadowaki, P. Guptasarma, and D. G. Hinks, Nature **392**, 157 (1998)

[52] H. Ding, M. R. Norman, T. Yokoya, T. Takeuchi, M. Randeria, J. C. Campuzano, T. Takahashi, T. Mochiku, and K. Kadowaki, Phys. Rev. Lett. **78**, 2628 (1997)

[53] C. P. Poole Jr., H. A. Farach, R. J. Creswick, R. Prozorov, Superconductivity, Amsterdam , Elsevier (2007)

[54] V. J. Emery, S.A. Kivelson, O. Zacher, Phys. Rev. B **56**, 6120 (1997)

[55] C. Capan, K. Behnia, J. Hinderer, A. G. M. Jansen, W. Lang, C. Marcenat, C. Marin, and J. Flouquet, Phys. Rev. Lett. **88**, 056601 (2002)

[56] Y. Wang, S. Ono, Y. Onose, G. Gu, Yoichi Ando, Y. Tokura, S. Uchida, and N. P. Ong, Science **299**, 86 (2003)

[57] F. Rullier-Albenque, R. Tourbot, H. Alloul, P. Lejay, D. Colson, and A. Forget, Phys. Rev. Lett. **96**, 067002 (2006)

[58] Y. Wang, L. Li, M. J. Naughton, G. D. Gu, S. Uchida, and N. P. Ong, Phys. Rev. Lett. **95**, 247002 (2005)

[59] S. Chakraborty and P. Philips, Phys. Rev. B **80**, 132505 (2009)

[60] B. Sacépé, C. Chapelier, T. I. Baturina, V. M. Vinokur, M. R. Baklanov, and M. Sanquer, Phys. Rev. Lett. **101**, 157006 (2008)

[61] S. P. Chockalingam, Madhavi Chand, Anand Kamlapure, John Jesudasan, Archana Mishra, Vikram Tripathi, and Pratap Raychaudhuri, Phys. Rev. B **79**, 094509 (2009)

[62] J. Heckel and P. Jugelt, X-ray Spectrometry, **13**, 159 (1984)

[63] L. D. Landau, Sov. Phys. JETP 3, 920 (1957) ; L. D. Landau, Sov. Phys. JETP **5**, 101 (1957) ; L. D. Landau, Sov. Phys. JETP **8**, 70 (1958)

[64] P. W. Anderson, in Strong Correlation and Superconductivity, edited by H. Fukuyama, S. Mackawa, and A. Malozemoff (Springer-Verlag, Berlin, 1989)

[65] J. Hwang, T. Timusk, A.V. Puchkov, N.L. Wang, G.D. Gu, C.C. Homes, J.J. Tu, H. Eisaki, arXiv:cond-mat/0306250v2, (2003)

[66] M. Gurvitch and A.T. Fiory, Phys. Rev. Lett. **59**, 1337 (1987)

[67] Z. Schlesinger, R.T. Collins, F. Holtzberg, C. Feild, S.H. Blanton, U. Welp, G.W. Crabtree, Y. Fang, and J.Z. Liu, Phys. Rev. Lett. **65**, 801 (1990)

[68] A.V. Puchkov, D.N. Basov, and T. Timusk, J. Phys.: Condens. Matter **8**, 10 049 (1996)

[69] A. Damascelli, Z. Hussain, and Z.X. Shen, Rev. Mod. Phys. **75**, 473 (2003)

[70] J. M. Tranquada, B. J. Sternlieb, J. D. Axe, Y. Nakamura, and S. Uchida, Nature **375**, 561 (1995)

[71] A. W. Hunt, P. M. Singer, K. R. Thurber, and T. Imai, Phys. Rev. Lett. **82**, 4300 (1999)

[72] N. Ichikawa, S. Uchida, J. M. Tranquada, T. Niemöller, P. M. Gehring, S.-H. Lee, and J. R. Schneider, cond-mat/9910037 (1999)

[73] T. Noda, H. Eisaki, and S. Uchida, Science **286,** 265 (1999)

[74] H. A. Mook, P. Dai, S. M. Hayden, G. Aeppli, T. G. Perring, and F. Dogan, Nature **395,** 580 (1998); H. A. Mook and F. Dogan, Nature **401,** 145 (1999)

[75] P. Dai, H. A. Mook, and F. Dogan, Phys. Rev. Lett. **80**, 1738 (1998)

[76] M. Akoshima, T. Noji, Y. Ono, and Y. Koike, Phys. Rev. B **57,** 7491 (1998)

[77] Y. Ando, A. N. Lavrov, and K. Segawa, Phys. Rev. Lett. **83,** 2813 (1999)

[78] A. Mourachkine, Supercond. Sci. Technol. **13**, 1378 (2000)

[79] C. M. Varma, P.B. Littlewood, S. Schmitt-Rink, E. Abrahams, A.E. Ruchenstein, Phys. Rev. Lett. **63**, 1996 (1989)

[80] X. T. Wu and R. Ikeda, Phys, Rev. B **83**, 104517 (2011)

[81] N. Plakida, High-Temperature Cuprate Superconductors, Springer-Verlag, Berlin Heidelberg (2010)

[82] P. W. Anderson, arXiv:cond-mat/0201429 (2002)

[83] N. Bulut, Adv. Phys, **51**, 1587 (2002)

[84] G. Kotliar, S.Y. Savrasov, K. Haule, V.S. Oudovenko, O. Parcollet, and C.A. Marianetti, Rev. Mod. Phys, **78**, 865 (2006)

[85] Th. Maier, M. Jarrel, Th. Pruschke, and M.H. Hettler, Rev. Mod. Phys, **77**, 1027 (2005)

[86] N. M. Plakida and V.S.Oudovenko, Condensed Matter Physics, **11**, 495 (2008)

[87] J. Hubbard, Proc. Roy. Soc. A **276**, 238 (1963); J. Gutzwiller, Phys. Rev. Lett. **10**, 59 (1963)

[88] W. Nolting and W. Borgiel, Phys. Rev. **33**, 6962 (1982)

[89] V. I. Anisimov and O. Gunnarsson, Phys. Rev. B **43**, 7570 (1991)

[90] N. F. Mott, Metal-Insulator Transitions, 2nd edn. (Taylor and Francis, London, 1990)

[91] R. S. Markiewicz, Tanmoy Das, and A. Bansil, Phys. Rev. B **82**, 224501 (2010)

[92] V. Emery, Phys. Rev. Lett. **58**, 2794 (1987)

[93] C. M. Varma, S. Schmitt-Rink, E. Abrahams, Solid State Commun. **62**, 681 (1987)

[94] F. C. Zhang and T.M. Rice, Phys. Rev. B **37**, 3759 (1988)

[95] H. Eskes, L.H. Tjeng, G.A. Sawatzky, Phys. Rev. B **41**, 288 (1990)

[96] X. Wang, L.de' Medici, and A. J. Millis, Phys. Rev. B **83**, 094501 (2011)

[97] C. Janowitz, U. Seidel, R. -St. Unger, A. Krapf, R. Manzke, V. Gavrichkov, S. Ovchinnikov, Pis'ma v Zh. Èksper. Teoret. Fiz., **80**:11, 819 (2004)

[98] A. Bianconi, M. De Santis, A.M. Flank, A. Fontaine, P. Lagarde, A. Marcelli, H. Katayama-Yoshida, and A. Kotani**,** Physica C **153-155**, 1760 (1988)

[99] M. Pompa, C. Li, A. Bianconi, A. Congiu Castellano, S. Della Longa, A.M. Flank, P. Lagarde, and D. Udron. Physica C **184**, 51 (1991)

[100] H. Romberg, M. Alexander, N. Nücker, P. Adelmann, and J. Fink, Phys. Rev. B **42**, 8768 (1990)

[101] A. E. Ruckenstein, P. J. Hirschfeld, and J. Appel, Phys. Rev. B **36**, 857 (1987)

[102] F. Marsiglio, A. Ruckenstein, S. Schmitt-Rink, and C. Varma, Phys. Rev. B **43**, 10 882 (1991)

[103] G. Martinez and P. Horsch, Phys. Rev. B **44**, 317 (1991)

[104] Z. Liu and E. Manousakis, Phys. Rev. B **45**, 2425 (1992)

[105] T. Tanamoto, H. Kohno, and H. Fukuyama, J. Phys. Soc. Jpn. **62**, 717 (1993)

[106] H. Kamimura, H. Ushio, S. Matsuno, T. Hamada, Theory of copper oxide, Springer-Verlag Berlin Heidelberg (2005)

[107] F. J. Ohkawa, Phys. Rev. B **42**, 4163 (1990)

[108] A. Macridin, M. Jarrell, Th. Maier,and G. A. Sawatzky, Phys. Rev. B **71**, 134527 (2005)

[109] M. Ogata and H. Fukuyama, Rep. Prog. Phys. **71**, 036501 (2008)

[110] P. W. Anderson, Matt. Res. Bull. **8**, 153 (1973)

[111] B. Edegger, V. N. Muthukumar and C. Gros, Advances in Physics, **56**, 6 927–1033 (2007); G. Baskaran, Z. Zou and P.W. Anderson, Solid State Commun. **63** 973 (1987)

[112] P. W. Anderson, Phys. Rev. Lett. **343**, 953 (1975)

[113] K. D. Tsendin, B. P. Popov, D. V. Denisov, Physica C **415**, 94 (2004); K. D. Tsendin, B. P. Popov, D. V. Denisov, Supercond. Sci. Technol. **19**, 313 (2006); K. D. Tsendin, D. V. Denisov, J. of Optoelectronics and Advanced Materials **5**, 1011 (2003)

[114] I. A. Chernik and S. N. Lykov, Sov. Phys. Solid State **23**, 817 (1981)

[115] V. I. Kaidanov and Yu. I. Ravich, Sov. Phys. Usp. **28**, 31 (1985)

[116] S. A. Nemovn and Yu. I. Ravich, Sov. Phys. Usp. **41**, 735 (1998)

[117] R. A. Klemm, Physica C **341**, 939 (2000); and ref. therein

[118] A. M. Gabovich and A. I. Voitenko, Phys. Rev. B **55**, 1081 (1997)

[119] R. Liu, C. G. Olson, W. C. Tonjes, and R. F. Frindt, Phys. Rev. Lett. **80**, 5762 (1998)

[120] D. S. Marshall, D. S. Dessau, D. M. King, C.-H. Park, A. Y. Matsuura, Z.-X. Shen, W. E. Spicer, J. N. Eckstein, and I. Bozovic , Phys. Rev. B **52**, 12548 (1995)

[121] K. Mitsen, O. Ivanenko, Phys. Usp. **47**, 493 (2004)

[122] J. A. Wilson, J. Phys. Condens. Matter **13**, R945 (2001)

[123] A. S. Moskvin, Phys. Rev. B **84**, 075116 (2011)

[124] J. Zaanen and O. Gunnarson, Phys. Rev. B **40**, 7391 (1989)

[125] H. J. Schulz, Phys. Rev. Lett. **64**, 1445 (1990)

[126] M. Kato and K. Machida, J. Phys. Soc. Jpn. **59**, 1047 (1990)

[127] V. J. Emery, S. A. Kivelson, J. M. Tranquada, cond-mat/9907228 (1999)

[128] G. Siebold, C. Castellani, D. DiCastro, and M. Grilli, Phys.Rev. B **58**, 13506 (1998).

[129] V. J. Emery, S. A. Kivelson, and H.-Q. Lin, Physica B **163**, 306 (1990); Phys. Rev. Lett. **64**, 475 (1990)

[130] U. Löw, V. J. Emery, K. Fabricius, and S. A. Kivelson, Phys. Rev. Lett. **72**, 1918 (1994). For a brief review, see J. Zaanen, J. Phys. Chem. Solids **59**, 1769 (1998)

[131] S. R. White and D. J. Scalapino, Phys. Rev. *B* **61**, 6320 (2000)

[132] T. Suzuki, T. Goto, K. Chiba, T. Shinoda, T. Fukase, H. Kimura, K. Yamada, M. Ohashi, and Y. Yamaguchi, Phys. Rev. B **57**, 3229 (1997)

[133] Ch. Niedermayer, C. Bernhard, T. Blasius, A. Golnik, A. Moodenbaugh, and J. I. Budnick, Phys. Rev. Lett. **80**, 3843 (1998)

[134] M. K. Crawford, R. L. Harlow, E. M. McCarron, W. E. Farneth, J. D. Axe, H. Chou, and Q. Huang, Phys. Rev. B **44**, 7749 (1991)

[135] Y. Ohta, T. Tohyama, and S. Maekawa, Phys. Rev. B **43**, 2968 (1991)

[136] D. C. Peets, D. G. Hawthorn, K. M. Shen, Young-June Kim, D. S. Ellis, H. Zhang, Seiki Komiya, Yoichi Ando, G. A. Sawatzky, Ruixing Liang, D. A. Bonn, and W. N. Hardy, Phys. Rev. Lett. **103**, 087402 (2009)

[137] X. Wang, L. de' Medici, and A. J. Millis, Phys. Rev. B **81**, 094522 (2010)

[138] H. Eskes and G. A. Sawatzky, Phys. Rev. B **44**, 9656 (1991)

[139] H. Kamimura and M. Eto, J. Phys. Soc. Jpn. **59**, 3053 (1990)

[140] R. B. Laughlin, Science **242**, 525 (1988)

[141] Y. Ando, Y. Kurita, S. Komiya, S. Ono, and K. Segawa, Phys. Rev. Lett. **92**, 197001 (2004)

[142] T. R. Chien, Z. Z. Wang, and N. P. Ong, Phys. Rev. Lett. **67**, 2088 (1991)

[143] N. E. Hussey, J. Phys. Condens. Matter **20**, 123201 (2008)

[144] P. W. Anderson, Phys. Rev. Lett. **67**, 2092 (1991)

[145] L. Forro, D. Mandrus, C. Kendziora, L. Mihaly, and R. Reeder, Phys. Rev. B **42** (1990)

[146] Y. Ando, A. N. Lavrov, S. Komiya, K. Segawa, and X. F.Sun, Phys. Rev. Lett. **87**, 017001 (2001)

[147] Y. Yanase and K. Yamada, J Phys. Soc. Jpn. **68**, 548 (1999)

[148] M. S. Laad and S. Blawid, Phys. Rev. B **57**, 11738 (1998)

[149] S. G. Kaplan, S. Wu, H.-T. S. Lihn, H. D. Drew, Q. Li, D. B. Fenner, J. M. Phillips, and S. Y. Hou, Phys. Rev. Lett. **76**, 696 (1996)

[150] D. M. Eagles, Solid State Commun. **69**, 229 (1989)

[151] T. Honma, K. Yamaya, F. Minami, and S. Takekaw, Physica C **176**, 209 (1991)

[152] P. Sanchez and H. Sanchez, Phys. stat. sol. (b) **220**, 531 (2000)

[153] B. S. Shastry, B. I. Shraiman, and R. R. P. Singh, Phys. Rev. Lett. **70**, 2004 (1993)

[154] N. E. Hussey, J. R. Cooper, J. M. Wheatley, I. R. Fisher, A. Carrington, A. P. Mackenzie, C. T. Lin, and O. Milat, Phys. Rev. Lett. **76**, 122 (1996)

[155] J. Stöhr, H.C. Siegmann, Magnetism From Fundamentals to Nanoscale Dynamics, Springer-Verlag Berlin Heidelberg (2006)

[156] David T. Attwood, Soft X-Rays and Extreme Ultraviolet Radiation: Principles and Applications, Cambridge university press (1999)

[157] J. J. Rehr and R. C. Albers, Rev. Mod. Phys. **72**, 621 (2000)

[158] www. Cells.es/Beamlines/CLAESS/commissioning.html

[159] A. Bianconi, C. Li, S. Della Longa, and M. Pompa, Phys. Rev. B **45**, 4989 (1992)

[160] R. D. Cowan, The Theory of Atomic Structure and Spectra, University of California Press, Berkeley (1981)

[161] Y. Ando, Y. Hanaki, S. Ono, T. Murayama, K. Segawa, N. Miyamoto, and Seiki Komiya, Phy. Rev. B **61**, R14956 (2000)

[162] M. Ronay, A. Santoni, A. G. Schrott, L. J. Terminello, S. P. Kowalczyk, and F. J. Himpsel, Solid State Commun. **77**, 699 (1991)

[163] P. Ghigna, G. Spinolo, G. Flor, and N. Morgante, Phys. Rev. B **57**, 13426 (1998)

[164] A. Q. Pham, F. Studer, N. Merrien, A. Maignan, C. Michel, and B. Raveau, Phys. Rev. B **48**, 1249 (1993)

[165] N. Merrien, F. Studer, G. Poullain, C. Michel, A. M. Flank, P. Lagarde, and A. Fontaine, J. Solid State Chem. **105**, 112 (1993)

[166] M. Schneider, R.S. Unger, R. Mitdank, R. Müller, A. Krapf, S. Rogaschewski, H. Dwelk, C. Janowitz, and R. Manzke, Phys. Rev. B **72**, 014504 (2005)

[167] A.K. Ariffin, C. Janowitz, B. Müller, L. Dudy, P. Sippel , R. Mitdank, H. Dwelk, A. Krapf, and R. Manzke, J. Phys.: Conf. Series **150**, 052084 (2009)

[168] N. L. Saini, H. Oyanagi, M. Molle, K.B. Garg, C. Kim, and A. Bianconi, J. Phys. Chem. Solids **65,** 1439 (2004)

[169] N. L. Saini, D.S.L. Law, P.Pudney, K.B. Garg, A.A. Menovsky, and J.J.M. Franse, Phys. Rev. B **52**, 6219 (1995)

[170] C. Aruta, G. Ghiringhelli, C. Dallera, F. Fracassi, P. G. Medaglia, A. Tebano, N. B. Brookes, L. Braicovich, and G. Balestrino, Phys. Rev. B **78**, 205120 (2008)

[171] B. Müller, PhD thesis, Humboldt University of Berlin (2010)

[172] N. L. Saini, A. Lanzara, A. Bianconi, and H. Oyanagi, Phys. Rev. B **58**, 11768 (1998)

[173] O. K. Andersen, A. I. Liechtenstein, O. Jepsen, and F. Paulsen. J. of Phys. and Chem. of Solids, **56**(12) 1573, (1995)

[174] S. D. Conradson, I. D. Raistrick, and A. R. Bishop, Science **248**, 1394 (1990)

[175] S.A. Kivelson and V.J. Emery, in Strongly Correlated Electronic Materials: The Los Alamos Symposium 1993 (eds Bedell, K. S. et al.) 619–656 (Addison-Wesley, Maine, 1994)

[176] V. J. Emery and S. A. Kivelson, Physica C **235–240**, 189 (1994)

[177] C. Weber, K. Haule, and G. Kotliar, Phys. Rev. B **82**, 125107 (2010)

[178] C. Lubritto, K. Rosciszewski, and A. M. Oles, J. Phys. Condens. Matter **8**, 11053 (1996)

[179] C. Di Castro, L. F. Feiner, and M. Grilli, Phys. Rev. Lett. **66**, 3209 (1991)

[180] L. F. Feiner, J. H. Jefferson, and R. Raimondi, Phys. Rev. Lett. **76**, 4939 (1996)

[181] A. Ghafari, C. Janowitz, A.K. Ariffin, H. Dwelk, A. Krapf, and R. Manzke, Inpress Physica C, Physica C **485**, 163 (2013)

[182] T. Nishikawa, J. Takeda, and M. Sato, J. Phys. Soc. Japan **63**, 1441 **(**1994)

[183] R. K. Singhal, N.L. Saini, S. Dalela, B. Sekhar, D.C. Jain, and K.B. Garg, NIM. B. **199**, 280 (2003)

[184] K. B. Garg, S. Dalela, N.L. Saini, R.K. Singhal, D.C. Jain, and C.T. Chen, Physica C **399**, 98 (2003)

[185] A. Bianconi, S. Della Longa, C. Li, M. Pompa, A. Congiu-Castellano, D. Udron, A. M. Flank, and P. Lagarde, Phys. Rev B **44**, 10126 (1991)

[186] C. T. Chen, L.H. Tjeng, J. Kwo, H.L. Kao, P. Rudolf, F. Sette, and R.M. Fleming, Phys. Rev. Lett. **68**, 2543 (1992)

[187] R. P. Sharma, S.B. Ogale, Z.H. Zhang, J.R. Liu, W.K. Chu, B.Veal, A. Paulikas, H. Zheng, and T. Venkatesan, Nature **404**, 736 (2000)

[188] J. M. Tranquada, G. D. Gu, M. Hücker, Q. Jie, H.-J. Kang, R. Klingeler, Q. Li, N. Tristan, J. S. Wen, G. Y. Xu, Z. J. Xu, J. Zhou, and M. v. Zimmermann, Phys. Rev. B **78**, 174529 (2008)

[189] M. C. Sekhar, B. G. Krishna, R. R. Reddy, P.V. Reddy, S.V. Suryanarayana, Supercond. Sci. Technol. **9**, 29 (1996)

[190] R. L. Jacobsen, T.M. Tritt, A.C. Ehrlich, and D.J. Gillespie, Phys. Rev. B **47**, 8312 (1993)

[191] L. P. Gor'kov and G. B. Teitel'baum, Phys. Rev. Lett. **97**, 247003 (2006)

[192] S. Ono, S. Komiya, and Y. Ando, Phys. Rev. B **75**, 024515 (2007)

[193] F. V. Kusmartsev and M. Saarela, J Supercond. Nov. Magn. **22**, 155 (2009)

[194] S. Blundell, Magnetism in Condensed Matter, Oxford University Press Inc., New York (2001)

[195] K. Machida, J. of Low Temp. Phys. **44**, 23 (1981)

[196] F. Keffer, in Encyclopedia of Physics, edited by H. P.J. Wijin (Springer, New York, 1966), Vol. XVIII/2

[197] P. Crespo, J.M. Gonzalez, A. Hernando, and F.J. Yndurain, Phys. Rev. B **69**, 12403 (2004)

[198] H. F. Fong, B. Keimer, D. Reznik, D. L. Milius, and I. A. Aksay, Phys. Rev. B **54**, 6708 (1996)

[199] S. M. Hayden, H. A. Mook, Pengcheng Dai, T. G. Perring, and F. Dogan, Nature **429**, 531 (2004)

[200] V. Hinkov, S. Pailhès, P. Bourges, Y. Sidis, A. Ivanov, A. Kulakov, C. T. Lin, D. P. Chen, C. Bernhard, and B. Keimer, Nature **430**, 650 (2004)

[201] H. He, P. Bourges, Y. Sidis, C. Ulrich, L. P. Regnault, S. Pailhès, N. S. Berzigiarova, N. N. Kolesnikov4, and B. Keimer1, Science **295**, 1045 (2002)

[202] D. Reznik, J.-P. Ismer, I. Eremin, L. Pintschovius, T. Wolf, M. Arai, Y. Endoh, T. Masui, and S. Tajima, Phys. Rev. B **78**, 132503 (2008)

[203] C. T. Chen, F. Sette, Y. Ma, M. S. Hybertsen, E. B. Stechel, W. M. C. Foulkes, M. Schulter, S-W. Cheong, A. S. Cooper, L. W. Rupp, Jr., B. Batlogg, Y. L. Soo, Z. H. Ming, A. Krol, and Y. H. Kao, Phys. Rev. Lett. **66**, 104 (1991)

[204] F. P. Koffyberg and F. A. Benko, J. Appl. Phys. **53**, 1173 (1982)

[205] J. Ghijsen, L. H. Tjeng, J. van Elp, H. Eskes, J. Westerink, G. A. Sawatzky, and M. T. Czyzyk, Phys. Rev. B **38**, 11322 (1988)

[206] G. van der Laan, C. Westra, C. Haas, and G. A. Sawatzky, Phys. Rev. B **23**, 4369 (1981)

[207] J. Zaanen, C. Westra, and G. A. Sawatzky, Phys. Rev. B **33**, 8060 (1986)

[208] G. A. Sawatzky, Stud. Inorg. Chem. **3**, 3 (1983)

[209] M. Faiz, J. Jennings, J. C. Campuzano, E. E. Alp, J. M. Yao, D. K. Saldin, and Jaejun Yu, Phys. Rev. B **50**, 6370 (1994)

[210] H. Hertz, Ann. Phys. **17**, 983 (1887)

[211] A. Einstein, Ann. Physik **31**, 132 (1905)

[212] A. Fujimori, E. Takayama-Muromachi, Y. Uchida, and B. Okai, Phys. Rev. B **35**, 8814 (1987)

[213] T. Takahashi, F. Maeda, H. Arai, H. Katayama-Yoshida, Y. Okabe, T. Suzuki, S. Hosoya, A. Fujimori, T. Shidara, T. Koide, T. Miyahara, M. Onoda, S. Shamoto, and M. Sato, Phys. Rev. B **36**, 5686 (1987)

[214] Z. Shen, J. W. Allen, J. J. Yeh, J.-S. Kang, W. Ellis, W. Spicer, L. Lindau, M. B. Maple, Y. D. Dalichaouch, M. S. Torikachvili, J. Z. Sun, and T. H. Geballe, Phys. Rev. B **36**, 8414 (1987)

[215] T. Takahashi, H. Matsuyama, H. Katayama-Yoshida, Y. Okabe, S. Hosoya, K. Seki, H. Fujimoto, M. Sato, and H. Inokuchi, Phys. Rev. B **39**, 6636 (1989)

[216] A. Kaminski, S. Rosenkranz, H. M. Fretwell, M. R. Norman, M. Randeria, J. C. Campuzano, J-M. Park, Z. Z. Li, and H. Raffy, Phys. Rev. B **73**, 174511 (2006)

[217] H.-B. Yang, J. D. Rameau, Z.-H. Pan, G. D. Gu, P. D. Johnson, H. Claus, D. G. Hinks, and T. E. Kidd, Phys. Rev. Lett. **107**, 047003 (2011)

[218] S. Hüfner, Photoelectron Spectroscopy Principles and Applications, Springer-Verlag Berlin (2003)

[219] A. Damascelli, Physica Scripta. T**109**, 61 (2004)

[220] J. B. Pendry, Surface Science **57**, 679 (1976)

[221] J.F.L. Hopkinson and J.B. Pendry, Computer phys. Comm. **19**, 69 (1980)

[222] C. N. Berglund and W.E. Spicer, Phys. Rev. A **136**, 1030 (1964)

[223] M. P. Seah and W. A. Dench, Surface and Interface Analysis 1, 2 (1979)

[224] J. Hermanson Solid State Comm. **22**, 11 (1977)

[225] M. Lindroos, S. Sahrakorpi, and A. Bansil, Phys. Rev. B **65**, 054514 (2002)

[226] S. Sahrakorpi, M. Lindroos, and A. Bansil, Phys. Rev. B **68**, 054522 (2003)

[227] V. Arpiainen and M. Lindroos, Phys. Rev. Lett. **97**, 037601 (2006)

[228] M. C. Asensio, J. Avila, L. Roca, A. Tejeda, G. D. Gu, M. Lindroos, R. S. Markiewicz, and A. Bansil, Phys. Rev. B **67**, 014519 (2003)

[229] C. Sakai, F. Matsui, N. Takahashi, S. N. Takeda, and H. Daimon, Phyica C **467**, 43 (2007)

[230] J. Mesot, M. Randeria, M. R. Norman, A. Kaminski, H. M. Fretwell, J. C. Campuzano, H. Ding, T. Takeuchi, T. Sato, T. Yokoya, T. Takahashi, I. Chong, T. Terashima, M. Takano, T. Mochiku, and K. Kadowaki, Phys. Rev. B **63**, 224516 (2001)

[231] A. Ghafari, C. Janowitz, P. Hlawenka, R. Weyrich, H. Dwelk, A. Krapf, and R. Manzke, Phys. Rev. Lett., to be submitted

[232] Z.-X. Shen and J.R. Schrieffer, Phys. Rev. Lett. **78**, 1771 (1997)

[233] M. R. Norman and H. Ding, Phys. Rev. B **57**, R11089 (1998)

[234] P. W. Anderson and Y. Ren, High Temperature superconductivity, Addision-Wesley, Redwood City, California (1990)

[235] T. Valla, A. V. Fedorov, P. D. Johnson, Q. Li, G. D. Gu, and N. Koshizuka, Phys. Rev. Lett. **85**, 828 (2000)

[236] R. Hlubina and T. M. Rice, Phys. Rev. B **51**, 9253 (1995)

[237] D. S. Dessau, B. O. Wells, Z.-X. Shen, W. E. Spicer, A. J. Arko, R. S. List, D. B. Mitzi, and A. Kapitulnik, Phys. Rev. Lett. **66**, 2160 (1991)

[238] J. C. Campuzano, H. Ding, M. R. Norman, H. M. Fretwell, M. Randeria, A. Kaminski, J. Mesot, T. Takeuchi, T. Sato, T. Yokoya, T. Takahashi, T. Mochiku, K. Kadowaki, P. Guptasarma, D. G. Hinks, Z. Konstantinovic, Z. Z. Li, and H. Raffy, Phys. Rev. Lett. **83**, 3709 (1999)

[239] X.-G. Wen and P.A. Lee, Phys. Rev. Lett. **76**, 503 (1996)

[240] E. W. Carlson and D. Orgad, S. A. Kivelson, and V. J. Emery, Phys. Rev. B **62**, 3422 (2000)

[241] Z.-X. Shen, P. J. White, D. L. Feng, C. Kim, G. D. Gu, H. Ikeda, R. Yoshizaki, and N. Koshizuka, Science **280**, 259 (1998)

[242] A. G. Loeser, Z.-X. Shen, M. C. Schabel, C. Kim, M. Zhang, and A. Kapitulnik, Phys. Rev. B **56**, 14185 (1997)

[243] A. V. Fedorov, T. Valla, P. D. Johnson, Q. Li, G. D. Gu, and N. Koshizuka, Phys. Rev. Lett. **82**, 2179 (1999)

[244] B. Müller, L. Dudy, C. Janowitz, and R. Manzke, Phys. Rev. Lett. **103**, 109701 (2009)

[245] A. G. Loeser, Z.-X. Shen, M. C. Schabel, C. Kim, M. Zhang, A. Kapitulnik, and P. Fournier, , Phys. Rev. B **56**, 14 185 (1997)

[246] B. Fauque, Y. Sidis, V. Hinkov, S. Pailhes, C. T. Lin, X. Chaud, and P. Bourges, Phys. Rev. Lett. **96**, 197001 (2006)

[247] R. Daou, J. Chang, D. LeBoeuf, O. Cyr-Choinière, F. Laliberté, N. Doiron-Leyraud, B. J. Ramshaw, R. Liang, D. A. Bonn, W. N. Hardy, and L. Taillefer, Nature **463**, 519 (2010)

[248] N. Poccia, G. Campi, M. Fratini, A. Ricci, N. L. Saini, and A. Bianconi, Phys. Rev. B **84**, 100504(R) (2011)

[249] N. L. Saini, J. Avila, M. C. Asensio, S. Tajima, G. D. Gu, N. Koshizuka, A. Lanzara and A. Bianconi , Phys. Rev. B **57**, R11 101 (1998)

[250] N. L. Saini, A. Bianconi, A. Lanzara, J. Avila, M. C. Asensio, S. Tajima, G. D. Gu, and N. Koshizuka, Phys. Rev. Lett. **82**, 2619 (1999)

[251] S. M. Hayden, G. Aeppli, H. A. Mook, T. G. Perring, T. E. Mason, S.-W. Cheong, and Z. Fisk, Phys. Rev. Lett. **76**, 1344 (1996) ; G. Aeppli, T. E. Mason, S. M. Hayden, H. A. Mook, and J. Kulda , Science **278**, 1432 (1997); S. Chakravarty, Science **278**, 1412 (1997)

[252] B. O. Wells, Y. S. Lee, M. A. Kastner, R. J. Christianson, R. J. Birgeneau, K. Yamada, Y. Endoh, and G. Shirane, Science **277**, 1067 (1997); K. Yamada et al., J. Supercond. **10**, 343 (1997)

[253] J. M. Tranquada J. D. Axe, N. Ichikawa, A. R. Moodenbaugh, Y. Nakamura, and S. Uchida, Phys. Rev. Lett. **78**, 338 (1997)

[254] A. Bianconi, N. L. Saini, A. Lanzara, M. Missori, T. Rossetti
H. Oyanagi, H. Yamaguchi, K. Oka, and T. Ito, Phys. Rev. Lett. **76**, 3412 (1996)

[255] N. L. Saini, J. Avila, A. Bianconi, M. C. Asensio, S. Tajima, G. D. Gu, and N. Koshizuka A. Lanzara, Phys. Rev. Lett. **79**, 3467 (1997)

[256] A. Bianconi, M. Lusignoli, N. L. Saini, P. Bordet, A. Kvick, and P. G. Radaelli, Phys. Rev. B **54**, 4310 (1996)

[257] A. Bianconi, N. L. Saini, T. Rossetti, A. Lanzara, A. Perali, and M. Missori, H. Oyanagi, H. Yamaguchi, and Y. Nishihara, and D. H. Ha, Phys. Rev. B **54**, 12018 (1996)

[258] B. O. Wells, Z. -X. Shen, A. Matsuura, D. M. King, M. A. Kastner, M. Greven, and R. J. Birgeneau, Phys.Rev. Lett. **74**, 964 (1995)

[259] F. Ronning, C. Kim, D. L. Feng, D. S. Marshall, A. G. Loeser, L. L. Miller, J. N. Eckstein, I. Bozovic and Z.-X. Shen, Science **282**, 2067 (1998)

[260] A. A. Kordyuk, S. V. Borisenko, T. K. Kim, K. A. Nenkov, M. Knupfer, J. Fink, M. S. Golden, H. Berger, and R. Follath, Phys. Rev. Lett. **89**, 077003 (2002)

[261] A. V. Chubukov and D. K. Morr, Phys. Rev. Lett. **81**, 4716 (1998)

[262] Y.-D. Chuang, A. D. Gromko, D. S. Dessau, Y. Aiura, Y. Yamaguchi, K. Oka, A. J. Arko, J. Joyce, H. Eisaki, S. I. Uchida, K. Nakamura, and Yoichi Ando, Phys. Rev. Lett. **83**, 3717 (1999)

[263] J. M. Wills, M. Alouani, P. Andersson, A. Delin, O. Eriksson, and O. Grechnyev, Full-Potential Electronic Structure Method, Springer-Verlag Berlin Heidelberg (2010)

[264] http://www.wien2k.at/reg_user/textbooks/DFT_and_LAPW-2_cottenier.pdf

[265] E. Engel and R. M. Dreizler, Density Functional Theory, Springer-Verlag Berlin Heidelberg (2011)

[266] P. Hohenberg and W. Kohn, Phys. Rev. B **136**, 864 (1964)

[267] P. Haas, F. Tran, and P. Blaha, K. Schwarz, and R. Laskowski Phys. Rev. B **80**, 195109 (2009)

[268] J. P. Perdew, K. Burke, and M. Ernzerhof, Phys. Rev. Lett. **77**, 3865 (1996)

[269] Z. Wu and R. E. Cohen, Phys. Rev. B **73**, 235116 (2006)

[270] J. P. Perdew, A. Ruzsinszky, G. I. Csonka, O. A. Vydrov, G. E. Scuseria, V. N. Staroverov, and J. Tao Phys. Rev. A **76**, 040501(R) (2007)

[271] A.P. Gaiduk and V. N. Staroverov Phys. Rev. A **83**, 012509 (2011)

[272] G. I. Csonka, J. P. Perdew, A. Ruzsinszky, P. H. T. Philipsen, S. Lebègue, J. Paier, O. A. Vydrov, and J. G. Ángyán Phys. Rev. B **79**, 155107 (2009)

[273] J. P. Perdew, A. Ruzsinszky, G. I. Csonka, O. A. Vydrov, G. E. Scuseria, L. A. Constantin, X. Zhou, and K. Burke, Phys. Rev. Lett. **100**, 136406 (2008); **102**, 039902(E) (2009)

[274] R. Wahl, D. Vogtenhuber, and G. Kresse, Phys. Rev. B **78**, 104116 (2008)

[275] M. Ropo, K. Kokko, and L. Vitos, Phys. Rev. B **77**, 195445 (2008)

[276] A. Dewaele, M. Torrent, P. Loubeyre, and M. Mezouar, Phys. Rev. B **78**, 104102 (2008)

[277] A. Ghafari, A. Boochani, C. Janowitz, and R. Manzke, Phys. Rev. B **84**, 125205 (2011); M. Moustafa, A. Ghafari, A. Paulheim, C. Janowitz, and R. Manzke, Inpress J. of Electron Spectroscopy and Related Phenomena

[278] J. C. Slater, Phys. Rev. **51**, 846 (1937)

[279] T. L. Loucks, Augmented Plane Wave MethodBenjamin, New York (1967)

[280] D. J. Singh, Planewaves, Pseudopotentials and the LAPW MethodKluwer, Dordrecht (1994)

[281] S. Cottenier, Density Functional Theory and the family of (L)APW-methods: a step-by-step in-troduction (Instituut voor Kern- en Stralingsfysica, K.U.Leuven, Belgium), 2002, ISBN 90-807215-1-4 (to be found at http://www.wien2k.at/reg user/textbooks)

[282] E. Sjöstedt, L. Nordstrom, and D. J. Singh, Solid State Commun. **114**, 15 (2000)

[283] O. Entin-Wohlman, A. B. Harris, and Amnon Aharony, Phys. Rev. B **53**, 11661 (1996)

[284] F. Tran and P. Blaha, Phys. Rev. Lett. **102**, 226401 (2009); D. Koller, F. Tran, P. Blaha, Phys. Rev. B **85**, 155109 (2012)

[285] A. D. Becke and M.R. Roussel, Phys. Rev. A **39**, 3761 (1989)

[286] A. D. Becke, J. Chem. Phys. **98**, 5648 (1993)

[287] C. T. Lee, W. T. Yang, and R. G. Parr, Phys. Rev. B, **37**, 785 (1988)

[288] J. A. Wilson, F.J. Di Salvo, and S. Mahajan, Adv. Phys. **24**, 117 (1975)

[289] L. Li , X. S. Fang , T Y. Zhai , M. Y. Liao , U. K. Guatam , X. C. Wu , Y. Koide , Y. Bando, and D. Golberg . Adv. Mater. **22**, 4151 (2010).

[290] P. Blaha, K. Schwarz, G. Madsen, D. Kvaniscka, and J. Luitz, Wien2k, An Augmented Plane Wave Plus Local Orbitals Program for Calculating Crystal Properties (Vienna University of Technology, Vienna, Austria, 2001)

[291] S. G. Patel, S. K. Arora, and M.K. Agarwal, Bull. Mater. Sci. **21**, 297 (1998)

[292] E. Engel, and S. H. Vosko, Phys. Rev. A **47**, 2800 (1993); E. Engel and S. H. Vosko, Phys. Rev. B **47**, 13164 (1993)

[293] L. Lykke, Bo B. Iversen, and G. K. H. Madsen , Phys. Rev. B **73**, 195121 (2006); David J. Singh, Phys. Rev. B **81**, 195217 (2010); Briki, A. Zaoui, F. Boutaiba, and M. Ferhat, Appl. Phys. Lett. **91**, 182105 (2007)

[294] M. Moustafa, PhD thesis, Humboldt University of Berlin (2012)

[295] S. Pittalis, E. Räsänen, and C. R. Proetto, Phys. Rev. B **81**, 115108 (2010)

[296] D. J. Singh, Phys. Rev. B **82**, 205102 (2010)

[297] W. Feng, D. Xiao, Y. Zhang, and Y. Yao, Phys. Rev. B **82**, 235121 (2010)

[298] A. Ghafari, C. Janowitz, and R. Manzke, Cond. Matt. Phys, submitted

[299] J. A. Wilson and A. D. Yoffe, Adv. Phys. **18**, 193 (1969)

[300] R.A. Klemm, Physica C **341**, 839 (2000)

[301] M. Moustafa, T. Zandt, C. Janowitz, and R. Manzke, Phys. Rev. B **80**, 035206 (2009)

[302] A. C. Makrides, K. M. Abraham, G. L. Holleck, T. H. Nguyen, and R. J. Hurd, Proceeding of 34th International Power Sources Symposium (IEEE, Piscataway, NJ, 1990), p. 167

[303] N. Ahmad, P.C. Klipstein, S.D. Obertelli, E.A. Marseglia, and R.H. Friend, J. Phys. C: Solid State Phys. **20**, 4105 (1987)

[304] A. F. Kusmartseva, B. Sipos, H. Berger, L. Forro, and E. Tutis, Phys. Rev. Lett. **103**, 236401 (2009)

[305] D. W. Murphy, F. J. DiSalvo, G. W. Hull, and J. V. Waszczak, Inorg. Chem. **15**, 17 (1976)

[306] Y. Onuki, T. Hirai, K. Shibutani, T. Komatsubara, J. of Inclusion Phenomena **2**, 279 (1984) and references therein

[307] C. Felser, P. Deniard, M. Bäcker, T. Ohm, J. Rouxel, and A. Simon, J. Mater. Chem. **8**, 1295 (1998)

[308] M. M. May, C. Brabetz, C. Janowitz, and R. Manzke, Phys. Rev. Lett. **107**, 176405 (2011)

[309] C. Monney, C. Battaglia, H. Cercellier, P. Aebi, and H. Beck, Phys. Rev. Lett. **106**, 106404 (2011)

[310] J. van Wezel, P. Nahai-Williamson, and S. S. Saxena, Phys. Rev. B **83**, 024502 (2011)

[311] H. Cercellier, C. Monney, F. Clerc, C. Battaglia, L. Despont, M. G. Garnier, H. Beck, P. Aebi, L. Patthey, H. Berger, and L. Forro, Phys. Rev. Lett. **99**, 146403 (2007)

[312] C. Monney, H. Cercellier, F. Clerc, C. Battaglia, E. F. Schwier, C. Didiot, M.G. Garnier, H. Beck, P. Aebi, H. Berger, L. Forró, and L. Patthey, Phys. Rev. B **79**, 045116 (2009)

[313] M. D. Johannes and I. I. Mazin, Phys. Rev. B **77**, 165135 (2008)

[314] O. Degtyareva, M. V. Magnitskaya, J. Kohanoff, G. Profeta, S. Scandolo, M. Hanfland, M. I. McMahon, and E. Gregoryanz, Phys. Rev. Lett. **99**, 155505 (2007)

[315] A. M. Gabovich, A. I. Voitenko, T. Ekino, Mai Suan Li, H. Szymczak, and M. Pękała, Advances in Cond. Matt. Phys. **2010**, 681070 (2010)

[316] K. Rossnagel, J. Phys.: Condens. Matter **23**, 213001 (2011)

[317] M. M. May, C. Janowitz, and R. Manzke, arXiv:1208.4761v1 (2012)

[318] R. Claessen, R. O. Anderson, J. W. Allen, C. G. Olson, C. Janowitz, W. P. Ellis, S. Harm, M. Kalning, R. Manzke, and M. Skibowski, Phys. Rev. Lett. **69**, 808 (1992)

[319] L. Perfetti, C. Rojas, A. Reginelli, L. Gavioli, H. Berger, G. Margaritondo, M. Grioni, R. Gaál, L. Forró, and F. Rullier Albenque, Phys. Rev. B **64**, 115102 (2001)

[320] P. B. Allen and N. Chetty, Phys. Rev. B **50**, 14855 (1994)

[321] D. K. G. de Boer, C. F. van Bruggen, G. W. Bus, R. Coehoorn, C. Haas, G. A. Sawatzky, H. W. Myron, D. Norman, and H. Padmore, Phys. Rev. B **29**, 6797 (1984)

[322] R. Claessen, R. O. Anderson, G.-H. Gweon, J. W. Allen, W. P. Ellis, C. Janowitz, C. G. Olson, Z. X. Shen, V. Eyert, M. Skibowski, K. Friemelt, E. Bucher, and S. Hüfner, Phys. Rev. B **54**, 2453 (1996)

[323] A. Ghafari, C. Janowitz, and R. Manzke, Phys. Rev. B, to be submitted

[324] Massidda, J. Yu, and A.J. Freeman, Physica C **152**, 251 (1988)

[325] H. Krakauer and W.E. Pickett, Phys. Rev. Lett. **60**, 1665 (1988)

[326] M.S. Hybertsen and L.F. Matheiss, Phys. Rev. Lett. **60**, 1661 (1988)

[327] B. Szpunar and V.H. Smith Jr., Phys. Rev. B **45**, 10616 (1992)

[328] V. Bellini, F. Manghi, T. Thonhauser, and C. Ambrosch-Draxl, Phys. Rev. B **69**, 184508 (2004)

[329] Quantum Esperesso packages , http://www.quantum-espresso.org/

[330] F. D. Murnaghan, Proc. Nat. Acad. Sci. **30**, 244 (1944)

[331] V.I. Anisimov, J. Zaanen, and O.K. Andersen, Phys. Rev. B **44**, 943 (1991)

[332] I. Schnell, G. Czycholl, and R. C. Albers, Phys. Rev. B **65**, 075103 (2002)

[333] G. K. H. Madsen and P. Novák, Europhys. Lett. **69** (5), 777 (2005); http://www.wien2k.at/reg_user/textbooks/Constraint_U.pdf

[334] M. T. Czyżyk and G. A. Sawatzky Phys. Rev.B **49**, 14211 (1994)

[335] G. M. Lopez, A. Filippetti, M. Mantega, and V. Fiorentini, Phys. Rev. B **82**, 195122 (2010)

[336] I. P. R. Moreira, P. Rivero, and F. Illas, J. Chem. Phys. **134**, 074709 (2011)

[337] D. Vaknin, E. Caignol, P. K. Davies, J. E. Fischer, D. C. Johnston, and D. P. Goshorn Phys. Rev. B **39**, 9122 (1989)

[338] Y. Tokura, S. Koshihara, T. Arima, H. Ishibashi, T. Ido, and S. Uchida , Phys. Rev. B **41**, 11657 (1990)

[339] M.A. Korotin and V.I. Anisimov, Mater. Lett. **10**, 28 (1990)

[340] A.F. Mattheiss and D.R. Hamann, Phys. Rev. B **40**, 2217 (1989); D. Singh et al. Physica B **163**, 470 (1990)

[341] D.L. Novikov, V.A. Gubanov, A.J. Freeman, Physica C **210**, 301 (1993)

[342] H. Wu, Q. Zheng, X. Gong, and H. Q. Lin, J. Phys.: Condens. Matter **11**, 4637 (1999)

[343] J. D. Jorgensen, M. A. Beno, D. G. Hinks, L. Soderholm, K. J. Volin, R. L. Hitterman, J. D. Grace, Ivan K. Schuller, C. U. Segre, K. Zhang, and M. S. Kleefisch, Phys. Rev. B **36**, 3608 (1987)

[344] J. E. Muller and O. Jepsen, Phys. Rev. Lett. **40**, 720 (1978)

[345] P. J. Durham, J. B. Pendry, and C. H. Hodges, Solid State Commun. **38**, 159 (1981)

[346] G. N. Greaves, P. J. Durham, G. Diakun, and P. Quinn, Nature **294**, 139 (1981)

[347] D. H. Tomboulian, Hanb. Physik **30**, 246 (1957)

[348] L. Smrcka, Czech. J. Phys. B **30**, 1012 (1980)

Publication and Conferences

Papers

- **A. Ghafari**, A. Boochani, C. Janowitz, and R. Manzke, '*Electronic structure of ZrS_xSe_{2-x} by Tran-Blaha modified Becke-Johnson density functional*' , Phys. Rev. B. 84, 125205 (2011)
- **A. Ghafari**, C. Janowitz, A.K. Ariffin, H. Dwelk, A. Krapf, and R. Manzke, '*Temperature dependence of the hole density in high-TC superconductirs $Bi_2Pb_ySr_2CaCu_2O_{8+\delta}$*', Physica C **485**, 163 (2013)
- M. Moustafa, **A. Ghafari**, A. Paulheim, C. Janowitz, and R. Manzke, '*Spin Orbit Splitting in the Valence Bands of ZrS_xSe_{2-x}: Angle Resolved Photoemission and Density Functional Theory*', Inpress J. of Electron Spectroscopy and Related Phenomena
- **A. Ghafari**, C. Janowitz, and R. Manzke, '*The effect of lithium intercalation on the electronic structure of the ternary compound semiconductors $ZrSe_{2-x}S_x$*', Phys. Rev. B, submitted
- **A. Ghafari**, C. Janowitz, and R. Manzke, '*From two copper planes to $Bi_2Sr_2CaCu_2O_8$ by DFT*', Phys. Rev. B, To be submitted
- **Ghafari**, C. Janowitz, P. Hlawenka, R. Weyrich, H. Dwelk, A. Krapf, and R. Manzke, 'Polarization and temperature dependence of ARPES spectra of Bi(Pb)-2212 cuprate', Phys. Rev. Lett., To be submitted

Conferences: Talks and Poster

- **A. Ghafari**, C. Janowitz, A.K. Ariffin, H. Dwelk, A. Krapf, and R. Manzke, '*Inhomogeneity of holes in $(Bi,Pb)_2Sr_2CaCu_2O_{8+\delta}$ single crystals studied by X-ray absorption spectroscopy*', International Conference on Magnetic and Superconducting Materials (MSM11), Malaysia 2011
- C. Janowitz, **A. Ghafari**, P. Hlawenka, R. Weirich, H. Dwelk, A. Krapf, and R. Manzke, '*Systematic ARPES study of the polarization dependence of Bi(Pb)-2212 and (Bi,Pb)-2201 low energy excitations*'

  International conference on superconductivity and magnetism, Istanbul 2012

- M. Orabi Moustafa, **A. Ghafari**, C. Janowitz, and R. Manzke, '*Spin Orbit Splitting in the Valence Bands of* ZrS_xSe_{2-x}*: ARPES and DFT*', 12th International conference on electronic spectroscopy and structure 2012, Saint-Malo, France
- A.K. Ariffin, B. Müller, R. Mitdank. **A. Ghafari**, H. Dwelk, A. Krapf, C. Janowitz, and R. Manzke, '*Temperature dependence of the Hole Density of Underdoped Bi(Pb)-2201 by X-ray Absorption Spectroscopy*', First Joint BER I and BESSY II Users Meeting, 12-13 Nov. 2009, Berlin-Germany
- **A. Ghafari**, A. K. Ariffin, B.Müller, R. Mitdank, H. Dwelk, A. Krapf, C. Janowitz, and R. Manzke, '*Abnormal Temperature Dependence of the Itinerant Hole Density of Bi(Pb)-2201 by X-ray Absorption Spectroscopy*', DPG, Regensburg-Germany, Mar. 2010, http://www.dpg-verhandlungen.de/2010/regensburg/tt9.pdf
- A. Ghafari, A. Boochani, M. Moustafa, C. Janowitz, and R. Manzke, '*Electronic structure of* ZrS_xSe_{2-x} *by density functional theory*', DPG, Dresden-Germany, Mar. 2011)
- **A. Ghafari**, A. K. Ariffin,C. Janowitz, H. Dwelk, R. Mitdank, A. Krapf, and R. Manzke, '*Temperature dependence of itinerant holes of Bi(Pb)-2212 single crystals in the nearly optimally and under-doped regime by XAS*',DPG, Dresden-Germany, Mar. 2011, http://www.dpg-verhandlungen.de/2011/dresden/tt10.pdf
- **A. Ghafari**, A. K. Ariffin, R. Weyrich, C. Janowitz, H. Dwelk, R. Mitdank, A. Krapf, and R. Manzke, '*Fluctuation of the hole density of a slightly under-doped* $(Bi,Pb)_2$ $Sr_2CaCu_2O_{8+\delta}$ *single crystal studied by X-ray absorption spectroscopy*', DPG, Dresden-Germany, Mar. 2011, http://www.dpg-verhandlungen.de/2011/dresden/tt10.pdf
- **A. Ghafari**, A.K. Ariffin, C. Janowitz, H. Dwelk, A. Krapf, and R. Manzke, '*Temperature behavior of the hole density of (Bi,Pb)-2212 single crystals*', DPG, Berlin-Germany, Mar. 2012, http://www.dpg-verhandlungen.de/year/2012/conference/berlin/static/tt27.pdf
- P. Hlawenka, R. Weyrich, **A. Ghafari**, C. Janowitz, H. Dwelk, A. Krapf, and R. Manzke, '*Polarization dependence of low energy excitation of*

(Bi,Pb)-2201 and (Bi,Pb)-2212 using ARPES', DPG, Berlin-Germany, Mar. 2012, http://www.dpg-verhandlungen.de/year/2012/conference/berlin/static/tt33.pdf

- **A. Ghafari**, K. Haghighi mood, C. Janowitz, and R. Manzke, '*Electronic structure of $Bi_2Sr_2CaCu_2O_8$ by DFT and QMC*', DPG, Berlin-Germany, Mar. 2012, http://www.dpg-verhandlungen.de/year/2012/conference/berlin/static/tt27.pdf

Selbständigkeitserklärung

Hiermit versichere ich, die vorliegende Arbeit selbständig und ohne unerlaubte fremde Hilfe angefertigt zu haben. Ich versichere, mich nicht anderweitig um einen Doktorgrad beworben zu haben. Die dem Verfahren zu Grunde liegende Promotionsordnung der Mathematisch-Naturwissenschaftlichen Fakultät I der Humboldt Universität zu Berlin habe ich zur Kenntnis genommen.

Aliakbar Ghafari

Berlin, den 7.2.2013